University of Alberta

Numerical Modeling of the Ocean Circulation in the Canadian Arctic Archipelago

by

Qiang Wang

A thesis submitted to the Faculty of Graduate Studies and Research
in partial fulfillment of the requirements for the degree of

Doctor of Philosophy

Department of Earth and Atmospheric Sciences

Fall 2012
Edmonton, Alberta

Abstract

The Canadian Arctic Archipelago (CAA) is a complex network of straits and basins connecting the Arctic Ocean and the Atlantic Ocean. It is one of the main pathways for freshwater outflow from the Arctic Ocean to the Atlantic Ocean. Circulation and associated variability in the CAA are examined in this thesis using numerical models.

After correcting for shortwave radiation, the CAA model captures much of the observed spatiotemporal structure of the sea ice and ocean circulation in the Canadian Arctic Archipelago, especially, the southward flow in M'Clintock Channel and cyclonic circulation in eastern Lancaster Sound. The momentum balance of ocean currents is studied and we found that the southward flow in M'Clintock Channel is driven by ageostrophic accelerations and is controlled by topography. Vorticity dynamics analysis shows that both stratification and bathymetry have a strong impact on the circulation in eastern Lancaster Sound.

We did some sensitivity experiments to study the impact of the stress on the volume transport through Lancaster Sound and Nares Strait. We found that the ice stress on the ocean in Parry Channel has a strong impact on the seasonal variation of volume transport through Lancaster Sound. The boundary flows also have a strong impact on the volume transport through Lanaster Sound and Nares Striat. The ice stress on the ocean in Parry Channel, stress on the ocean in Nares Strait, stress on the ocean in Baffin Bay all have an impact on the seasonal variation of volume transport through Nares Strait.

Acknowledgements

First and foremost, I owe my deepest gratitude to my supervisor, Prof. Paul G. Myers, for his superb guidance in the development of my research. Without his consistent and illuminating supervision, this thesis could not have reached its present form.

I would like to thank my secondary supervisor, Prof. Andrew B.G. Bush, he gave me many valueable suggestions to help me solve several key problems in my research. I always benefit a lot from conversations with him. I also want to thank Prof. Christian Haas. He provided me with helpful suggestions which greatly improved the thesis and his encouragement inspired me throughout my Phd study.

I would like to thank my labmates: Arjen D. Terwisscha van Scheltinga, Colin Moore, Emily Collier, Ji Lei, Laura Castro, Praveen Kuzhiyil Veluthedathe, Tamara Janes, Veronique Lago and Xianmin Hu for helpming me solve many questions about the models.

Lastly, I want to thank my parents for their love and support.

Table of Contents

1 Introduction **1**

1.1 Sea ice in the CAA and ajacent seas 3

1.2 Ocean Currents in the CAA and ajacent seas 4

1.3 Thesis Outline 9

Bibliography **13**

2 Model description **20**

2.1 Ocean model 20

2.1.1 Primitive Equations 20

2.1.2 Subgrid physics 21

2.1.3 Open boundary conditions 21

2.2 Sea ice model 22

2.2.1 Ice thermodynamics 22

2.2.2 Ice dynamics 24

2.2.3 Continuity equations 26

2.2.4 Ice boundary condition 27

2.3 Ice-ocean coupling 27

Bibliography **29**

3 Model configuration and validation **31**

3.1 Model configuration 31

3.2 Model Evaluation 35
3.2.1 Sea ice 35
3.2.2 Ocean currents 37
3.2.3 Seasonal circulation 38
3.2.4 Temperature and Salinity distribution and mixed layer depth 39
3.3 Sensitivity experiments 40

Bibliography **63**

4 Flow constraints on pathways through the Canadian Arctic Archipelago **69**
4.1 Introduction 69
4.2 Model Configurations 73
4.3 Model Evaluation 78
4.3.1 Sea ice 78
4.3.2 Ocean currents 80
4.4 M'Clintock Channel 82
4.5 Eastern Lancaster Sound 84
4.6 Summary and Discussion 85

Bibliography **99**

5 Seasonal circulation in the CAA **108**
5.1 Introduction 108
5.2 Model configuration 110
5.3 Seasonal pattern in the CAA 111
5.4 Parry Channel 115
5.5 Nares Strait 119
5.6 Conclusions 122

Bibliography **135**

6 Summary **139**

Bibliography **142**

List of Figures

1.1 The name of the island, straits, and locations in the model domain, AG: Amundsen Gulf, B: Bellot Strait, CH: Cardigan Strait and Hell Gate, CP: Cape Parry, D: Dolphin and Union Strait, BM: Byam Martin Channel, BaS: Barrow Strait, FH: Fury and Hecla Strait, FS: Franklin Strait, GA: Prince Gustalf Adolf Sea, GB: Gulf of Boothia, LS: Lancaster Sound, JS: Jones Sound, MaS: Mackenzie Shelf, MC: M'Clintock Channel, MS: McClure Strait, NS: Nares Strait, Pe: Peel Sound, PS: Penny Strait, VMS: Viscount Melville Sound, VS: Victoria Strait, C: Cape Bathurst, CR: Clyde River, De: Devon Island, CI: Cornwallis Island, KW: King William Island, R: Resolute Bay, SH: Sachs Harbour, PP: Prince Patrick Island, PWI: Prince of Wales Island. PRI: Prince Regent Inlet, QEI: Queen Elizabeth Islands, Ro: Roberson Channel, Sm: Smith Sound, SI: Somerset Island, MS, VMS, BaS, and LS constitute Parry Channel. 11

1.2 Mean sea ice concentration in (a) January (b) March (c) May (d) July (e) September (f) November for the period 1988-2004 from SSM/I (Special Sensor Microwave Imager). 12

3.1 The CAA grid. 43

3.2 Bathymetry [m] in CAA control experiment. 44

3.3 The surface air temperature difference [^{0}C] between the IABP/POLES dataset and Large and Yeager (2004) dataset for August. . . . 44
3.4 Downwelling shortwave radiation [W m^{-2}] in July (a) from the Arctic Global Radiation (AGR) dataset, (b) from Large and Yeager (2004) dataset, and (c) the difference between the AGR dataset and Large and Yeager (2004) dataset for June. 45
3.5 (a) Mean sea ice concentration in May for the period 1984-2004 from SSM/I, (b) Simulated mean sea ice concentration in July averaged over years 6-8. 46
3.6 (a) Mean sea ice concentration in September for the period 1984-2004 from SSM/I, (b) Simulated mean sea ice concentration in September averaged over years 6-8. 46
3.7 (a) Mean sea ice concentration in September for the period 1984-2004 from SSM/I, (b) Simulated mean sea ice concentration in September averaged over years 6-8. 47
3.8 Simulated mean sea ice thickness [m] in April averaged over years 6-8. 47
3.9 (a) The mean currents in the CAA averaged over the top 300 m and over years 6-8 in the CAA control experiment, with one fifth of the horizontal grid points shown. The box shows the zoomed region in Figure 3.10. 48
3.10 Zoom of the currents from Figure 3.9. The background field is $\log_{10}(f/h)$. 48
3.11 The mean cross section current speed [cm s^{-1}] in Barrow Strait (section shown in Figure) in April averaged over years 6-8 in the CAA control experiment. 49
3.12 Sea level height [m] averaged over years 6-8 in the CAA in (a) March, (b) September in CAA control experiment. 49

3.13 Sea level height [m] averaged over years 6-8 in the CAA in (a) March, (b) September in CAA control experiment. 50
3.14 Magnitude [cm s^{-1})] of monthly currents over top 50 m (color contoured) averaged over years 6-8 in March (a) and September (b) with velocity vectors superimposed 51
3.15 Magnitude [cm s^{-1})] of monthly currents over top 50 m (color contoured) averaged over years 6-8 in March (a) and September (b) with velocity vectors superimposed 52
3.16 Mean annual cycle of observed volume transport [Sv] from August 1998 to July 2010 (blue line) and modeled volume transport [Sv] from August 1998 to August 2004 (red line) through western Lancaster Sound. 53
3.17 Annual cycle of volume transport [Sv] through Lancaster Sound, M'Clure Strait, Byam Martin Channel, Penny Strait, M'Clintock Channel, Peel Sound in CAA control experiment averaged over years 6-8. 53
3.18 Climatology sea surface temperature [^{0}C] from PHC dataset in the CAA (a) March, (b) September. 54
3.19 Sea surface temperature averaged [^{0}C] over years 6-8 in the CAA in (a) March, (b) September in CAA control experiment. . . . 55
3.20 Temperature [^{0}C] at 100 m in the CAA averaged over years 6-8 in (a) March, (b) September in CAA control experiment. . . . 56
3.21 Sea surface salinity in the CAA averaged over years 6-8 in (a) March and (b) September in CAA control experiment. 57
3.22 Salinity at 100 m in the CAA averaged averaged over years 6-8 (a) March, (b) September in CAA control experiment. 58
3.23 Mixed layer depth [m] in the CAA averaged over years 6-8 in April in CAA control experiment. 58

3.24 The position of ice bridge in Nares Strait (Small blue box). The large blue box shows the model domain. 59
3.25 Modeled sea ice concentration in July 2000 when there is no sea ice bridge in Nares Strait in CAA interannual experiment. . . 59
3.26 Modeled sea ice concentration in July 2000 when the sea ice bridge in Nares Strait is parameterized in CAA interannual experiment. 60
3.27 Modeled sea ice concentration in July 1998 when downwelling shortwave radiation from the CORE data is used and there is no ice bridge in Nares Strait in CAA interannual experiment. . 61
3.28 Modeled sea ice concentration in July 1998 when downwelling shortwave radiation from AGR data is used and the sea ice bridge in Nares Strait is parameterized in CAA interannual experiment. 61
3.29 Observed sea ice concentration from SSM/I in July 1998. . . . 62

4.1 The name of the island, straits, and locations in the model domain, AG: Amundsen Gulf, B: Bellot Strait, D: Dolphin and Union Strait, BM: Byam Martin Channel, BaS: Barrow Strait, FH: Fury and Hecla Strait, FS: Franklin Strait, GB: Gulf of Boothia, LS: Lancaster Sound, JS: Jones Sound, MaS: Mackenzie Shelf, MC: M'Clintock Channel, MS: McClure Strait, NS: Nares Strait, Pe: Peel Sound, PS: Penny Strait, VMS: Viscount Melville Sound, VS: Victoria Strait, C: Cape Bathurst, CR: Clyde River, De: Devon Island, CI: Cornwallis Island, KW: King William Island, R: Resolute Bay, PP: Prince Patrick Island, PWI: Prince of Wales Island. PRI: Prince Regent Inlet, QEI: Queen Elizabeth Islands, SI: Somerset Island, The thick red bold line shows the location of a section in Figure 4.8. MS, VMS, BaS, and LS constitute Parry Channel. 90

4.2 (a) The CAA configuration, (b) The Pan-Arctic configuration with the background bathymetry [m]. 91

4.3 Bathymetry [m] in a) CAA control experiment (upper left), (b) experiment CAA-MC (upper right), (c) experiment CAA-FB (lower left), and (d) experiment CAA-BS (lower right). 91

4.4 Downwelling shortwave radiation [W m^{-2}] in June (a) from the Arctic Global Radiation dataset, (b) from Large and Yeager (2004) dataset, and (c) the difference between the AGR dataset and Large and Yeager (2004) dataset for June. 92

4.5 (a) Mean sea ice concentration in July for the period 1984-2004 from SSM/I. Simulated (b) mean sea ice concentration in July and (c) mean sea ice thickness [m] in April averaged over years 6-8 in the CAA control experiment. 93

4.6 (a) The mean currents in the CAA averaged over the top 300 m and over years 6-8 in the CAA control experiment, with one fifth of the horizontal grid points shown. The box shows the zoomed region in Figure 5, (b) as in (a), but for the Pan-Arctic experiment averaged over years 16-18, with one third of the horizontal grid points shown. 94

4.7 Zoom of the currents from Figure 4.6a. The background field is $\log_{10}(f/h)$. The red line shows the position of line A, where momentum balance is shown in Figure 4.10. 95

4.8 The mean cross section current speed [cm s^{-1}] in Barrow Strait (section shown in Figure 4.1) in April averaged over years 6-8 in the CAA control experiment. 95

4.9 (a) The mean Ertel's potential vorticity and currents averaged over the top 300 m in eastern Lancaster Sound. (b) The cross section current speed [cm s^{-1}] at 81.4°W with the location of the section shown by the thick bold line in subfigure c. (c) Surface salinity in eastern Lancaster Sound. (d) The vertical velocity [10^{-5} m s^{-1}] (contours) over the top 140 m overlaying Ertel's potential vorticity at 81.4°W. Downward velocity is negative. The units for the Ertel's potential vorticity are 10^{-10} m^{-1} s^{-1}. All values are averaged over years 16-18 in the Pan-Arctic experiment. 96

4.10 Meridional momentum balance averaged over top 50 m along line A, which is shown in Figure 4.7. Ageo represents ageostrophic acceleration. The values have been multiplied by 10^7. 97

4.11 (a) the CAA control experiment ice concentration (color contours) and ice motion vectors (black arrows) and wind vectors (magenta arrows) in August and (b) in September. 98

5.1 Magnitude (cm s^{-1}) of monthly sea ice motion (color contoured) in March (a) and September (b) with velocity vectors superimposed in Parry Channel in the fifth year of model run under normal year forcing, with one third of the horizontal grid points shown. 124

5.2 Magnitude (cm s^{-1}) of monthly currents over top 50 m (color contoured) in (a) March (b) and September with velocity vectors superimposed in Parry Channel in the fifth year of the model run under normal year forcing, with one third of the horizontal grid points shown. 125

5.3 The zonal stress [Pa] on the ocean in Parry Channel in (a) March, and (b) June, (c) July, (d) August, (e) September, (f) October, (g) November, (h) December in the fifth year of the model run under normal year forcing. Eastward is positive. . . 126

5.4 Magnitude (cm s^{-1}) of monthly sea ice motion (color contoured) in March (a) and September (b) with velocity vectors superimposed in Nares Strait in the fifth year of the model run under normal year forcing, with one third of the horizontal grid points shown. 127

5.5 Magnitude (cm s^{-1}) of monthly currents over top 50 m (color contoured) in March (a) and September (b) with velocity vectors superimposed in Nares Strait in the fifth year of model run under normal year forcing, with one third of the horizontal grid points shown. 128

5.6 The meridional stress on the ocean in Nares Strait in (a) March, (b) May, (c) July, (d) September, (e) November, (f) January in the fifth year of model run under normal year forcing. Northward is positive. 129

5.7 Magnitude (cm s^{-1}) of monthly sea ice motion (color contoured) in March (a) and September (b) with velocity vectors superimposed in the fifth of model year run under normal year forcing, with one fifth of the horizontal grid points shown. 130
5.8 Magnitude (cm s^{-1}) of monthly currents over top 50 m (color contoured) in March (a) and September (b) with velocity vectors superimposed in the fifth year of model run under normal year forcing, with one fifth of the horizontal grid points shown. 131
5.9 Model results of monthly mean zonal stress [Pa] (a) and meridional stress (b) in March, zonal stress (c) and meridional stress (d) in September in the fifth year of model run under normal year forcing. 132
5.10 Time series of monthly observed (red line) and modeled (blue line) volume transport [Sv] through Lancaster Sound from January 1998 to November 2004. 132
5.11 Mean annual cycle of observed volume transport [Sv] from August 1998 to July 2010 (blue line) and modeled volume transport from August 1998 to August 2004 (red line) through western Lancaster Sound. 133
5.12 Position of areas 1, 2, and 3. 133
5.13 Time series of volume transport [Sv] through western Lancaster Sound in different sensitivity experiments. 134
5.14 Time series of volume transport [Sv] through Nares Strait in different sensitivity experiments. 134

List of Symbols and Abbreviations

AGR	Arctic Global Radiation
CAA	Canadian Arctic Archipelago
$CORE$	Coordinated Ocean Reference Experiments
DSR	Downwelling shortwave radiation
EVP	elastic-viscous-plastic
GCM	General Circulation Model
$IABP$	International Arctic Buoy Program
$IBCAO$	International Bathymetric Chart of the Arctic Ocean
$ISCCP$	International Satellite Cloud Climatology Project
$LY04$	Large and Yeager (2004)
MYI	multiyear ice
$NCEP$	National Centers for Environmental Prediction
$NCAR$	National Center for Atmospheric Research
$NEMO$	Nucleus for European Modeling of the Ocean
$PIOMAS$	Pan-Arctic Ice-Ocean Modeling and Assimilation System
$POLES$	Polar exchange at the Sea Surface
SST	Sea Surface Temperature
SSS	Sea Surface Salinity

VT	Volume transport

List of Tables

3.1 Observed ice thickness and modeled ice thickness (m). 43

4.1 Details on the model configurations and experiments used in the paper. 89

4.2 List of six numerical experiments. 89

4.3 Observed ice thickness and modeled ice thickness (m). 89

5.1 List of sensitivity experiments. 124

Chapter 1

Introduction

Over the modern satellite era, which began in late 1978, Arctic ice extent has shown a downward trend in all months, most rapidly for September (e.g. Serreze et al. (2007); Shimada et al. (2006)). As the summer sea ice cover disappears, the Arctic will become more easily accessible. In September 2007 and 2008, the Arctic sea ice receded so much that the Northwest Passage through the straits of the Canadian Arctic Archipelago (hereinafter, CAA) was navigable (Serreze and Stroeve, 2008). Many scientists think that it is possible that large parts of the Arctic Ocean will be ice free in summer within 100 years because of global warming (Stroeve et al., 2007), some scientists even think that Arctic's summer sea ice will fully melt around 2030 (Stroeve et al., 2008). A reduction of sea ice area could increase biological productivity in the sea ice-upper ocean system (Arrigo et al., 2008) and improve shipping opportunities by opening the Northwest Passage. The fresh water which flows from the Arctic Ocean to the North Atlantic Ocean can have a major effect on deep convection, the Atlantic meridional overturning circulation, and high latitude nutrients and productivity (Aagaard and Carmack, 1989, 1994; Carmack, 2000; Curry and Mauritzen, 2005; Carmack, 2007).

The CAA occupies 2.5×10^6 km^2 of continental shelf that comprise 20% of the Arctic Ocean (Melling, 2000) (Figure 1.1). Many channels in the CAA

have been deepened by glacial action to form a network of basins as deep as 600 m, separated by sills. Deep (365-440 m) sills at the western margin of the continental shelf are the first impediment to inflow from the Canada Basin, but the shallowest sills are in the central and southern parts (Melling, 2000).

The CAA is one of the significant pathways for surface outflow of the Arctic Ocean to the Atlantic. Serreze et al. (2006) estimated that 35% of the total liquid freshwater export from the Arctic passes through the CAA. The transfer of water from the Pacific to the Atlantic has been attributed to the higher sea level of the Pacific (Stigerbrandt, 1984). Steele and Ermold (2007) suggest that the flow through the CAA increased from 1970 to 1990. It is likely that the route and size of freshwater flux from the Arctic to North Atlantic Ocean through the CAA will change in the future (Dickson et al., 2007). Model results show that the freshwater outflow through the CAA is expected to increase by 50% by 2100 (Dickson et al., 2007). In order to understand the impact of the flow change in the CAA, it is important to understand the current/past variations in water properties and circulation in the CAA.

Baffin Bay is the immediate recipient of freshwater passing through the Archipelago. It is a deep (2400 m) basin bounded by banks and a 675 m sill in Davis Strait that restricts exchange with the Labrador Sea.

Scarcity of continuous oceanographic observations in the CAA makes it difficult for a detailed study. Melling et al. (2008) pointed out that some technological challenges remain. For example, instruments that might be deployed near the surface to measure current and salinity are vulnerable to destruction by drifting ice and icebergs. Numerical models are thus an efficient alternative tool to study the circulation in the CAA and freshwater flux through the main straits of the CAA.

My research focus on using a new state-of-the-art coupled ocean/sea-ice general circulation model, NEMO (Nucleus for European Modelling of the

ocean), to develop a tool capable of detailed studies of seasonal and climate variability in the Canadian Arctic, including Baffin Bay and use it to address questions on flow dynamics.

1.1 Sea ice in the CAA and ajacent seas

The minimum sea ice cover in the CAA occurs in early September (Canadian Ice Service, 2007). The western regions of the CAA (i.e., Queen Elizabeth Islands, western Parry Channel, and M'Clintock Channel) contained high concentrations for the entire season from 1988 to 2004 (Figure 1.2). In September, the Prince Gustalf Adolf Sea shows a small net monthly sea ice motion into the CAA and the sea ice moves eastward in Parry Channel (Agnew et al., 2008). Howell et al. (2008) suggests that M'Clintock Channel continuously operates as a drain-trap mechanism for old sea ice and the net sea ice motion into M'Clintock Channel in September and Octocber supports this (Agnew et al., 2008). In September, Lancaster Sound and southern Beaufort Sea is usually ice-free (Figure 1.2).

In winter, the CAA is covered by sea ice (Figure 1.2) and there is little net ice motion in the CAA except for Barrow Strait and Lancaster Sound which have mean eastward ice motion ranging from 4 km/d in January (Agnew et al., 2008). The wind driven ice movement in the CAA is hindered because of numerous shallow and narrow water channels; the internal ice pressure caused by horizontal constrictions usually stops ice drift (Melling, 2002).

Nares Strait is the channel that separates Greenland from Canada between 78°N and 82°N. It borders the Canadian Archipelago and is more than 500 km long. The area is generally ice covered with rapidly drifting multi-year ice floes in summer and with stable land-fast ice (fast-ice) in winter. Ice arches along the strait usually form some time between December and March at the entrance to Robeson Channel and southern Kane Basin (Kwok, 2005; Kwok

et al., 2010). The two ice arches break up in summer (July and August). The ice flux through Nares Strait has been estimated at 4 mSv (Kwok, 2005).

In general, Baffin Bay is ice free in September (Figure 1.2). Ice starts to form in the open water in September and the ice cover increases steadily from north to south reaching a maximum in March when almost all Baffin Bay is covered by sea ice. Throughout the winter, there is generally more sea ice cover in the western than in the eastern half of Baffin Bay due to the inflow of the warm West Greenland Current. The air temperature gradient seems play more important than the water temperature (Barber et al., 2001) to keep the ice thinner on the eastern side. From May to August, the ice area decreases, initially along the Greenland coast and in the North Water. The ice bridge in the southern Kane Basin stops the inflow of ice from the north, with the continued wind-driven southward sea ice motion below the ice being sufficient to create a large polynya in North Water (Melling, 2000). The sea ice concentration is low along the Greenland coast because of the warm West Greenland Current. In July, a large area in the northwest, stretching from Smith Sound to Lancaster Sound, becomes ice-free. In winter, the sea ice motion is southeastward in western Baffin Bay (Agnew et al., 2008). Along the coast of Baffin Island, the mean ice thickness is 1.25-1.5 m in winter (Tang et al., 2004).

1.2 Ocean Currents in the CAA and ajacent seas

Flow through the central archipelago is directed from the Beaufort Sea to Baffin Bay. The zeroth order driving mechanism is the sea level difference (Stigerbrandt, 1984) with temporal anomalies strongly correlated with the wind stress over the Beaufort Sea (Prinsenberg et al., 2009). Extended current meter measurements have been made in Barrow Strait (Figure 1.1) over the

past decade (Prinsenberg and Hamilton, 2005) and provide the single long term record of currents and transports in the region (Melling et al., 2008). Otherwise, only limited short term current records exist (Melling et al., 1984).

The surface layer (above 200m) in the Beaufort Sea is fresher and lighter than that in Baffin Bay (Rudels, 1986) and the difference in steric height from the Beaufort Sea to Baffin Bay, with respect to the 250 decibar level, was calculated by Muench (1971) to be 0.3 m. This difference creates pressure gradients and drives the flow through the CAA (Rudels, 1986).

In McClure Strait, the flow is southeastward (Melling et al., 1984). There is southward flow towards Parry Channel via Byam Martin Channel and Penny Strait, with speeds of 5 to 13 cm s^{-1} based on current meter measurement (Fissel et al., 1988). In M'Clintock Channel, available current meter measurements shows the current is southward (Barry, 1993).

Based on hydrographic data and month-long sets of current meter data, part of the eastward transport through Barrow Strait flows southward into northern Peel Sound before continuing eastward through Barrow Strait at the north entrance of Peel Sound (Prinsenberg and Bennett, 1989). In April 1981, the northward transport (0.17 Sv) in eastern Peel Sound is higher than the southward transport (0.02 Sv) in western Peel Sound and is a significant contributor to Barrow Strait transport (Prinsenberg and Bennett, 1989).

There is a strong eastward current (10-20 cm s^{-1}) on the south side of western Lancaster Sound and the flow is similar at all depths and thus barotropic in nature while the current is weak on the north side of the sound and the flow is variable with depth and baroclinic in nature (Prinsenberg and Hamilton, 2005). Based on a section through western Lancaster Sound coincident with the moorings of Prinsenberg and Hamilton (2005), the yearly mean volume transport at the section, over 1998 to 2006, based on mooring data, is 0.7 $\pm$ 0.3 Sv (Prinsenberg et al., 2009). There is a strong annual cycle of volume

transport through western Lancaster Sound, ranging between weak transport in December (0.2 Sv) and strong transport in summer (1.1 Sv) (Melling et al., 2008). The 6-year mean freshwater flux through western Lancaster Sound is 48 mSv (Melling et al., 2008). McClure Strait/Viscount Melville Sound, Byam Martin Channel, Penny Strait, and Peel Sound are all sources of the transport through western Lancaster Sound.

In the eastern Lancaster Sound, the Baffin Current penetrates westward along the north side of eastern Lancaster Sound, crosses to the south side and flows out to the east based on satellite-tracked drifter measurements, hydrographic data, and current meter data from the summer of 1978 and 1979 (Fissel et al., 1982). In the core of the intrusive current at the north side of eastern Lancaster Sound, the near-surface speed was 75 cm s^{-1}, decreasing to 50 cm s^{-1} at 40 m depth and 25 cm s^{-1} at 250m depth (Fissel et al., 1982). Since the flow is eastward throughout Barrow Strait between Cornwallis Island and Somerset Island (Prinsenberg and Bennett, 1987), the Baffin Current does not extend as far as Resolute Bay, which is located to the south of Cornwallis Island. Jones and Coote (1980) analyzed water masses and nutrient distribution in Parry Channel and Baffin Bay and also suggested that the Baffin Water could not intrude into the region near Resolute Bay.

Inferred from CTD data, there is westward flow on the north side of Viscount Melville Sound, Barrow Strait, and Lancaster Sound (de Lange Boom et al., 1987). However, as far as we know, there is no data from direct current meters moored the north side of Viscount Melville Sound. Holloway and Wang (2009) successfully simulated in a global ice-ocean coupled model a westward current on the north side of Parry Channel. They explained this by the Neptune effect, which is a forcing of mean flows by eddy-topography interaction.

Münchow et al. (2006) estimated that the volume and freshwater fluxes from the Arctic Ocean to Baffin Bay through Nares Strait during their sur-

vey over a short period in August 2003 as 0.8 ± 0.3 Sv and 25 ± 12 mSv, respectively. Münchow and Melling (2008) and Rabe et al. (2010) showed results from instruments measuring ocean currents between 30 m and 300 m depth and temperature, conductivity, and pressure between 30 m depth and a few meters above the seabed for the 2003-2006 period. Based on three-year observations, Münchow and Melling (2008) estimated that the mean volume flux below 30m depth from the Arctic Ocean into Baffin Bay is 0.57 ± 0.09 Sv. The 3-year mean geostrophic velocity has a surface-intensified southward flow of 0.20 m s^{-1} against the western side of the strait and a secondary core flowing southward at 0.14 m s^{-1} in the middle of the strait (Rabe et al., 2010). When the sea ice was drifting in late summer, fall, and early winter, there is a strong surface intensified geostrophic flow in the middle of the strait (Rabe et al., 2010). When the sea ice was immobile in late winter, spring, and early summer, there was a subsurface core of strong geostrophic flow adjacent to the western side of the strait (Rabe et al., 2010). Rabe et al. (2012) found that geostrophic volume flux through the Nares Strait was less strongly influenced by the state of the ice. The 3-year mean geostrophic volume transport through Nares Strait under mobile ice and under fast ice was 0.47 ± 0.12 Sv, and 0.47 ± 0.09 Sv, respectively (Rabe et al., 2012).

The water which flows from the Arctic and then enters into Baffin Bay through Jones Sound needs to pass Cardigan Strait or Hell Gate first. The flow through Cardigan Strait was strong from January to September in 2003 and 2004, with the average flow weaker during the autumn and early winter (Melling et al., 2008). The mean volume fluxes through Cardigan Strait and Hell Gate from 1998 to 2002 are 0.2 Sv and 0.1 Sv, respectively (Melling et al., 2008).

All water which flows out of the CAA enters into Baffin Bay, with the exception of about 0.1 Sv that is diverted along the western side of Baffin

Island through Fury and Hecla Strait (Melling et al., 2008). Tang et al. (2004) reviewed the mean circulation and water properties in Baffin Bay. The West Greenland Current enters Baffin Bay on the very eastern slope of Davis Strait and then flows cyclonically. The current is augmented by outflows from Smith, Jones and Lancaster Sounds to become the Baffin Current. The Baffin Current flows along the western side of Baffin Bay and then the water flows out of Baffin Bay and enters the Labrador Sea.

There is a strong seasonal cycle of volume transport through Barrow Strait (Prinsenberg and Bennett, 1987) and western Lancaster Sound (Melling et al., 2008). The volume transport through west Lancaster Sound is highest in August and lowest in winter (Melling et al., 2008). Prinsenberg and Bennett (1987) found that the monthly sea level difference between Cape Parry/Sachs Harbour and Resolute is also highest in August and lowest in winter. They pointed out that there is a strong relation between the sea level difference along the Northwest Passage and volume transport through Barrow Strait. McLaughlin et al. (2004) pointed out that if the water flow through Barrow Strait is hydraulically controlled, the volume transport through Barrow Strait should increase during summer when the water becomes fresher, and decrease during winter when the water becomes more saline. The ice stress on the ocean is also likely to play an important role in controlling the flow through the CAA, especially in winter when the sea ice forms a static canopy over the channel (Melling, 2000; McLaughlin et al., 2004). It is still unclear what reason is the major cause for the seasonal variation of volume transport through western Lancaster Sound.

Numerical modeling of the CAA in the past has been very limited and the flow dynamics within the CAA are poorly understood. Kliem and Greenberg (2003) used a diagnostic model to study summer mean circulation in the CAA. Their model results reveal that the currents in the CAA depend on the eleva-

tion difference between the Arctic Ocean and Baffin Bay and on the baroclinic pressure gradients. Sou and Flato (2009) used an ice-ocean regional model to examine how sea ice conditions in the archipelago region respond to climate change projections. Aksenov et al. (2010) studied the sources of freshwater in the CAA and the routes of different water masses and their transport passing through the CAA. Terwisscha van Scheltinga et al. (2010) studied the ice flux through the CAA using a high resolution sea ice model. Using a high resolution pan-Arctic model, McGeehan and Maslowski (2012) have pointed out that the reduced northward flow of the West Greenland Current in winter can increase the volume transport through Lancaster Sound in winter compared to that in fall since reduced northward flow of the West Greenland Current can reduce the sea level in Baffin Bay.

1.3 Thesis Outline

The main objective of my thesis research is to use a regional numerical model to investigate the main physical processes responsible for flow pathways and transport variability in the CAA. My thesis research comprises (1) use a three-dimensional ocean circulation model to simulate circulation, sea ice, and associated variability in the CAA, (2) analysis of the model results and for sensitivity analysis to study the flow dynamics within the CAA.

My thesis includes the answers to the following questions:

1. What are the flow pathways through the CAA?

2. What is the flow dynamics that control the flow pathways through the CAA?

3. What are the reasons for the seasonal variability of volume transport through western Lancaster Sound and Nares Strait?

The thesis is laid out as follows: Chapter 2 presents the details of the model equations. Chapter 3 presents the details of the model configuration

and model validation. The model is validated using both sea ice data and ocean data.

Chapter 4 examines flow pathways through the CAA and flow dynamics in the CAA. The classic view is that the water flows from Beaufort Sea to Baffin Bay through Parry Channel. However, my model results show that the flow pathways are more complex than previously thought. More than half of the water which flows through Vicsount Melville Sound loops around Prince of Wales Island. It will be shown that the southward flow in M'Clintock Channel is driven by ageostrophic accelerations and is controlled by topography. Vorticity dynamics have been studied in eastern Lancaster Sound and the results show that both stratification and bathymetry have a strong impact on the circulation in eastern Lancaster Sound.

Chapter 5 presents the seasonal variability of the volume transport through western Lancaster Sound. Model sensitivity experiments are used to demonstrate that from January to May the ice stress on the ocean reduces the volume transport through Parry Channel. The factors that influence the seasonal variability of volume transport through Nares Strait will also be shown. An overall summary is given in Chapter 6.

Chapters 4 to 5 are based on two independent manuscripts, from which some figures and material are also reproduced in the introduction and model chapters. Chapter 4 is the paper entitled: "Flow constrains on pathways through the Canadian Arctic Archipelago" by Wang, Myers, Hu and Bush (Atmosphere-Ocean, in press). Chapter 5 is the paper entitled: "Seasonal circulation in the Canadian Arctic Archipelago" by Wang, Myers and Bush (to be submitted shortly to Geophysical Research Letters).

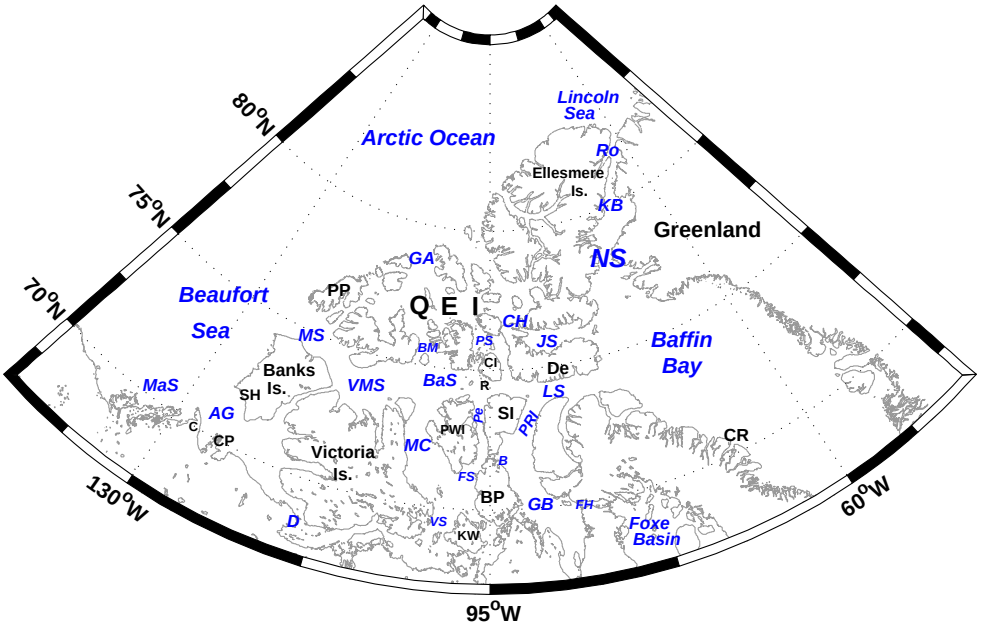

Figure 1.1: The name of the island, straits, and locations in the model domain, AG: Amundsen Gulf, B: Bellot Strait, CH: Cardigan Strait and Hell Gate, CP: Cape Parry, D: Dolphin and Union Strait, BM: Byam Martin Channel, BaS: Barrow Strait, FH: Fury and Hecla Strait, FS: Franklin Strait, GA: Prince Gustalf Adolf Sea, GB: Gulf of Boothia, LS: Lancaster Sound, JS: Jones Sound, MaS: Mackenzie Shelf, MC: M'Clintock Channel, MS: McClure Strait, NS: Nares Strait, Pe: Peel Sound, PS: Penny Strait, VMS: Viscount Melville Sound, VS: Victoria Strait, C: Cape Bathurst, CR: Clyde River, De: Devon Island, CI: Cornwallis Island, KW: King William Island, R: Resolute Bay, SH: Sachs Harbour, PP: Prince Patrick Island, PWI: Prince of Wales Island. PRI: Prince Regent Inlet, QEI: Queen Elizabeth Islands, Ro: Roberson Channel, Sm: Smith Sound, SI: Somerset Island, MS, VMS, BaS, and LS constitute Parry Channel.

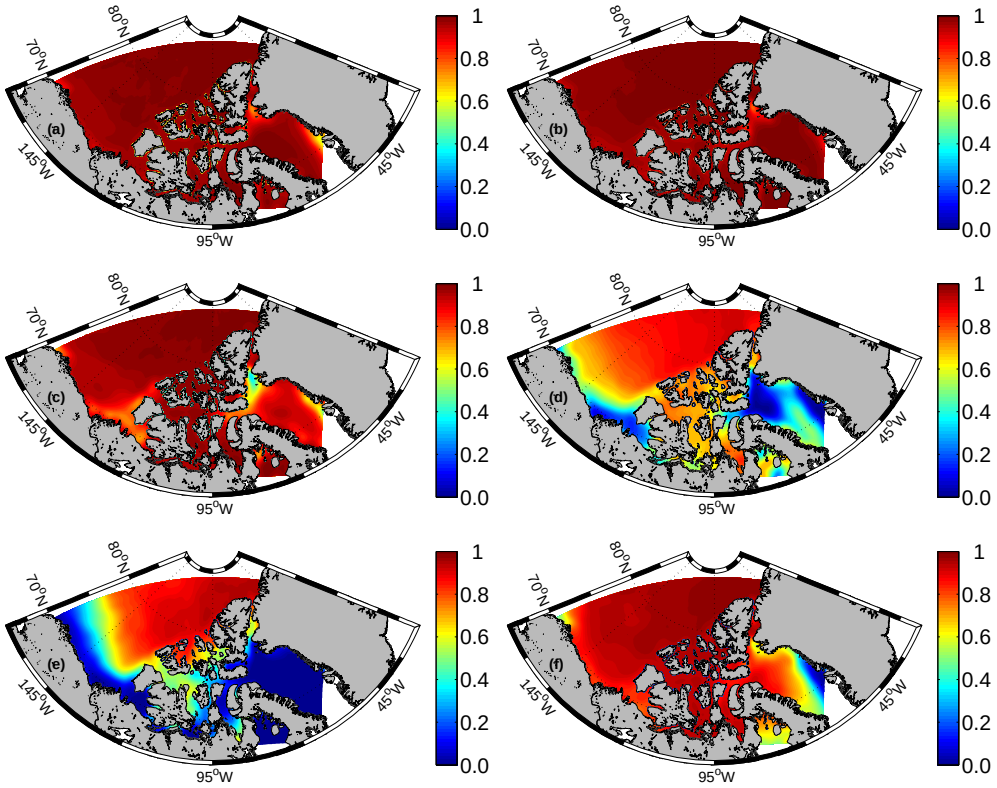

Figure 1.2: Mean sea ice concentration in (a) January (b) March (c) May (d) July (e) September (f) November for the period 1988-2004 from SSM/I (Special Sensor Microwave Imager).

Bibliography

Aagaard, K., and E. Carmack, 1989: The role of sea ice and other fresh water in the Arctic circulation. *Journal of Geophysical Research*, **94**, 14485–14498.

— 1994: The Arctic Ocean and climate: A perspective. *The Polar Oceans and Their Role in Shaping the Global Environment: The Nansen Centennial Volume*, O. M. Johannessen, R. D. Muench, and J. E. Overland, eds., Amer. Geophys. Union, USA, volume 85 of *Geophysical Monograph*, 4–20.

Agnew, T., A. Lambe, and D. Long, 2008: Estimating sea ice area flux across the Canadian Arctic Archipelago using enhanced AMSR-E. *Journal of Geophysical Research*, **113**, doi:10.1029/2007JC004582.

Aksenov, Y., S. Bacon, A. C. Coward, and P. N. Holliday, 2010: Polar outflow from the Arctic Ocean: A high resolution model study. *Journal of Marine System*, **83**, doi:10.1016/j.jmarsys.2010.06.007, 14–37.

Arrigo, K. R., G. van Dijken, and S. Pabi, 2008: Impact of a shrinking Arctic ice cover on marine primary production. *Geophysical Research Letters*, **35**, doi:10.1029/2008GL035028.

Barber, D., J. Hanesiak, W. Chan, and J. Piwowar, 2001: Sea-ice and meteorological conditions in Northern Baffin Bay and the North Water polynya between 1979 and 1996. *Atmosphere-Ocean*, **39**, 343–359.

Barry, R. G., 1993: Canada's cold seas. *Canada's cold environment*, H. M.

French and O. Slaymaker, eds., McGill Queen's University Press, Canada, NATO Science for Peace and Security Series, 29–61.

Canadian Ice Service, 2007: Canadian ice service archive documentation seriesregional charts: History, accuracy, and caveats. Ottawa.

Carmack, E., 2000: The Arctic Ocean's freshwater budget: Sources, storage and export. *The Freshwater Budget of the Arctic Ocean*, E. Lewis, E. Jones, T. Lemke, P.; Prowse, and W. P., eds., Kluwer Academic Publishers, The Netherlands, volume 7 of *NATO Science Series*, 91–126.

— 2007: The alpha/beta ocean distinction: A perspective on freshwater fluxes, convection, nutrients and productivity in high-latitude seas. *Deep Sea Research Part II*, **54**, doi:10.1016/j.dsr2.2007.08.018, 2578–2598.

Curry, R., and C. Mauritzen, 2005: Dilution of the northern North Atlantic Ocean in recent decades. *Science*, **308**, doi:10.1126/science.1109477, 1772–1774.

de Lange Boom, B., H. Melling, and R. A. Lake, 1987: Late winter hydrography of the northwest passage. *Canadian technical report of hydrography and ocean sciences*, Institute of Ocean Science, Washington, D.C, USA.

Dickson, R., B. Rudels, S. Dye, M. Karcher, J. Meincke, and I. Yashayaev, 2007: Current estimates of freshwater flux through Arctic and subarctic seas. *Progress in Oceanography*, **73**, doi:10.1016/j.pocean.2006.12.003, 210–230.

Fissel, D., J. Birch, H. Melling, and R. A. Lake, 1988: Non-tidal flows in the Northwest Passage. *Canadian Technical Report of Hydrography and Ocean Sciences*, Department of Fisheries and Oceans, Sidney, BC, Canada.

Fissel, D., D.D.Lemon, and J. Birch, 1982: Major features of the summer

near-surface circulation of western Baffin Bay, 1978 and 1979. *Arctic*, **35**, 180–200.

Holloway, G., and Z. Wang, 2009: Representing eddy stress in an Arctic Ocean model. *Journal of Geophysical Research*, **114**, doi:10.1029/2008JC005169.

Howell, S. E., A. Tivy, J. J. Yackel1, and S. McCourt, 2008: Multi-year sea-ice conditions in the western Canadian Arctic Archipelago region of the Northwest Passage: 1968-2006. *Atmosphere-Ocean*, **46**, doi:10.3137/ao.460203, 229–242.

Jones, E. P., and A. R. Coote, 1980: Nutrient distributions in the Canadian Archipelago: Indicators of summer water mass and flow characteristics. *Can. J. Fish. Aquat. Sci*, **37**, 589–599.

Kliem, N., and D. A. Greenberg, 2003: Diagnostic simulations of the summer circulation in the Canadian Arctic Archipelago. *Atmosphere-Ocean*, **41**, 273–289.

Kwok, R., 2005: Variability of Nares Strait ice flux. *Geophysical Research Letters*, **32**, doi:10.1029/2005GL024768.

Kwok, R., L. T. Pedersen, P. Gudmandsen, and S. S. Pang, 2010: Large sea ice outflow into the Nares Strait in 2007. *Geophysical Research Letters*, **37**, doi:10.1029/2009GL041872, 1363–1388.

McGeehan, T., and W. Maslowski, 2012: Evaluation and control mechanisms of volume and freshwater export through the Canadian Arctic Archipelago in a high-resolution pan-Arctic ice-ocean model. *Journal of Geophysical Research*, **117**, doi:10.1029/2011JC007261.

McLaughlin, F., E. Carmack, R. Ingram, W. Williams, and C. Michel, 2004:

Oceanography of the northwest passage. *The Sea*, A. Robinson and K. Brink, eds., Harvard University Press, New York, Vol 14, part B, 1211–1242.

Melling, H., 2000: Exchanges of freshwater through the shallow straits of the North American Arctic. *Freshwater Budget of the Arctic Ocean*, E. L. et al., ed., Kluwer Academic Publishers, The Netherlands, NATO Science Series, 479–502.

— 2002: Sea ice of the northern Canadian Arctic Archipelago. *Journal of Geophysical Research*, **107**, doi:10.1029/2001JC001102.

Melling, H., T. Agnew, K. K. Falkner, D. Greenberg, C. Lee, A. Mnchow, B. Petrie, S. Prisenberg, R. Samelson, and R. A. Woodgate, 2008: Freshwater fluxes via Pacific and Arctic outflows across the Canadian Polar Shelf. *Arctic-Subarctic Ocean fluxes, defining the role of the northern seas in climate*, R. R. Dickson, J. Meincke, and P. Rhines, eds., Springer, New York, 193–247.

Melling, H., R. Lake, D. Topham, and D. Fissel, 1984: Oceanic thermal structure in the western Canadian Arctic. *Continental Shelf Research*, **3**, doi:10.1016/0278-4343(84)90010-4, 233–258.

Muench, R., 1971: The physical oceanography of the northern Baffin Bay region. *The Baffin-North Water project, scientific report 1*, Arctic institute of north America, Washington, D.C, USA.

Münchow, A., and H. Melling, 2008: Ocean current observations from Nares Strait to the west of Greenland: Interannual to tidal variability and forcing. *Journal of Geophysical Research*, **66**, 801–833.

Münchow, A., H. Melling, and K. K. Falkner, 2006: An Observational Estimate of Volume and Freshwater Flux Leaving the Arctic Ocean through Nares

Strait. *Journal of Physical Oceanography*, **36**, doi:10.1029/2001JC001039, 2025–2041.

Prinsenberg, S. J., and E. Bennett, 1987: Mixing and transports in Barrow Strait, the central part of the Northwest passage. *Continental Shelf Research*, **7**, doi:10.1016/0278-4343(87)90006-9, 913–935.

— 1989: Transport between Peel Sound and Barrow Strait in the Canadian Arctic. *Continental Shelf Research*, **9**, doi:10.1016/0278-4343(89)90008-3, 427–444.

Prinsenberg, S. J., and J. Hamilton, 2005: Monitoring the Volume, Freshwater and Heat Fluxes Passing through Lancaster Sound in the Canadian Arctic Archipelago. *Atmosphere-Ocean*, **43**, doi:10.3137/ao.430101, 1–22.

Prinsenberg, S. J., J. Hamilton, I. Peterson, and R. Pettipas, 2009: Observing and interpreting the seasonal variability of the oceanographic fluxes passing through Lancaster Sound of the Canadian Arctic Archipelago. *Influence of Climate Change on the Changing Arctic and Sub-Arctic Conditions*, J. C. Nihoul and A. G. Kostianoy, eds., Springer, The Netherlands, NATO Science for Peace and Security Series, 125–143.

Rabe, B., H. L. Johnson, A. Münchow, and H. Melling, 2012: Geostrophic ocean currents and freshwater fluxes across the Canadian polar shelf via Nares Strait. *Journal of Marine Research*, submitted.

Rabe, B., A. Münchow, H. L. Johnson, and H. Melling, 2010: Nares Strait hydrography and salinity field from a 3-year moored array. *Journal of Geophysical Research*, **115**, doi:10.1029/2009JC005966.

Rudels, B., 1986: The outflow of polar water through the Arctic Archipelago and the oceanographic conditions in Baffin Bay. *Polar Research*, **4**, 161–180.

Serreze, M. C., A. P. Barrett, A. G. Slater, R. A. Woodgate, K. Aagaard, R. B. Lammers, M. Steele, R. Moritz, M. Meredith, and C. M. Lee, 2006: The large-scale freshwater cycle of the Arctic. *Journal of Geophysical Research*, **111**, doi:10.1029/2005JC003424.

Serreze, M. C., M. M. Holland, and J. Stroeve, 2007: Perspectives on the Arctic's shrinking sea ice cover. *Science*, **315**, doi:10.1126/science.1139426, 1533–1536.

Serreze, M. C., and J. C. Stroeve, 2008: Standing on the brink. *Nature reports climate change*, **2**, doi:10.1126/science.1139426, 142–143.

Shimada, K., T. Kamoshida, M. Itoh, S. Nishino, E. Carmack, F. McLaughlin, S. Zimmermann, and A. Proshutinsky, 2006: Pacific Ocean inflow: Influence on catastrophic reduction of sea ice cover in the Arctic Ocean. *Geophysical Research Letters*, **33**, doi:10.1029/2005GL025624.

Sou, T., and G. Flato, 2009: Sea ice in the Canadian Arctic Archipelago: Modeling the past (1950–2004) and the future (2041–60). *Journal of Climate*, **22**, doi:10.1175/2008JCLI2335.1, 2181–2198.

Steele, M., and W. Ermold, 2007: Steric sea level change in the Northern Seas. *Journal of Climate*, **20**, 403–417.

Stigerbrandt, A., 1984: The North Pacific: a global-scale estuary. *Journal of Physical Oceanography*, **14**, 464–470.

Stroeve, J., M. M. Holland, W. Meier, T. Scambos, and M. Serreze, 2007: Arctic sea ice decline: Faster than forecast. *Geophysical Research Letters*, **34**, doi:10.1029/2007GL029703.

Stroeve, J., M. Serreze, S. Drobot, S. Gearheard, M. Holland, J. Maslanik,

W. Meier, and T. Scambos, 2008: Arctic Sea Ice Extent Plummets in 2007. *Eos Trans*, **89**, doi:10.1029/2008EO020001, 13.

Tang, C. C., C. K. Ross, T. Yao, B. Petrie, B. M. DeTracey, and E. Dunlap, 2004: The circulation, water masses and sea-ice of Baffin Bay. *Progress in Oceanography*, **63**, doi:10.1016/j.pocean.2004.09.005, 183–228.

Terwisscha van Scheltinga, A., P. G. Myers, and J. D. Pietrzak, 2010: A finite element sea ice model of the Canadian Arctic Archipelago. *Ocean Dynamics*, **60**, doi:10.1007/s10236-010-0356-5, 1539–1558.

Chapter 2

Model description

2.1 Ocean model

2.1.1 Primitive Equations

The primitive equations are represented in a coordinate system with an orthogonal set of unit vectors ($\mathbf{i}$, $\mathbf{j}$, $\mathbf{k}$), in which $\mathbf{k}$ is the local upward vector and ($\mathbf{i}$, $\mathbf{j}$) are two vectors orthogonal to $\mathbf{k}$.

$$\frac{\partial \mathbf{U}_h}{\partial t} = -[(\bigtriangledown \times \mathbf{U}) \times \mathbf{U} + \frac{\bigtriangledown(\mathbf{U}^2)}{2}]_h - f\mathbf{k} \times \mathbf{U}_h - \frac{\bigtriangledown_h p}{\rho_0} + \mathbf{D}^{\mathbf{U}} + \mathbf{F}^{\mathbf{U}} \quad (2.1)$$

$$\frac{\partial p}{\partial z} = -\rho g \quad (2.2)$$

$$\bigtriangledown \cdot \mathbf{U} = 0 \quad (2.3)$$

$$\frac{\partial T}{\partial t} = - \bigtriangledown \cdot (T\mathbf{U}) + D^T + F^T \quad (2.4)$$

$$\frac{\partial S}{\partial t} = - \bigtriangledown \cdot (S\mathbf{U}) + D^S + F^S \quad (2.5)$$

$$\rho = \rho(T, S, p) \quad (2.6)$$

$\mathbf{U}$ is the velocity composed of a horizontal vector component($\mathbf{U_h}$) and a vertical vector component ($w\mathbf{k}$), the subscript h denotes the local horizontal vector, i.e. over the ($\mathbf{i}$, $\mathbf{j}$) plane, $\bigtriangledown$ is the generalised derivative vector operator in ($\mathbf{i}$,$\mathbf{j}$,$\mathbf{k}$) directions, t is the time, T is the potential temperature of the ocean, S the salinity of the ocean, ρ in situ density, ρ_0 a reference density of the ocean, g the gravitational acceleration, p the pressure and $f = 2\mathbf{\Omega}\mathbf{k}$ the Coriolis accleration ($\mathbf{\Omega}$ is the Earth's angular velocity vector). $\mathbf{F}^{\mathbf{U}}$, F^T, F^S are forcing

terms and $\mathbf{D}^{\mathbf{U}}$, D^T, D^S are the parameterizations of small scale physics for momentum, temperature and salinity correspondingly. More details can be found in Madec (2008).

2.1.2 Subgrid physics

Currently, the model resolution is coarser than the scale at which turbulence occurs and thus the turbulent motions are never explicitly resolved but always parameterized. Due to strong anisotropy between the vertical and lateral motion, the subgrid scale physics are divided into lateral and vertical parts. The vertical momentum and tracer diffusive operators are given as:

$$\mathbf{D}^{v\mathbf{U}} = \frac{\partial}{\partial z}(A^{vm}\frac{\partial \mathbf{U}_h}{\partial z}) \tag{2.7}$$

$$D^{vT} = \frac{\partial}{\partial z}(A^{vT}\frac{\partial T}{\partial z}) \tag{2.8}$$

$$D^{vS} = \frac{\partial}{\partial z}(A^{vT}\frac{\partial S}{\partial z}) \tag{2.9}$$

where A^{vm} and A^{vT} are the vertical eddy viscosity and diffusivity coefficients, respectively. Those coefficients are computed by a model based on a turbulent kinetic energy prognostic equation (Blanke and Delecluse, 1993).

The formulation of lateral eddy fluxes depends on whether the model resolution is higher than mesoscale or not (i.e. the model is eddy-resolving or not). More details on the sub-grid physics and its equations can be found in the Madec (2008).

2.1.3 Open boundary conditions

The radiation relaxation algorithm is used at the open boundary. First, we calculate a phase velocity to determine whether perturbations tend to propagate toward, or away from, the boundary. Now a model variable ϕ is considered, here ϕ stands for u and v. The phase velocity normal and tangential to the

boundary is

$$C_{\phi x} = \frac{-\phi_t}{(\phi_x^2 + \phi_y^2)}\phi_x \qquad C_{\phi y} = 0 \tag{2.10}$$

The new boundary values are updated differently depending on the sign of $C_{\phi x}$. In the following, an eastern boundary is considered as an example. The radiation condition, written for a model variable ϕ, is:

$$\phi_t = -C_{\phi x}\phi_x + \frac{1}{\tau_0}(\phi_c - \phi) \qquad (C_{\phi x} > 0), \tag{2.11}$$

$$\phi_t = \frac{1}{\tau_i}(\phi_c - \phi) \qquad (C_{\phi x} < 0), \tag{2.12}$$

where ϕ stands for u and v, ϕ_c is the estimate of ϕ at the boundary, provided as boundary data. It should be noted that, $C_{\phi x}$ is bounded by the ratio $\delta x/\delta t$ for stability reasons. When $C_{\phi x}$ is eastward (outward propagation), the radiation condition (2.11) is used. When $C_{\phi x}$ is westward (inward propagation), the radiation condition (2.12) is used, which means that the value of ϕ is strongly relaxed to a climatology value ϕ_c. Usually τ_i is 1 day. The temperature, salinity, and the ocean velocities at the boundary need to be provided. More details can be found in Madec (2008).

2.2 Sea ice model

Within the NEMO system the ocean model is interactively coupled with a sea ice model (the Louvain-la-Neuve (LIM)). LIM (version 2) is a simple 3-layer (one for snow, two for ice) model which includes thermodynamics and dynamic processes (Fichefet and Maqueda, 1997).

2.2.1 Ice thermodynamics

The vertical growth and decay of sea ice due to thermodynamics is governed by a one dimensional heat-diffusion equation (Fichefet and Maqueda, 1997):

$$\rho_c c_{pc}\frac{\partial T_c}{\partial t} = G(h_e)k_c\frac{\partial^2 T_c}{\partial z^2} \tag{2.13}$$

where ρ_c c_{pc}, and k_c are the density, the specfic heat and thermal conductivity, respectively; T_c is the temperature, t is the time, and z is the vertical coordinate, the subscript c represents either ice (i) or snow (s). $G(h_e)$ is a correction factor which represents the effects of the unresolved ice floes of varying thickness contributing differently to the conductive heat flux.

At the surface of the snow-ice system, the energy balance is given by:

$$F^{net}(T_{su}) = F^{sw}(1-\alpha)(1-i_0) + F^{\downarrow}_{lw} - \epsilon\sigma T^4_{su} - F^{sh} - F^{lh} + F_c \qquad (2.14)$$

where T_{su} is the surface (ice or snow) temperature, F_{sw} is the shortwave downwelling radiation reaching the ice surface, α is the surface albedo, i_0 is the fraction of the net shortwave radiation penetrating the ice, $F^{\downarrow}_{lw}$ is the downwelling longwave radiation, ϵ is the surface emissivity, σ is the Stefan-Boltzmann constant, F_{sh} and F_{lh} are the turbulent fluxes of sensible heat and latent heat, respetively, and F_c is conductive flux below the surface.

If $F^{net} \geq 0$, T_{su} is held at the melting point and melting occurs according to:

$$F^{net}(T) = -q\frac{dh_x}{dt} \qquad (2.15)$$

where q is the sea ice energy of melting and the subscripts x represents either snow or ice.

At the bottom of the ice slab, the temperature equals the freezing point of seawater. At the bottom of the ice slab, the energy balance is given by:

$$F_w - F_c = -q\frac{dh_i}{dt} \qquad (2.16)$$

where F_w is the heat flux from the ocean, F_c is the conductive flux from the bottom of sea ice, h_i is ice thickness.

Now we consider the lateral growth and decay of the sea ice. To take into consideration the existence of leads and polynyas within the ice pack, the ice

concentration variable A, which is the percentage of each cell which is covered by sea ice, is introduced.

The thermodynamic variations of A depend on the heat budget of the open water B_l. If B_l is negative, the change of A is given by the following equation (Fichefet and Maqueda, 1997):

$$\left(\frac{\partial A}{\partial t}\right)_{increase} = (1 - A^2)^{\frac{1}{2}} \frac{(1 - A)B_l}{L_i h_0} \tag{2.17}$$

where h_0 is thickness of the newly formed sea ice, L_i represents the volumetric latent heat of fusion of sea ice.

If one assumes that the ice is uniformly distributed in thickness between 0 and $2h_i$ (where h_i represents ice thickness) over the ice covered portion of the grid cell and that the melting rate does not depend on the local ice thickness, reduction of ice concentration caused by vertical melting is given by the following equation:

$$\left(\frac{\partial A}{\partial t}\right)_{decrease} = -\frac{A}{2h_i}\Gamma\left[-\left(\frac{\partial h_i}{\partial t}\right)\right] \tag{2.18}$$

where Γ is the Heaviside unit function. More details can be found in Fichefet and Maqueda (1997).

2.2.2 Ice dynamics

Ice moves under the influence of winds and ocean currents. The force balance per unit area in the ice pack is given by a two-dimensional momentum equation:

$$m\frac{\partial \mathbf{u}}{\partial t} = \bigtriangledown \cdot \boldsymbol{\sigma} - mf\mathbf{k} \times \mathbf{u} + A(\boldsymbol{\tau}_{ai} + \boldsymbol{\tau}_{wi}) - mg \bigtriangledown H_0 \tag{2.19}$$

where m is the ice mass per unit area, $\mathbf{u}$ is the ice velocity, $\boldsymbol{\sigma}$ is the internal stress tensor, A is the ice concentration, $\boldsymbol{\tau}_{ai}$ is the wind stress on the sea ice, $\boldsymbol{\tau}_{wi}$ is the water stress on the sea ice, H_0 is the ocean surface elevation with respect to zero sea level.

The elastic-viscous-plastic (EVP) ice rheology (Hunke and Dukowicz, 1997), is used in the model. σ_{11}, σ_{22}, σ_{12} are the components of the ice internal stress tensor, and let:

$$\sigma_1 = \sigma_{11} + \sigma_{22}, \tag{2.20}$$

$$\sigma_2 = \sigma_{11} - \sigma_{22}, \tag{2.21}$$

$$D_D = \frac{1}{h_1 h_2}\left(\frac{\partial}{\partial \xi_1}(h_2 u) + \frac{\partial}{\partial \xi_2}(h_1 v)\right), \tag{2.22}$$

$$D_T = \frac{1}{h_1 h_2}\left(h_2^2 \frac{\partial}{\partial \xi_1}(u/h_2) - h_1^2 \frac{\partial}{\partial \xi_2}(v/h_1)\right), \tag{2.23}$$

$$D_S = \frac{1}{h_1 h_2}\left(h_1^2 \frac{\partial}{\partial \xi_2}(u/h_1) + h_2^2 \frac{\partial}{\partial \xi_1}(v/h_2)\right), \tag{2.24}$$

where D_D, D_T, D_S, are the divergence, horizontal tension, and shearing strain rates, respectively, ξ_1, ξ_2 are generalized orthogonal coordinates, and h_1 and h_2 are the associated scale factors.

With these definitions, the stress tensor is given by

$$2T\frac{\partial \sigma_1}{\partial t} + \sigma_1 = \left(\frac{D_D}{\triangle} - 1\right)P, \tag{2.25}$$

$$\frac{2T}{e^2}\frac{\partial \sigma_2}{\partial t} + \sigma_2 = \frac{D_T}{e^2 \triangle}P, \tag{2.26}$$

$$\frac{2T}{e^2}\frac{\partial \sigma_{12}}{\partial t} + \sigma_{12} = \frac{D_S}{2e^2 \triangle}P, \tag{2.27}$$

where T is a time scale that controls the rate of damping of elastic waves. P is the ice compressive strength, e is the ratio of principle axes of the elliptical yield curve and $\triangle$, a measure of the deformation rate, is given by

$$\triangle = [D_D^2 + \frac{1}{e^2}(D_T^2 + D_S^2)]^{\frac{1}{2}}, \tag{2.28}$$

The ice strength P is related to the ice thickness per unit area, h, and ice concentration, A, by $P = P^* h e^{-C(1-A)}$, where P^* and C are empirical constants.

The VP model (Hibler, 1979) is recovered at steady state:

$$\sigma_1 = (\frac{D_D}{\triangle} - 1)P, \tag{2.29}$$

$$\sigma_2 = \frac{D_T}{e^2\triangle}P, \tag{2.30}$$

$$\sigma_{12} = \frac{D_S}{2e^2\triangle}P, \tag{2.31}$$

The components of the internal stress force are (Hunke and Dukowicz, 2002):

$$2F_1 = \frac{1}{h_1}\frac{\partial\sigma_1}{\partial\xi_1} + \frac{1}{h_1h_2^2}\frac{\partial(h_2^2\sigma_2)}{\partial\xi_1} + \frac{2}{h_1^2h_2}\frac{\partial(h_1^2\sigma_{12})}{\partial\xi_2}, \tag{2.32}$$

$$2F_2 = \frac{1}{h_2}\frac{\partial\sigma_1}{\partial\xi_2} + \frac{1}{h_1^2h_2}\frac{\partial(h_1^2\sigma_2)}{\partial\xi_2} + \frac{2}{h_1h_2^2}\frac{\partial(h_2^2\sigma_{12})}{\partial\xi_1}, \tag{2.33}$$

Numerically, this is done on a C-grid (Bouillon et al., 2009). The C grid version of the sea ice model has several advantages: (a) easier coupling with NEMO, which is itself defined on a C grid; (b) possibility of representing ice transport across narrow straits; (c) better representation of inertial plastic compressive waves.

2.2.3 Continuity equations

Local changes, in the physical fields which are advected (sea ice concentration, the snow and ice volume per unit area, the snow and ice enthalpy per unit area, and the latent heat contained in the brine reservoir per unit area), are computed from the following conservation law:

$$\frac{\partial\Psi}{\partial t} = -\bigtriangledown\cdot(\mathbf{u}\Psi) + D\bigtriangledown^2\Psi + S_\Psi \tag{2.34}$$

where Ψ represents any of the variable listed above, S_Ψ is the rate of change of Ψ due to thermodynamics, and D is a horizontal diffusivity. The diffusion term used in (2.34) is used to avoid nonlinear instabilities in numerical simulations. More details can be found in the Fichefet and Maqueda (1997).

2.2.4 Ice boundary condition

When the sea ice motion is inward at the boundary, the ice concentration and ice thickness is set to a known exterior value. When the sea ice motion is outward at the boundary, the no gradient boundary for sea ice concentration and ice thickness is used. Let us use an east boundary as an example:

$$\psi_b = \psi_{ext} \qquad (u < 0) \tag{2.35}$$

$$\psi_{b-1} = \frac{1}{2}(\psi_{ext} + \psi_{b-2}) \qquad (u < 0) \tag{2.36}$$

$$\psi_b = \psi_{b-2} \qquad (u > 0) \tag{2.37}$$

$$\psi_{b-1} = \psi_{b-2} \qquad (u > 0) \tag{2.38}$$

where ψ can represent sea ice concentration and ice thickness, ψ_{ext} represent exterior value of ψ, subscript $_b$ indicates the boundary point, and subscripts $_{b-1}$ and $_{b-2}$ indicate grid points before the boundary.

2.3 Ice-ocean coupling

The coupling between the sea ice and ocean models uses the equations presented by Goosse and Fichefet (1999). The water stress on the sea ice (τ_{wi}) is:

$$\tau_{wi} = \rho_0 c_{wi} |\mathbf{u_w} - \mathbf{u_i}| (\mathbf{u_w} - \mathbf{u_i}), \tag{2.39}$$

where u_i and u_w are the ice velocity and the ocean surface velocity, respectively, ρ_0 is a reference seawater density and c_{wi} is the water-ice drag coefficient.

The sensible heat from the ocean to the ice (F_{wi}) is set to be propotional to the difference of temperature between the surface layer (T_w), and its freezing point (T_{Freeze}):

$$F_{wi} = \rho_0 c_{pw} c_h u_* (T_w - T_{Freeze}), \tag{2.40}$$

where u_* is the friction velocity, c_{pw} is the specfic heat of seawater, and c_h is a coefficient.

The salt flux between the ice and ocean is given by:

$$F_{salt} = S_w \left(\frac{\partial m_s}{\partial t} \right) + (S_w - S_i) \left(\frac{\partial m_i}{\partial t} \right), \tag{2.41}$$

where S_w and S_i are the seawater reference salinity and the sea ice salinity, and m_s and m_i are the masses of snow and ice per unit area, respectively. The first term on the right hand side of (2.41) is the salt flux associated with ice growth and melt. The second term represents the freshwater flux due to ice formation and melting. More details can be found in the Fichefet and Maqueda (1997).

Bibliography

Blanke, B., and P. Delecluse, 1993: Variability of the tropical Atlantic Ocean simulated by a general circulation model with two different mixed-layer physics. *Journal of Physical Oceanography*, **23**, 1363–1388.

Bouillon, S., M. A. M. Maqueda, V. Legat, and T. Fichefet, 2009: An elasticviscousplastic sea ice model formulated on Arakawa B and C grids. *Ocean Modelling*, **27**, doi:10.1016/j.ocemod.2009.01.004, 174–184.

Fichefet, T., and M. M. Maqueda, 1997: Sensitivity of a global sea ice model to the treatment of ice thermodynamics and dynamics. *Journal of Geophysical Research*, **102**, 12609–12646.

Goosse, H., and T. Fichefet, 1999: Importance of ice-ocean interactions for the global ocean circulation: a model study. *Journal of Geophysical Research*, **104**, 23337–23355.

Hibler, W. D., 1979: A Dynamic Thermodynamic Sea Ice Model. *Journal of Physical Oceanography*, **9**, 817–846.

Hunke, E., and J. Dukowicz, 1997: An Elastic-Viscous-Plastic for sea ice dynamics. *Journal of Physical Oceanography*, **27**, 1849–1867.

— 2002: The ElasticViscousPlastic Sea Ice Dynamics Model in General Orthogonal Curvilinear Coordinates on a Sphere-Incorporation of Metric Terms. *Monthly weather review*, **130**, 1848–1865.

Madec, G., 2008: NEMO Ocean Engine. Institut Pierre-Simon Palace (IPSL), France, volume 27 of *Notes de Pole de modelisation*.

Chapter 3

Model configuration and validation

3.1 Model configuration

We use a CAA configuration of version 3.1 of the Nucleus for European Modeling of the Ocean (NEMO) Ocean/Sea-Ice general circulation model numerical code (Madec, 2008) including the Louvain-la-Neuve sea-ice model (LIM2) (Fichefet and Maqueda, 1997) in which ice dynamics are updated with an elastic-viscous-plastic (EVP) rheology (Hunke and Dukowicz, 1997) implemented on a C-grid (Bouillon et al., 2009).

The CAA configuration has 46 levels in the vertical, with thicknesses from 6 m at the surface to 250 m at the bottom. A partial step representation of bathymetry is used. The configuration uses a linear free surface formulation, Laplacian horizontal viscosity, non-linear bottom boundary friction, and a turbulence closure scheme (order 1.5) for vertical mixing (Blanke and Delecluse, 1993).

The CAA configuration was spun up from September 1, using initial climatological temperature and salinity based on the Polar science center Hydrographic Climatology (PHC) 3.0 data set (Steele et al., 2001) and run under climatological forcing (normal year forcing). The coupled sea ice-ocean model is forced with 6-hourly surface air temperature, specific humidity and 10 m

winds, daily radiative fluxes, monthly precipitation and snow from Large and Yeager (2004) (hereafter LY04). Normal year forcing data is used in the configurations. Turbulent fluxes at the sea surface are implemented according to the CORE (Coordinated Ocean Reference Experiments) strategy, utilizing the bulk forcing methodology for global ocean ice models developed by Large and Yeager (2004). Surface albedo is parameterized following Shine and Henderson-Sellers (1985). At the ocean boundaries we need data for temperature, salinity and the velocities (Madec, 2008). A detailed description of the numerics of the open boundaries is found in Treguier et al. (2001).

The CAA model domain is shown in Figure 3.1. A tri-polar grid (Murray, 1996) is used in the horizontal, with one pole situated in the Pacific Ocean near Alaska and one pole situated in the northern Atlantic Ocean near Greenland. There are 446 $\times$ 268 points in the horizontal and the model resolution varies between 6.5 km and 9.5 km, with 7.5 km in Lancaster Sound. The bathymetry in CAA model is obtained from International Bathymetric Chart of the Arctic Ocean (IBCAO) (Jakobsson et al., 2008). The water depth in Bellot Strait, which is located between Somerset Island and Boothia Peninsula, is set to 17 m according to Melling (2000) (Figure 3.2). The bathymetry is smoothed with a Shapiro filter. There is a relaxation to the PHC climatology for sea surface salinity. The coefficient (0.167 m/day) amounts to a decay time of 60 days for 10m of water depth; under the ice cover restoring is 5 times stronger. No restoring to the sea surface temperature is applied. Some parameters of the coupled ice-ocean model are given in Table 1.

There are two boundaries. To the east, the boundary is located in Baffin Bay. To the north, the model is connected to the Arctic Ocean and Chukchi Sea. The monthly temperature, salinity, and the ocean velocities at the boundary is provided from a global model with a 1° horizontal resolution (Holloway and Wang, 2009) and were averaged over years 1958-2004. In northern Foxe

Basin, a closed boundary is used. According to observations, the volume transport through the Fury and Hecla Strait is between 0.04 Sv (Sadler, 1982) and 0.1 Sv (Barber, 1965).

The monthly sea ice boundary data (ice velocities, ice concentration and ice thickness) is derived from Pan-Arctic Ice-Ocean Modeling and Assimilation System (PIOMAS) data sets (Zhang and Rothrock, 2003). The monthly data is averaged over 1978-2004. The initial ice concentration is the mean ice concentration on September 1 from 1984 to 2004 derived from SMM/I data sets (Cavalieri et al., 2008). The initial ice thickness is 2 m. In Nares Strait, the ice velocity is set to zero from early February to mid July according to Kwok et al. (2010) in order to simulate the ice bridging in Nares Strait. The CAA control experiment ran for 8 years. Unless specified otherwise, mean quantities for the CAA configuration in this paper will refer to averages over years 6-8.

Because the mountainous topography in the northern Archipelago is not resolved by the NCEP/NCAR (National Centers for Environmental Prediction/National Center for Atmospheric Research) model, surface air temperatures over Nares Strait and much of the Archipelago in the NCEP/NCAR reanalysis are too cold in summer and represent high-altitude glaciers of Greenland and Ellesmere Island (Sou and Flato, 2009). The LY04 surface air temperature is based on NCEP/NCAR reanalysis (Large and Yeager, 2004). Although the NCEP/NCAR surface air temperatures are corrected monthly by the mean monthly climatological difference between the IABP/POLES (International Arctic Buoy Program/Polar exchange at the Sea Surface) dataset (Rigor et al., 2000) and NCEP/NCAR reanalysis over the Arctic cap north of 70°N (Large and Yeager, 2004), the revision did not consider the spatial variability of surface air temperature. Thus, for the CAA configuration, the LY04 surface air temperatures are adjusted again using IABP/POLES data, the

same approach as Sou and Flato (2009). Our adjustment removes the monthly climatological differences between the LY04 and IABP/POLES dataset in the normal year forcing. There are still large difference around Nares Strait, with the difference larger than 2.5°C in August (Figure 3.3) and September.

Downwelling shortwave radiation (DSR) is a major term in the surface heat budget and is an important factor that controls the sea ice melting and growth (Maykut and Untersteiner, 1971). The LY04 DSR is based on the ISCCP (International Satellite Cloud Climatology Project) dataset which was created using a GCM (General Circulation Model) radiative transfer model (Large and Yeager, 2004). We compare the DSR from LY04 with DSR from the Arctic Global Radiation (AGR) dataset (Box et al., 1998). In AGR, the DSR is obtained from land stations, ocean drifting stations and empirically derived long-term climatological estimates from earlier Russian studies (Serreze et al., 1998). The ocean drifting stations include Soviet North Pole drifting ice stations (Marshunova and Mishin, 1994) and U.S. drifting stations (ice island "T-3 ", "Arils II ") (Marshunova and Chernigovskii, 1971; Weller and Holmgren, 1974; Roulet, 1969).

Both the DSR from the AGR dataset (Figure 3.4) and LY04 (Figure 3.4) show that in June, the DSR is high over the Greenland ice sheet and is relatively low over the central and southern archipelago. The DSR is high over the Greenland ice sheet because of the elevation effect on atmospheric path length and the tendency for the high central portions of the ice sheet to be above the bulk of the cloud cover (Serreze et al., 1998). In summer, the DSR decreases away from the North Pole when the latitude is less than 70°N because of the combined effects of day length and solar zenith angle (Serreze et al., 1998). The DSR difference between the AGR data and LY04 (Figure 3.4c), which is above 60 W m^{-2}, in June is highest in northern Baffin Bay. The DSR difference between AGR data and LY04 in northern Baffin Bay is also above 60

W m^{-2} in May, and still $\sim$ 30 W m^{-2} in July and August. An interpolation was used to map the irregularly spaced data to data on the regular grid of AGR data (Serreze et al., 1998), which may lead to errors. However, since there are several observational sites around northern Baffin Bay (Serreze et al., 1998), LY04's underestimation of the DSR around northern Baffin Bay is likely real. This leads to too small heat fluxes and too much sea ice in summer. Since the AGR dataset covers our the CAA configuration's domain, we use this data for our shortwave radiation. The monthly mean AGR data value is used as the forcing for every day in a given month.

After a 5 year model run under normal year forcing, the model is run under the interannual year forcing. For the interannual year run, the CORE surface air temperatures are adjusted using IABP/POLES (International Arctic Buoy Program/Polar exchange at the Sea Surface) data, the same approach as Sou and Flato (2009). Our adjustment simply removes the monthly difference between the CORE and IABP/POLES dataset. The downwelling shortwave radiation data is corrected using the Arctic Global Radiation dataset by the following methods: Interannual year daily DSR = daily CORE data + monthly climatology AGR data - monthly normal year CORE data.

3.2 Model Evaluation

Focusing on the regions important for our scientific questions (McClure Strait through to Lancaster Sound, in the central archipelago), the model results will show that they agree rather well with the observations and allow us to use the model fields to explain the relevant dynamics.

3.2.1 Sea ice

Sea ice concentration is an important parameter to be examined because there are satellite measurements to validate the model's performance. Figure 3.5a

and 3.5b compare the 1984-2004 mean sea ice concentration fields in July derived from SMMR (August 1984-1987) and SMM/I (September 1987-2004) data sets (Cavalieri et al., 2008) with the results of the CAA control experiment. Overall, the spatial pattern of the model simulated sea ice concentration is consistent with satellite measurements. The North Water Polynya, located in northern Baffin Bay between Ellesmere Island and Greenland, is an important habitat for wildlife. The model simulated spatial patterns of the North Water Polynya is similar to observed patterns (Figure 3.5).

In McClure Strait and Viscount Melville Sound, the sea ice is nearly stagnant from December to May while the sea ice moves eastward in eastern Lancaster Sound. The observational results also show that the sea ice is landfast in western Parry Channel from December to May and the sea ice can move in eastern Parry channel (Agnew et al., 2008). Here the sea ice concentration in July is used because the sea ice concentration in Baffin Bay is better simulated after correcting the DSR from AGR dataset. In southeastern Baffin Bay, the sea ice concentration is low because of the warm West Greenland Current. The air temperature gradient seems play more important than the water temperature (Barber et al., 2001) to keep the ice thinner on the eastern side. In the southern Beaufort Sea, there is the Cape Bathurst polynya, which is located in Amundsen Gulf, as the wind drives the sea ice westward in July. In September, both modeled results and observed results show that Baffin Bay is nearly ice free (Figure 3.6). But the modeled sea ice concentration overestimates the observed results. Both model results and observational data show that Baffin Bay is nearly ice free in August and September (Figure 3.6) and the sea ice gradually expands to cover the whole model domain by January (not shown here). In November, both the model results and observations show that the model domain is covered by sea ice except eastern Baffin Bay although the model results overestimate the sea ice extent in eastern Baffin Bay (Figure

3.7). Both model results and observations show that the sea is covered by sea ice in November.

Another important aspect of sea ice is its thickness. In April, the modeled ice thickness is highest near the coast to the northwest of the Queen Elizabeth Islands, which is consistent with observational results (Bourke and Garrett, 1987; Melling, 2002). The ice thickness reduces from the west coast of Prince Patrick Island to the Beaufort Sea north of Alaska (Figure 3.8). The ice thickness also reduces with latitude from northwest of the Queen Elizabeth Islands to Parry Channel (Figure 3.8). The difference of ice thickness from February to May in most of the model domain is less than 0.5 m. Table 1 shows some observations of ice thickness compared to modelled ice thickness. The modelled ice thickness compares well with those found in the observations in most regions. Interannual variability in ice thickness may affect the comparison. For example, the ice thickness ranges from 0.9 m to 2 m at Clyde River in April.

3.2.2 Ocean currents

There is southeastward flow through McClure Strait. Part of the current through McClure Strait comes from the southern Beaufort Sea, while part of the inflow comes from a southwestward flow north of CAA. The core of the current is on the north side in McClure Strait and diverts to the southern side in eastern Viscount Melville Sound (Figure 3.9). The current that originates north of the archipelago also flows southward into Parry Channel via Byam Martin Channel and Penny Strait, with the surface velocities in the range of 2-9 cm s^{-1}. Near the northern entrance of M'Clintock Channel, part of the current from McClure Strait bifurcates into M'Clintock Channel and then flows into Peel Sound via Franklin Strait. The southward surface current peaks at 7 cm s^{-1} in northwestern M'Clintock Channel.

The current through Barrow Strait intrudes into northern Peel Sound as a cyclonic current loop (Figure 3.10). The mean volume transport through Peel Sound in April is 0.19 Sv in the CAA control experiment, which are similar to a previous estimate (0.15 Sv) (Prinsenberg and Bennett, 1989). As the sill in Dolphin and Union Strait is 26 m in the IBCAO dataset, the mean volume transport through Dolphin and Union Strait is 0.02 Sv in the CAA control experiment. The water flow through Peel Sound has mainly gone through M'Clintock Channel. In eastern Barrow Strait, the core of the eastward current is located on the south side (Figure 3.11). The model currents show a jet just off the shelf break at the south side in April, with velocities decreasing to the north (Figure 3.11), as seen by Prinsenberg and Bennett (1987). Velocities at 50 m are $\sim$ 13 cm s^{-1}, close to the observed maximum (Prinsenberg and Bennett, 1987), albeit the model maximum of 18 cm s^{-1} is at the surface. Based on a section through western Lancaster Sound coincident with the moorings of Prinsenberg and Hamilton (2005), the long term mean volume transport is 0.77 Sv in the CAA control experiment, slightly larger than the 0.7 Sv (with interannual variations of $\pm$ 0.3 Sv), based on observations (Prinsenberg et al., 2009).

3.2.3 Seasonal circulation

The sea level is high on the Mackenzie Shelf and Alaskan Beaufort Shelf and is low in central Baffin Bay (Figure 3.12). The West Greenland Current is relatively stronger in September than that in March in northern Baffin Bay (Figure 3.14). Therefore, the sea along the Greenland Coast in northern Baffin Bay is relatively high in September compared with that in March (Figure 3.12). In Parry Channel, the cross channel sea level gradient (Figure 3.13) is higher in September than that in March because of stronger currents in September (Figure 3.15).

Both modeled results and observed results show that the modeled seasonal volume transport increases from April to August and decrease from August to December (Figure 3.16). The observed volume transport is about 0.9 Sv in August and is about 0.2 Sv in November and December, while the modeled volume transport is about 0.8 Sv in August and is about 0.5 Sv in December. The modeled volume transport in winter is higher than the observed volume transport. There are several reasons that may cause this. One of them is that the surface pressure is not considered in the model and it might have an impact on the model results. Another possible reason is that the wind field in the Parry Channel might not be accurate due to coarse resolution and this might have an influence on the model results. The third possible reason is that the model underestimates the southward sea ice motion west of Banks Island in November, thus overestimating the sea level height at the western entrance of Parry Channel.

The volume transports through M'Clure Strait, M'Clintock Channel and Peel Sound increase from April to August and decreases from September to October (Figure 3.17). The volume transport through Byam Martin Channel increases from August to November but the variation is smaller than that in M'Clintock Channel and Peel Sound (Figure 3.17).

3.2.4 Temperature and Salinity distribution and mixed layer depth

Figure 3.18 shows climatology sea surface temperature (hereafter SST) from the PHC 3.0 data set (Steele et al., 2001) in the CAA in (a) March, (b) September. In March, the SST is relatively high near the Alaskan and Canadian coast and is between -1.8°C and -2.0°C in other regions. In September, the SST is relatively high at eastern Baffin Bay because of the warm West Greenland Current. The SST is also relatively high in the Amundsen Gulf.

The modeled SST is also between -1.8°C and -2.0°C in March in most regions (Figure 3.19). In September, the modeled SST is relatively high in eastern Baffin Bay and Amundsen Gulf (Figure 3.19), similar to the climatology SST. The temperature at 100 m is relatively high on the eastern side of Baffin Bay and in central Baffin Bay for both March and September (Figure 3.20).

Figure 3.21 shows sea surface salinity (hereafter SSS) in the CAA in March and September. In March and September, the SSS is relatively low in western Baffin Bay because relatively fresh water from Parry Channel flows along the coast of Baffin Island. In September, the SSS is relatively high in eastern Baffin Bay because of the warm West Greenland Current carrying saltier waters from the Irminger Current. In September, the SSS is relatively low on the Mackenzie Shelf because of Mackenzie River. The salinity at 100 m is relatively low in Peel Sound, Prince Regent Inlet, and the south side of Lancaster Sound both in March and September (Figure 3.22).

The maximum mixed layer depth in Baffin Bay occurs in April. The mixed layer depth is greater than 100 m in the center of northern Baffin Bay (Figure 3.23). The mixed layer depth is greater than 80 m in western and central Baffin Bay. On the Alaskan Beaufort Shelf and the Makenzie Shelf, the mixed layer depth is less than 20 m.

3.3 Sensitivity experiments

First we use two sensitivity experiments to see the effect of the ice bridge on the sea ice concentration in northern Baffin Bay. Ice bridges along the strait usually form some time between December and March at the entrance to Robeson Channel and southern Kane Basin (Kwok, 2005; Kwok et al., 2010). The model could not simulate an ice bridge if $e = 2$, here e is the principal axis ratio of the plastic yeild curve (Dumont et al., 2009). Dumont et al. (2009) reduced the value of e and successfully simulated the ice bridge in Nares Strait.

Here a different way is used to parameterize the sea ice bridge in Nares Strait in order to simulate the sea ice concentration better in Nares Strait. During periods when the ice bridges was observed to be present, the sea ice velocity is set to zero in Nares Strait. Figure 3.24 shows the position of the ice bridge in Nares Strait. The ice velocity in the box in Nares Strait in Figure 3.24 is set to zero between Feburary 2 and July 17. Feburary 2 is choosen because the average date that the south ice bridge forms is February 2 (Kwok et al., 2010). Since the ice bridge normally breaks up in July and August (Kwok, 2005), we set the ice bridge break up on July 17.

Figures 3.25 and 3.26 show the modeled sea ice concentration in July 2000 when there is no ice bridge in Nares Strait and there is an ice bridge in Nares Strait, respectively. In these two experiments, the downwelling shortwave radiation from CORE data are used. When there is no ice bridge, the sea ice concentration is high in western Nares Strait while it is relatively low in eastern Nares Strait. This pattern does not agree with the observed sea ice concentration under normal year forcing (Figure 3.5). The ice bridge in the southern Kane Basin stops the inflow of ice from the north and the sea ice concentration is low south of ice bridge (Figure 3.5). When there is an ice bridge, the sea ice concentration is low in southern Nares Strait which is similar as the observed sea ice concentration under normal year forcing (Figure 3.5).

Second, two sensitivity experiments were used to show that the use of downwelling shortwave radiation can improve the simulation of sea ice concentration in northern Baffin Bay. Figure 3.27 and Figure 3.28 show the sea ice concentration in July 1998 when the DSR from CORE data and AGR data are used, respectively. When the CORE data is used, the sea ice concentration is above 50% in northern Baffin Bay in July 1998. In July, observed sea ice concentration shows that a large area in the northwest, stretching from Smith

Sound to Lancaster Sound, becomes ice-free. Therefore, the model overestimates sea ice concentration in northern Baffin Bay (Figure 3.29). It is because the DSR from CORE data is smaller than the DSR from AGR data from May to July which we have mentioned previously in this chapter. In order to simulate sea ice concentration better, the DSR from AGR dataset instead of CORE dataset is used. When the DSR from AGR dataset is used, both the modeled and observed sea ice concentration in July 1998 is low from southern Nares Strait to east entrance of Lancaster Sound (Figure 3.28). When the DSR from AGR dataset is used, both modeled and observed results show that the sea ice concentration is relatively high in central Baffin Bay in July 1998 (Figure 3.28 and Figure 3.29). Therefore, the DSR from AGR dataset is better than the DSR from CORE dataset.

Table 3.1: Observed ice thickness and modeled ice thickness (m).

Location	Observation	CAA control experiment
Mackenzie Shelf (April)	2 (Melling et al., 2005)	2.5
Queen Elizabeth Islands region (March-May)	3.4 (1.6-5.5) (Melling, 2002)	2.5-4.5
McClure Strait (Feburary)	4.2 (McLaren et al., 1984)	3
Northern Peel Sound (April)	1.9 (Prinsenberg and Bennett, 1989)	2
Clyde River (April)	1.5 ± 0.3 (Tang et al., 2004)	1.5
Lincoln Sea (May)	4.7 ± 2.2 (2004); 5.2 ± 2.4 (2005) (Haas et al., 2006)	4.5

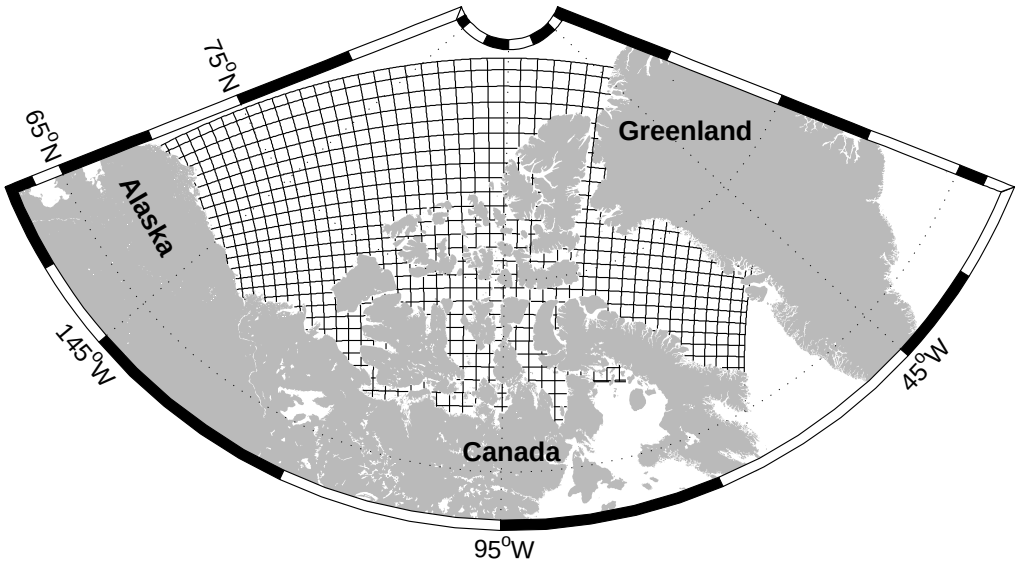

Figure 3.1: The CAA grid.

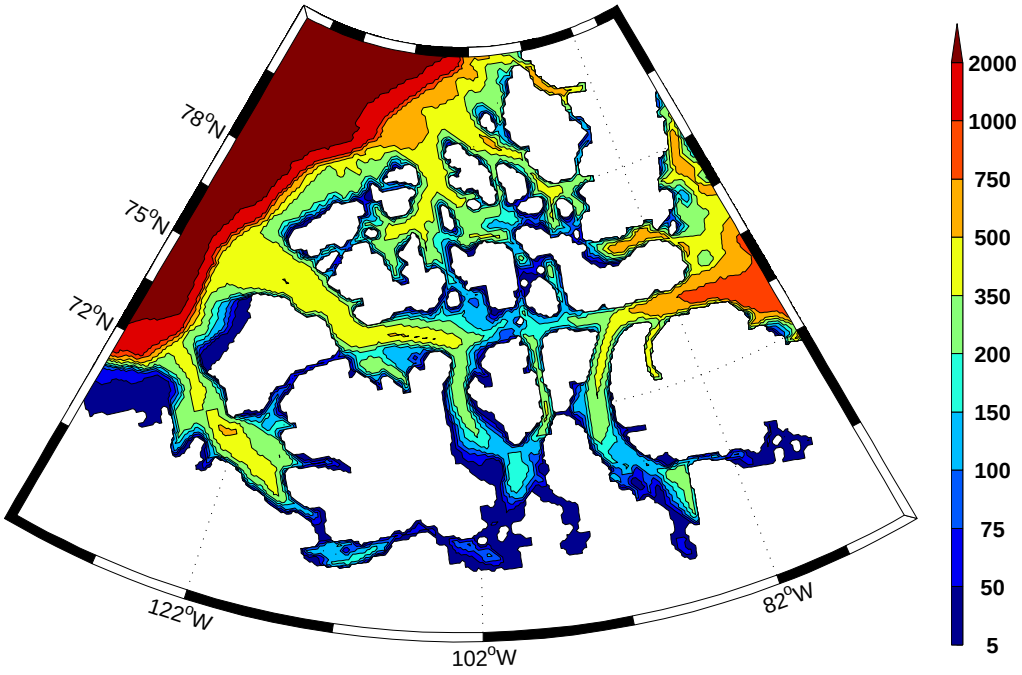

Figure 3.2: Bathymetry [m] in CAA control experiment.

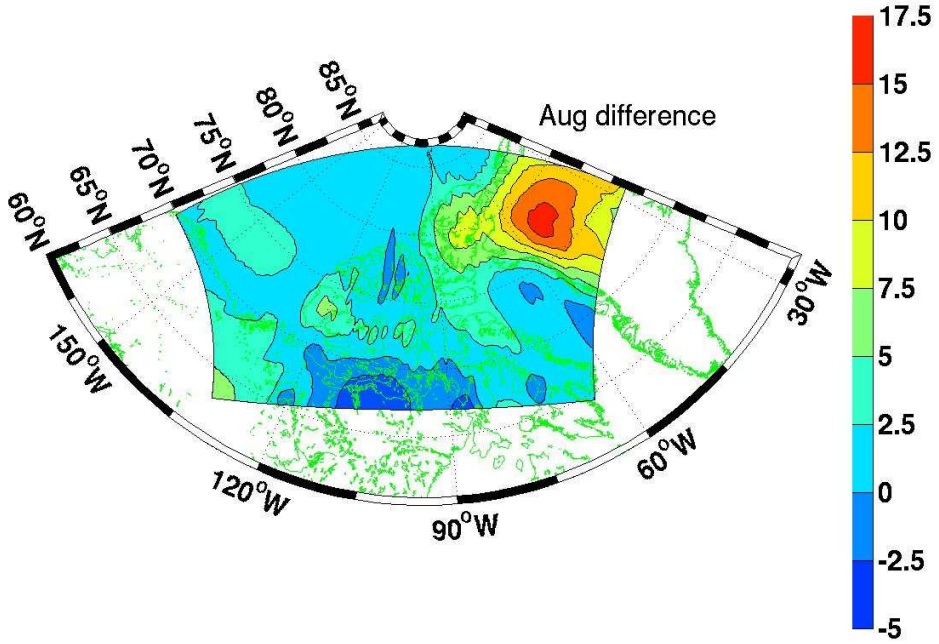

Figure 3.3: The surface air temperature difference [^{0}C] between the IABP/POLES dataset and Large and Yeager (2004) dataset for August.

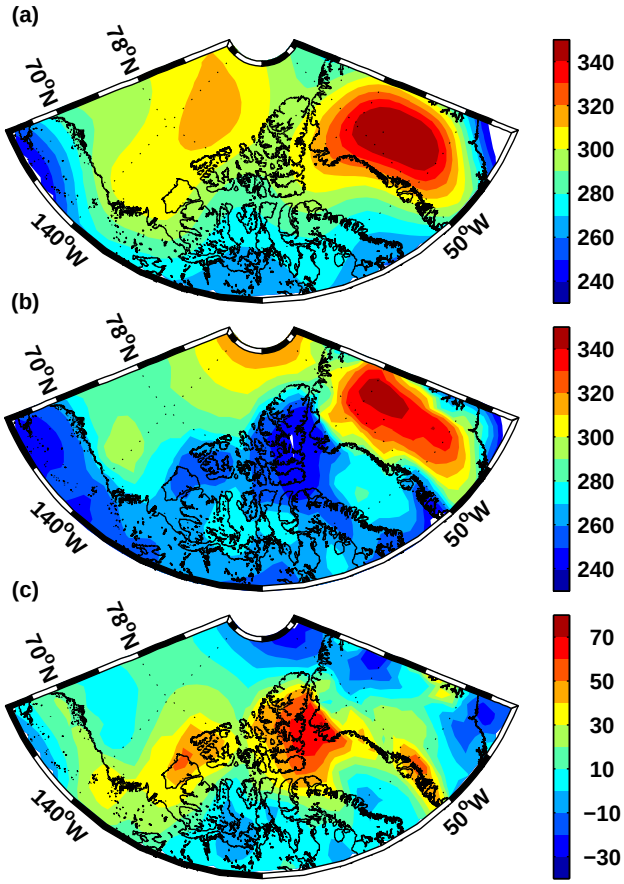

Figure 3.4: Downwelling shortwave radiation [W m^{-2}] in July (a) from the Arctic Global Radiation (AGR) dataset, (b) from Large and Yeager (2004) dataset, and (c) the difference between the AGR dataset and Large and Yeager (2004) dataset for June.

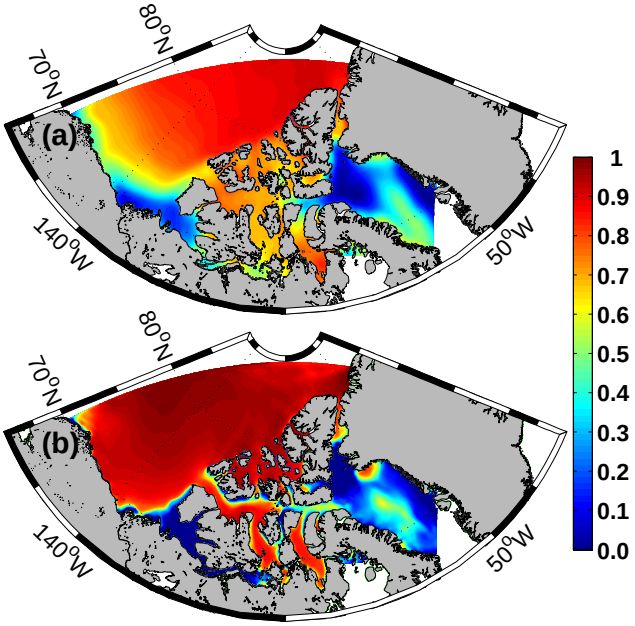

Figure 3.5: (a) Mean sea ice concentration in May for the period 1984-2004 from SSM/I, (b) Simulated mean sea ice concentration in July averaged over years 6-8.

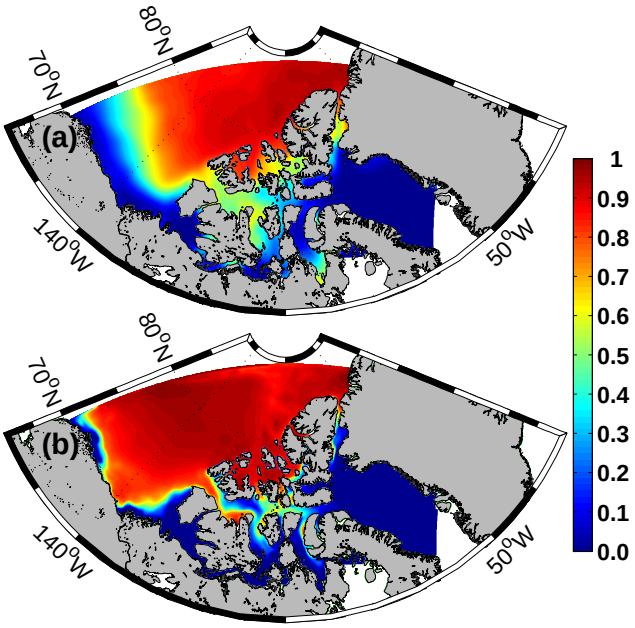

Figure 3.6: (a) Mean sea ice concentration in September for the period 1984-2004 from SSM/I, (b) Simulated mean sea ice concentration in September averaged over years 6-8.

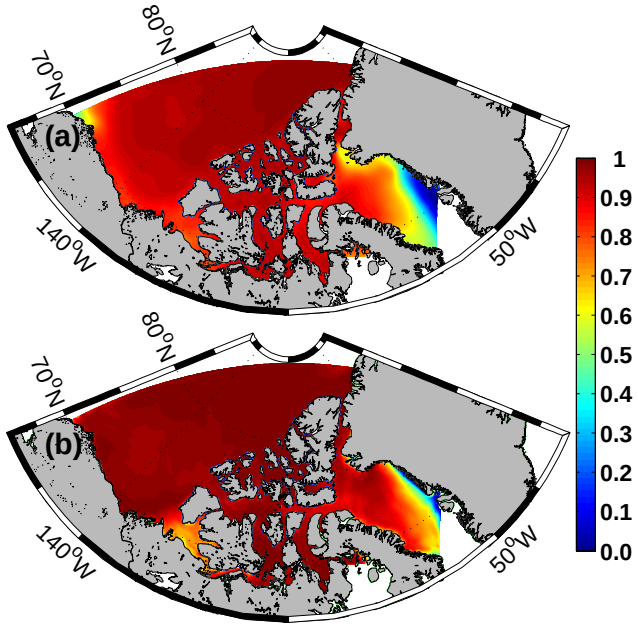

Figure 3.7: (a) Mean sea ice concentration in September for the period 1984-2004 from SSM/I, (b) Simulated mean sea ice concentration in September averaged over years 6-8.

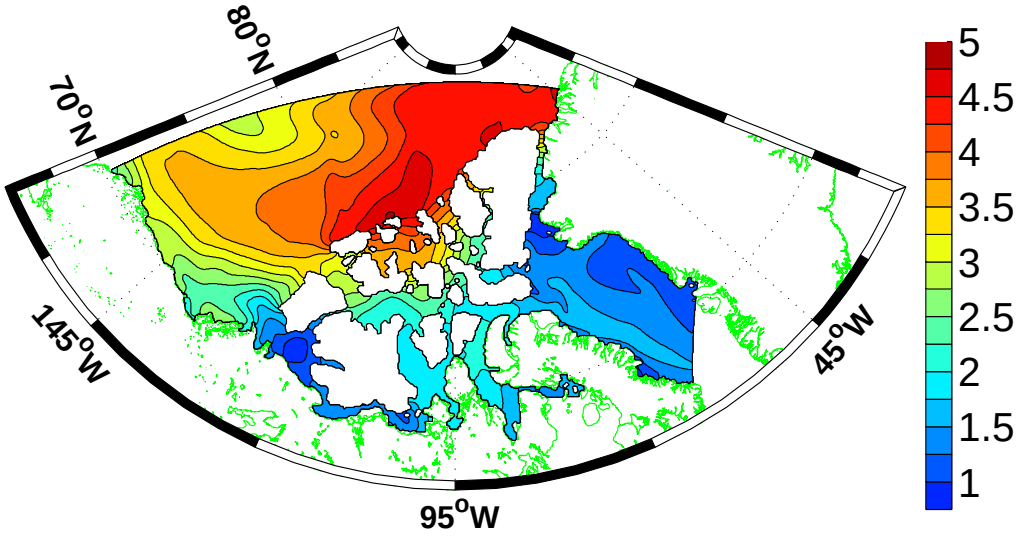

Figure 3.8: Simulated mean sea ice thickness [m] in April averaged over years 6-8.

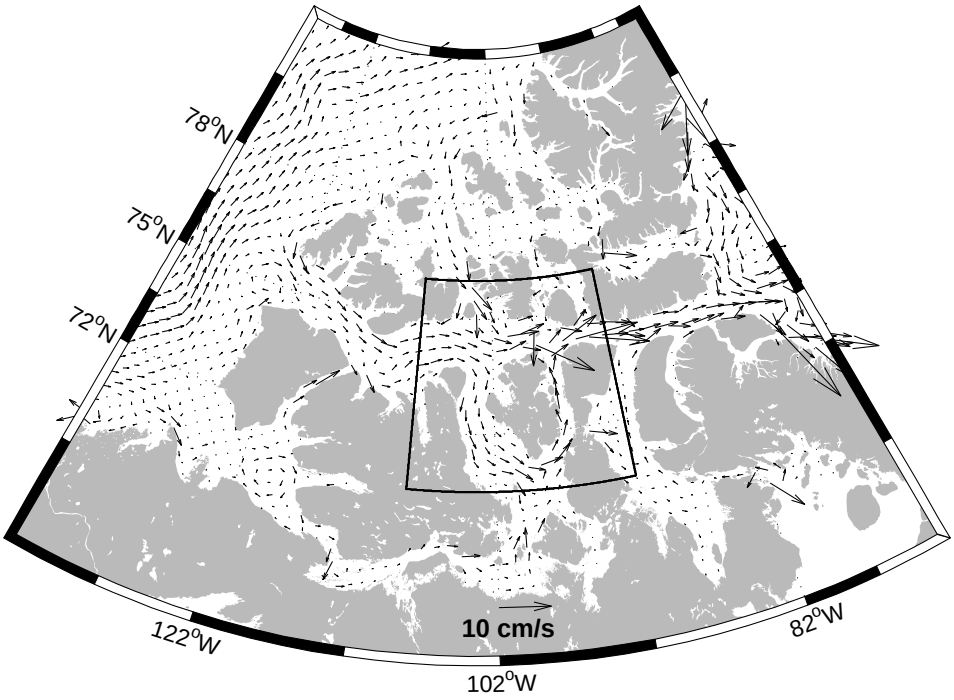

Figure 3.9: (a) The mean currents in the CAA averaged over the top 300 m and over years 6-8 in the CAA control experiment, with one fifth of the horizontal grid points shown. The box shows the zoomed region in Figure 3.10.

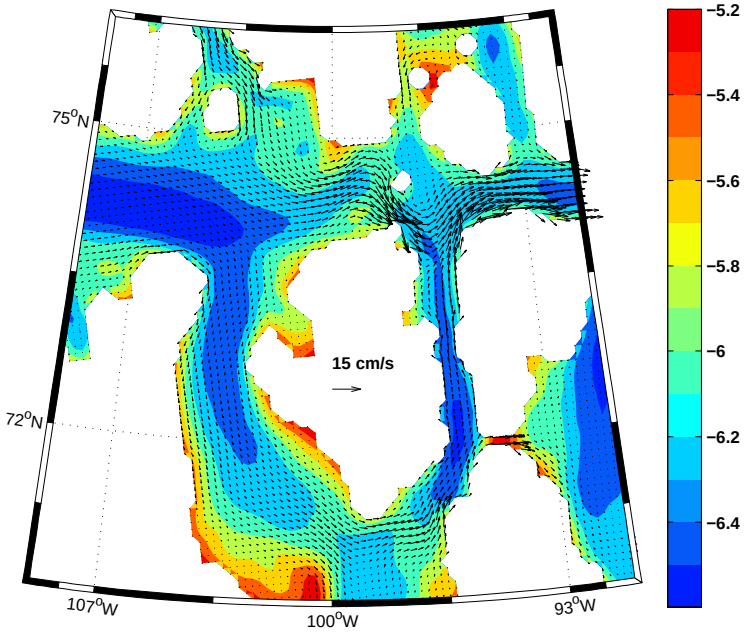

Figure 3.10: Zoom of the currents from Figure 3.9. The background field is $\log_{10}(f/h)$.

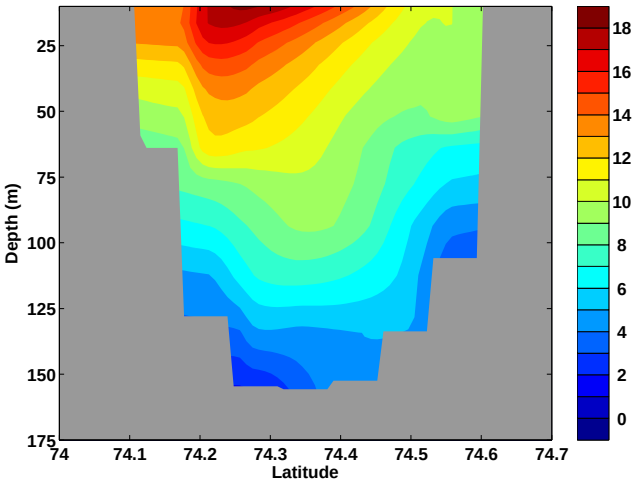

Figure 3.11: The mean cross section current speed [cm s^{-1}] in Barrow Strait (section shown in Figure) in April averaged over years 6-8 in the CAA control experiment.

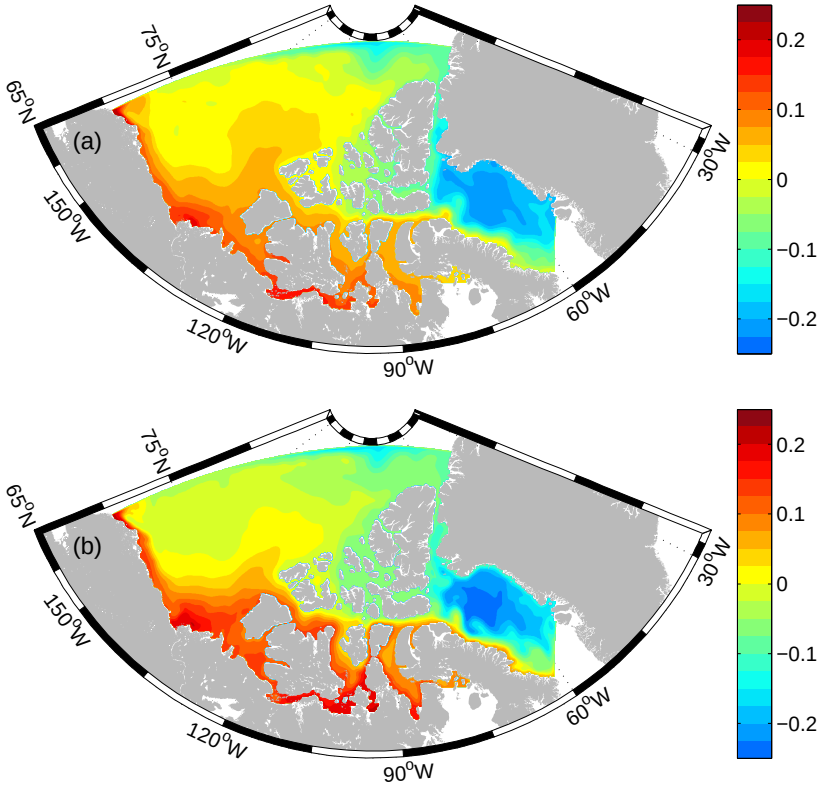

Figure 3.12: Sea level height [m] averaged over years 6-8 in the CAA in (a) March, (b) September in CAA control experiment.

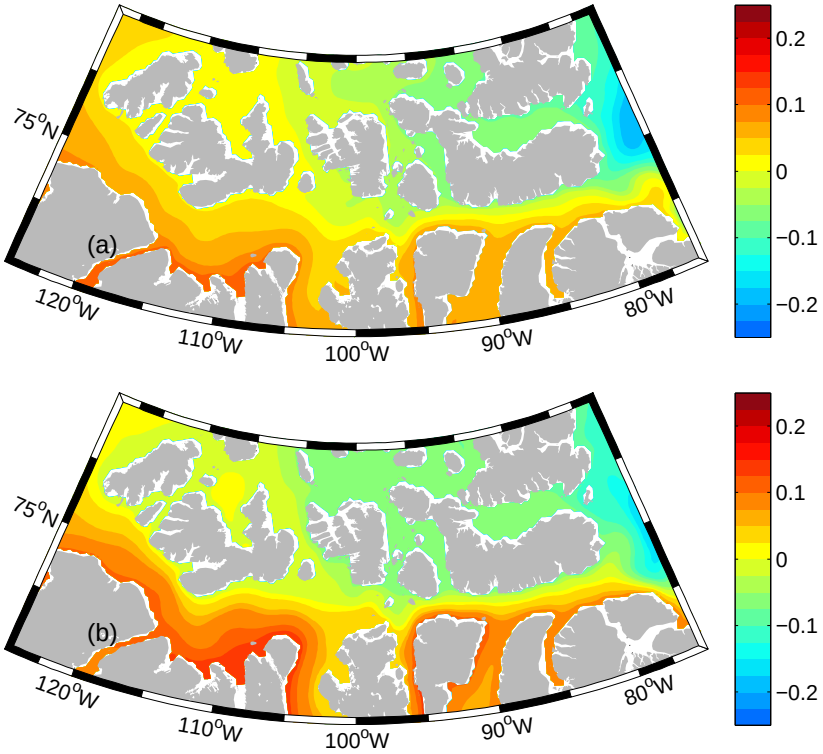

Figure 3.13: Sea level height [m] averaged over years 6-8 in the CAA in (a) March, (b) September in CAA control experiment.

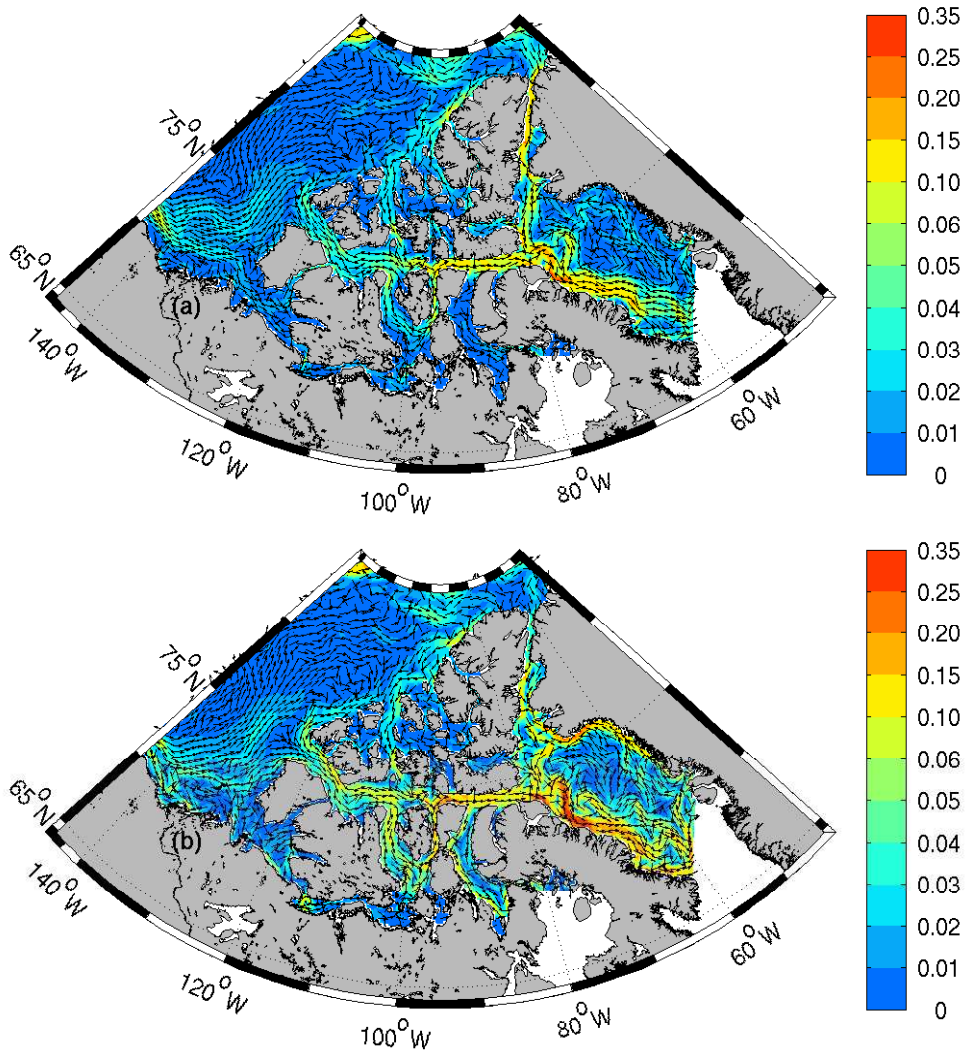

Figure 3.14: Magnitude [cm s^{-1})] of monthly currents over top 50 m (color contoured) averaged over years 6-8 in March (a) and September (b) with velocity vectors superimposed

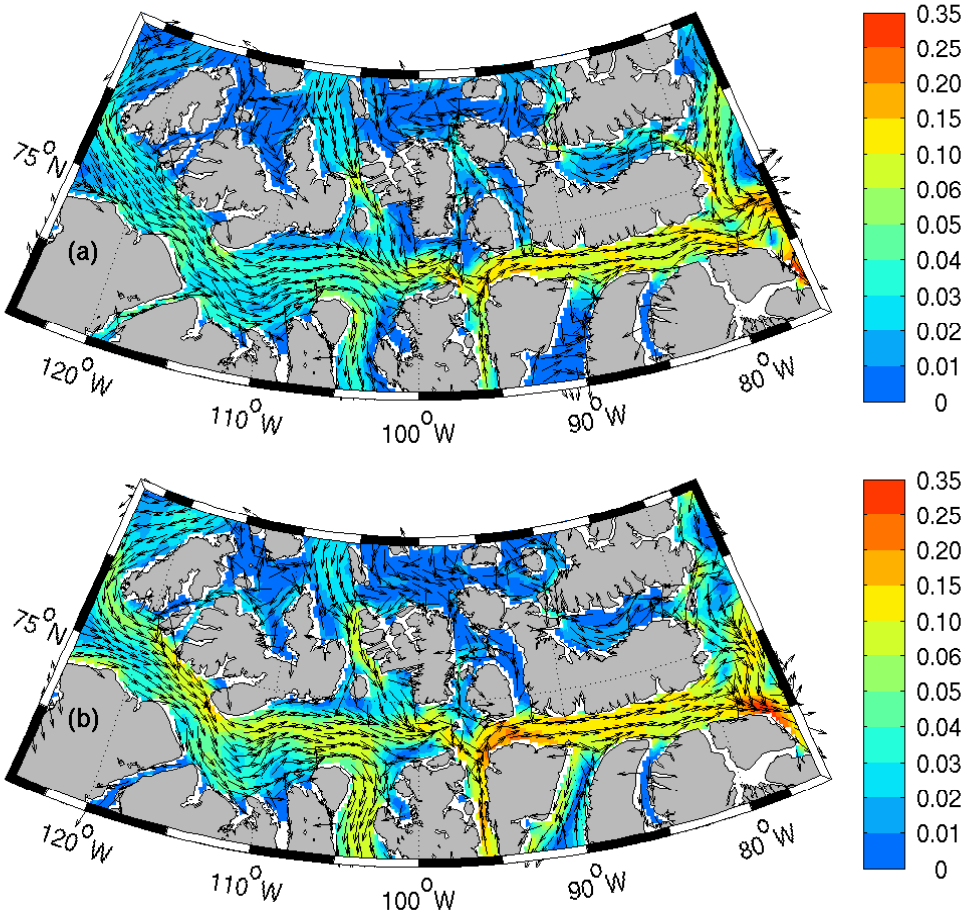

Figure 3.15: Magnitude [cm s^{-1})] of monthly currents over top 50 m (color contoured) averaged over years 6-8 in March (a) and September (b) with velocity vectors superimposed

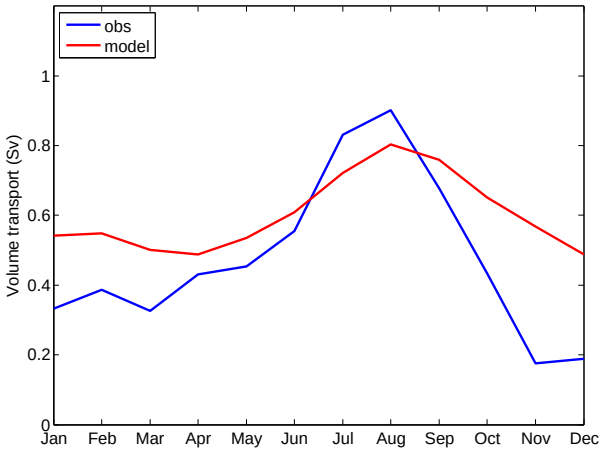

Figure 3.16: Mean annual cycle of observed volume transport [Sv] from August 1998 to July 2010 (blue line) and modeled volume transport [Sv] from August 1998 to August 2004 (red line) through western Lancaster Sound.

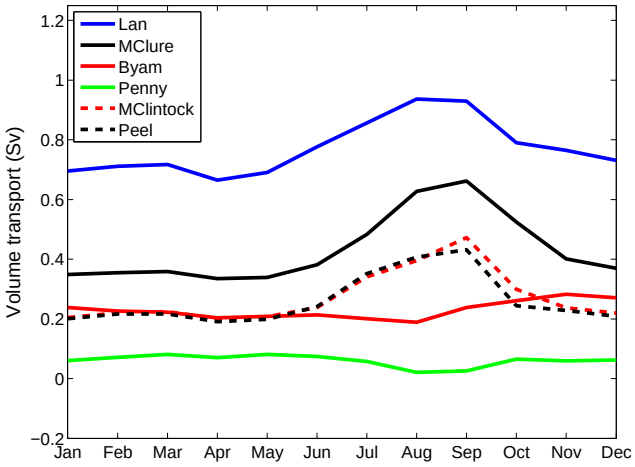

Figure 3.17: Annual cycle of volume transport [Sv] through Lancaster Sound, M'Clure Strait, Byam Martin Channel, Penny Strait, M'Clintock Channel, Peel Sound in CAA control experiment averaged over years 6-8.

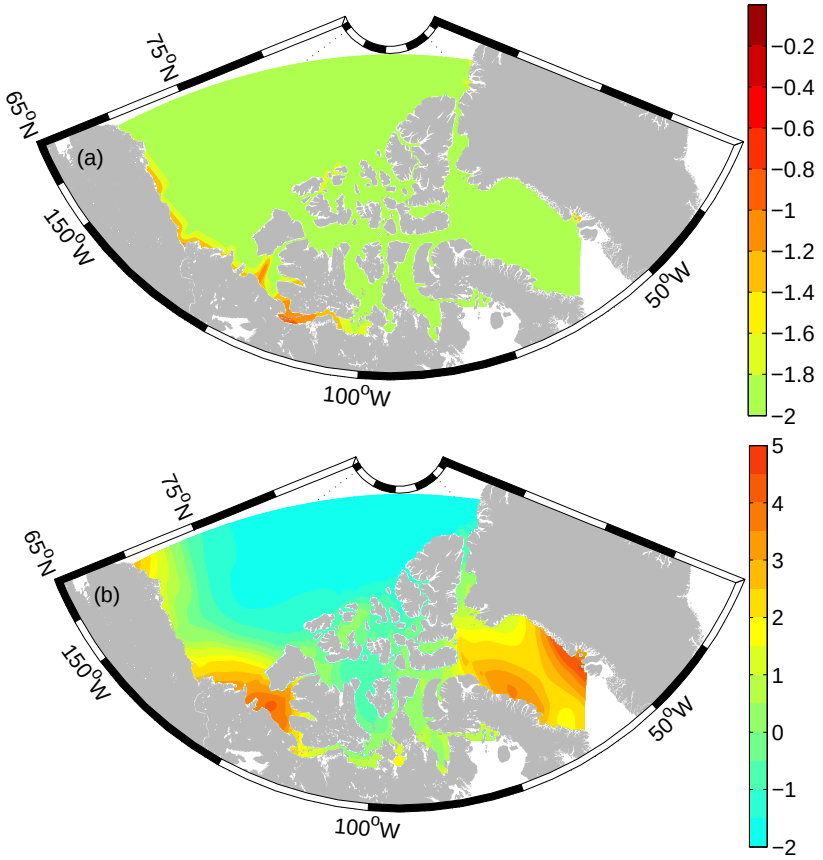

Figure 3.18: Climatology sea surface temperature [^{0}C] from PHC dataset in the CAA (a) March, (b) September.

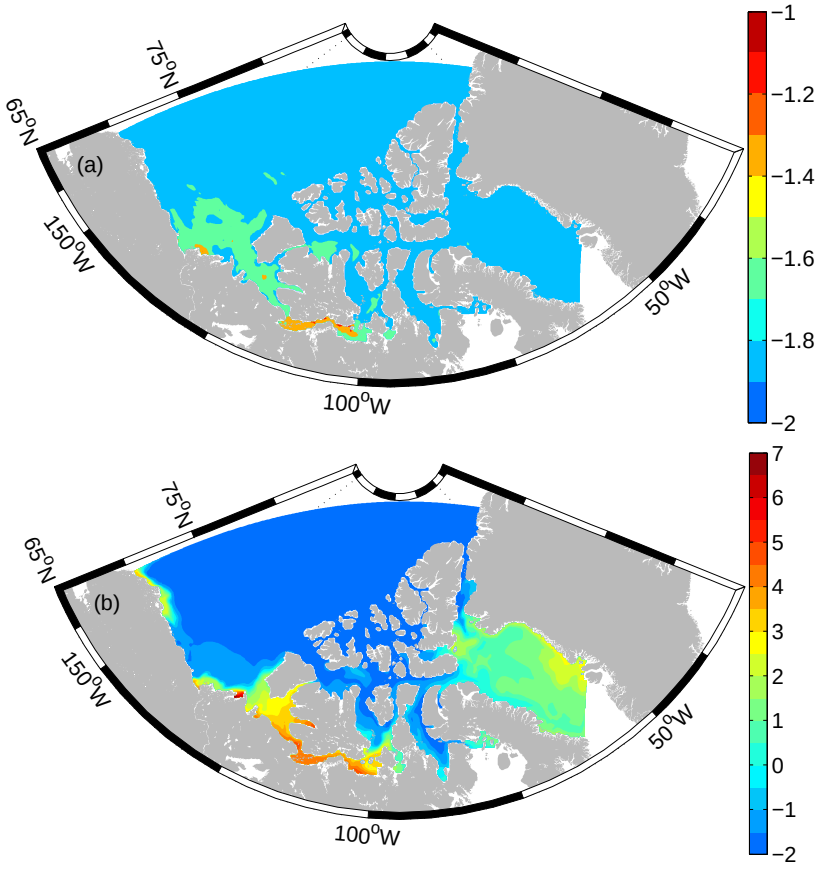

Figure 3.19: Sea surface temperature averaged [^{0}C] over years 6-8 in the CAA in (a) March, (b) September in CAA control experiment.

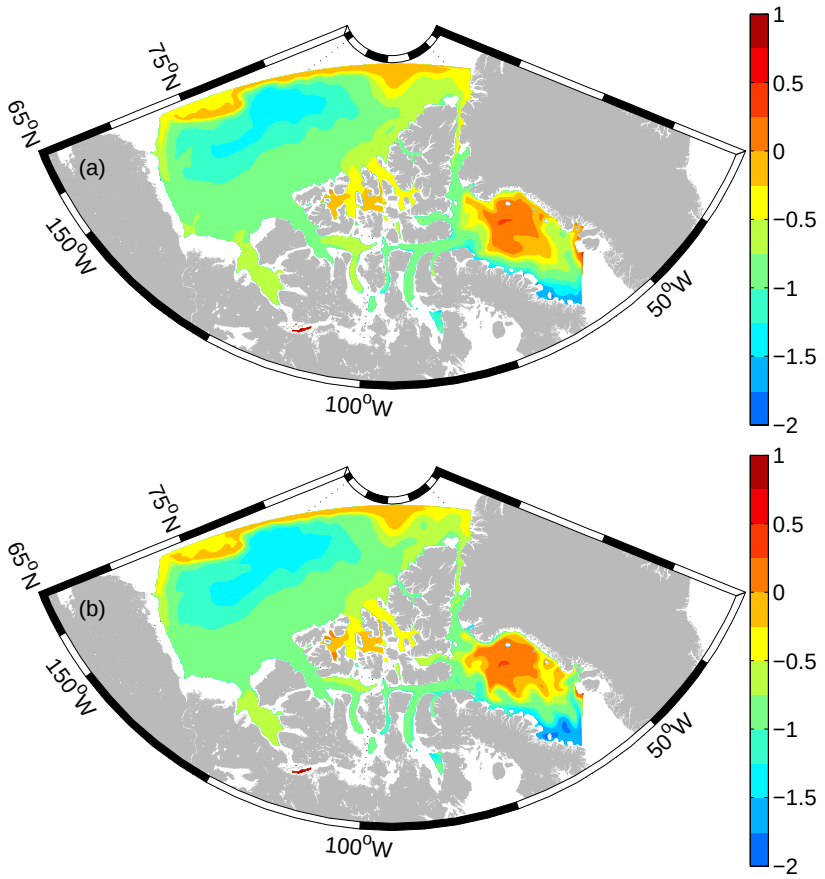

Figure 3.20: Temperature [^{0}C] at 100 m in the CAA averaged over years 6-8 in (a) March, (b) September in CAA control experiment.

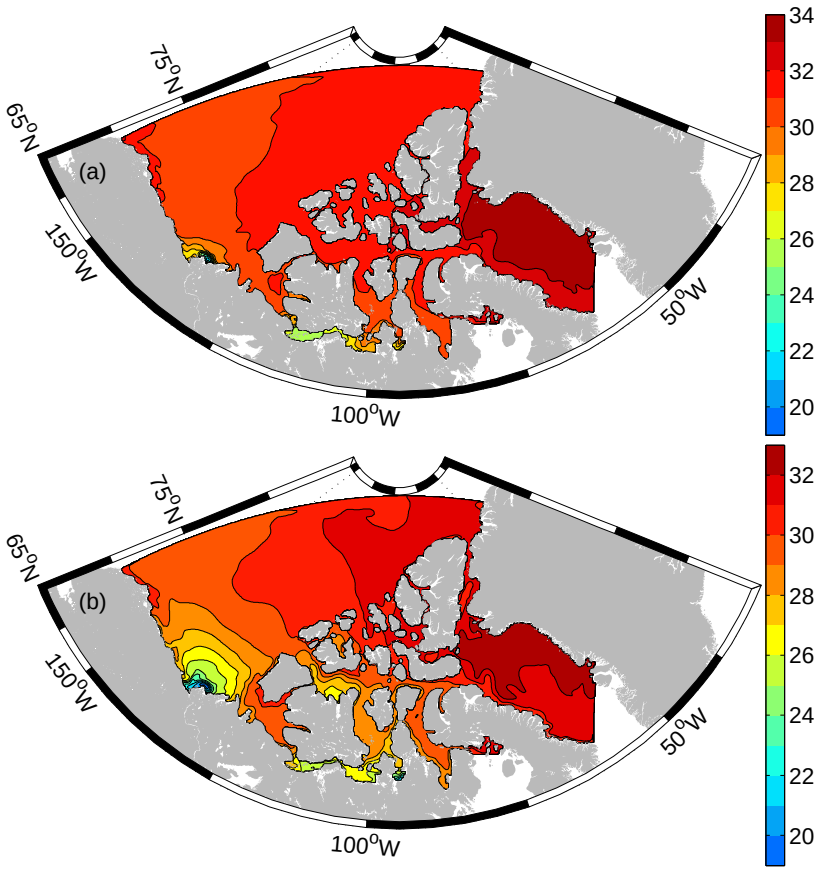

Figure 3.21: Sea surface salinity in the CAA averaged over years 6-8 in (a) March and (b) September in CAA control experiment.

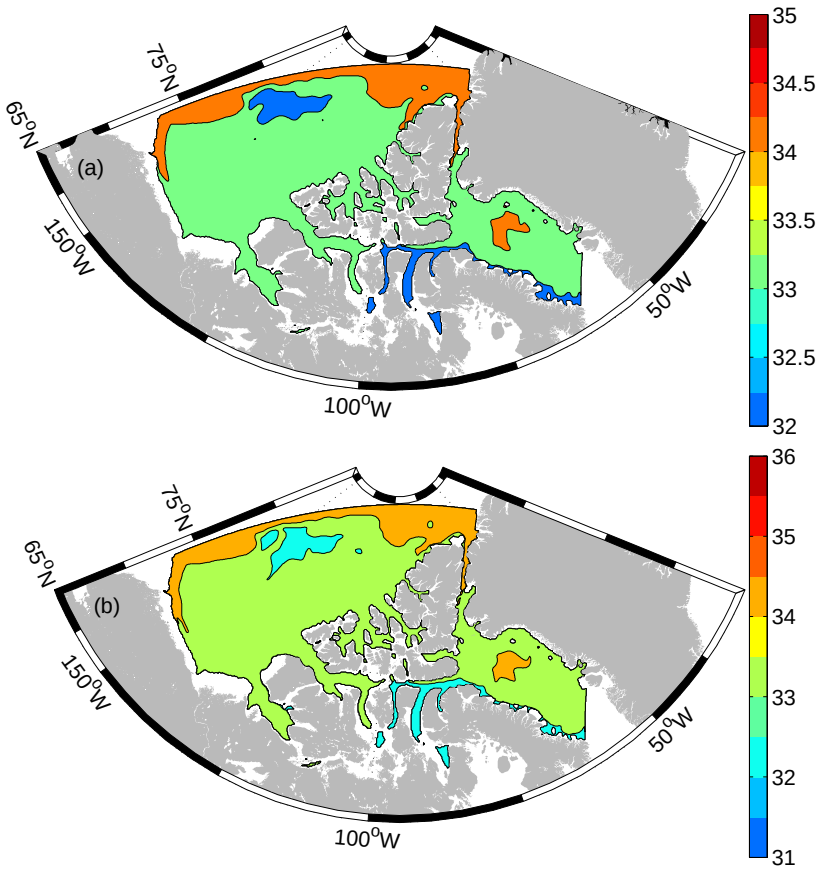

Figure 3.22: Salinity at 100 m in the CAA averaged averaged over years 6-8 (a) March, (b) September in CAA control experiment.

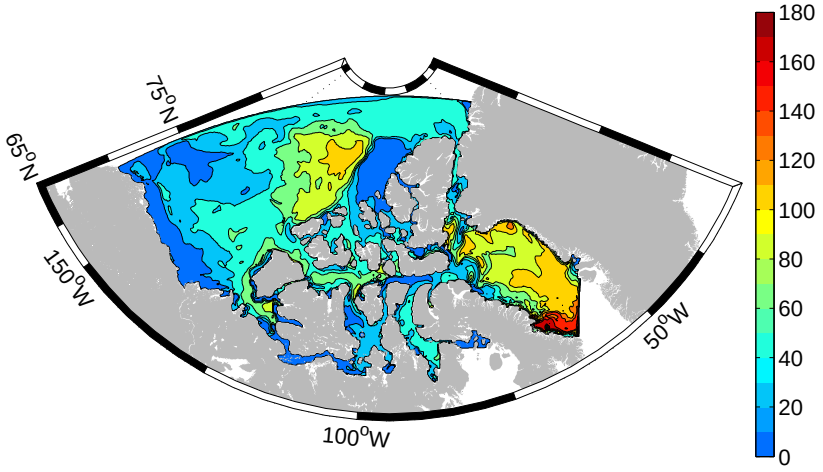

Figure 3.23: Mixed layer depth [m] in the CAA averaged over years 6-8 in April in CAA control experiment.

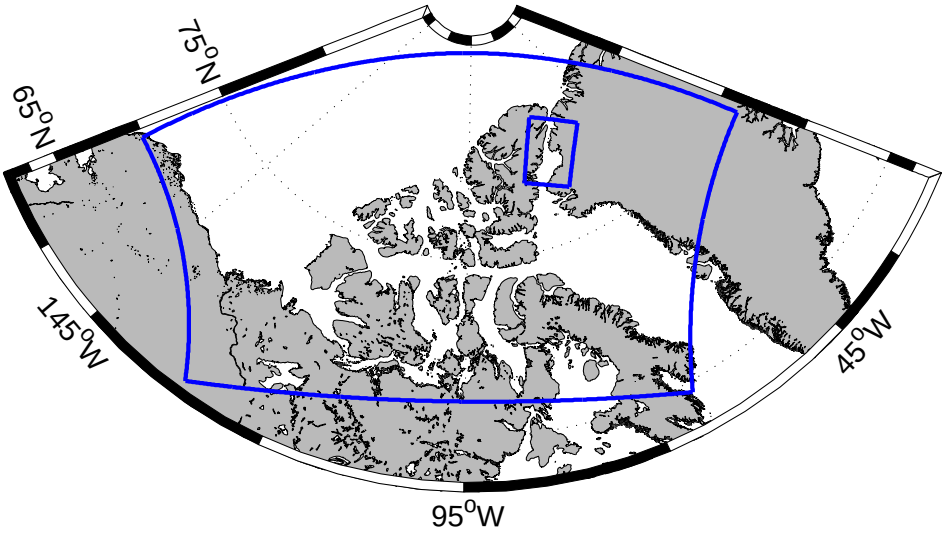

Figure 3.24: The position of ice bridge in Nares Strait (Small blue box). The large blue box shows the model domain.

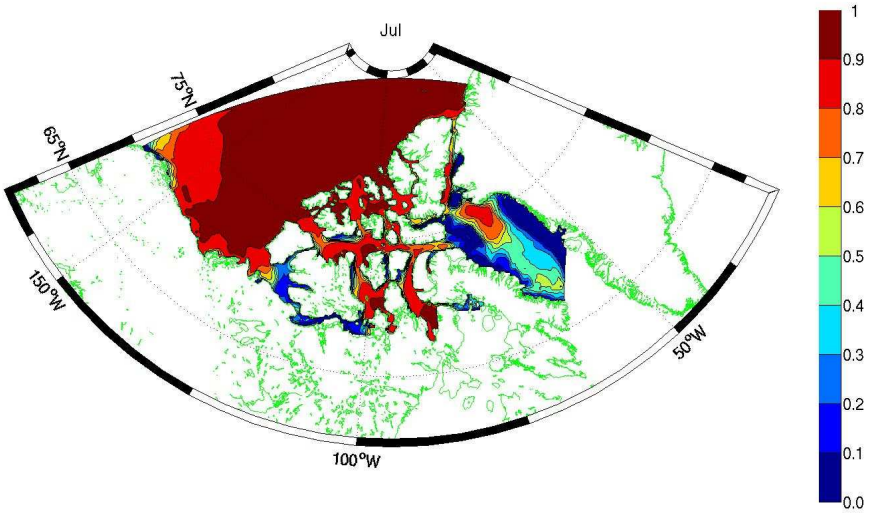

Figure 3.25: Modeled sea ice concentration in July 2000 when there is no sea ice bridge in Nares Strait in CAA interannual experiment.

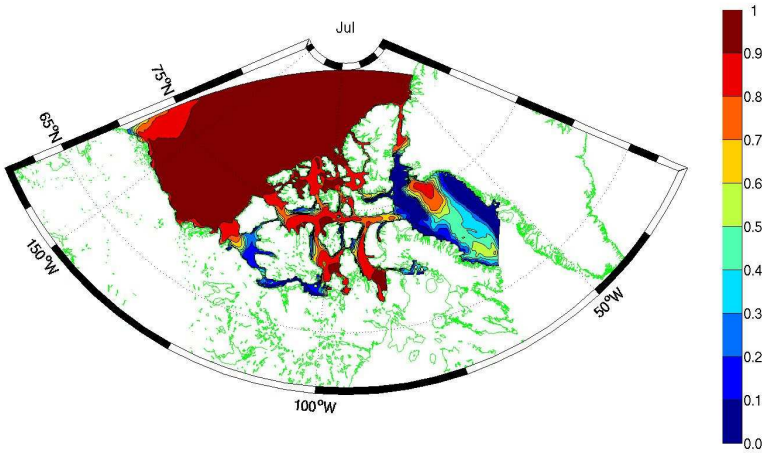

Figure 3.26: Modeled sea ice concentration in July 2000 when the sea ice bridge in Nares Strait is parameterized in CAA interannual experiment.

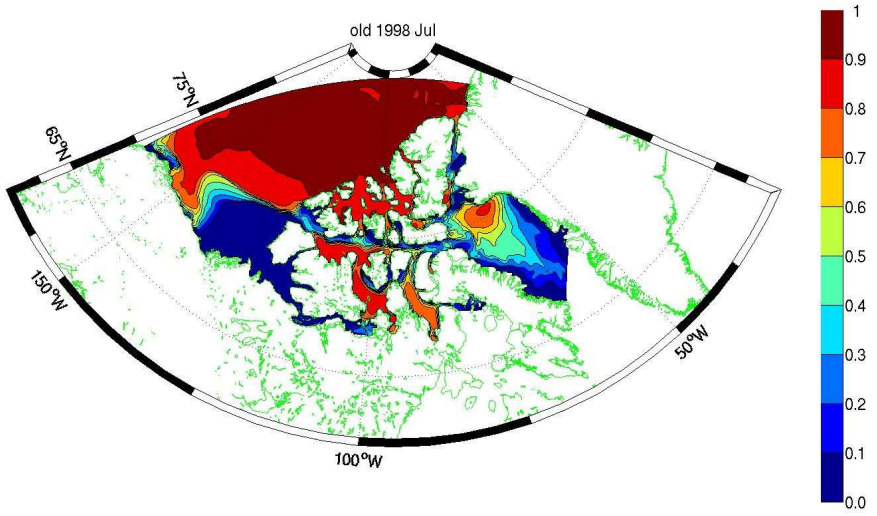

Figure 3.27: Modeled sea ice concentration in July 1998 when downwelling shortwave radiation from the CORE data is used and there is no ice bridge in Nares Strait in CAA interannual experiment.

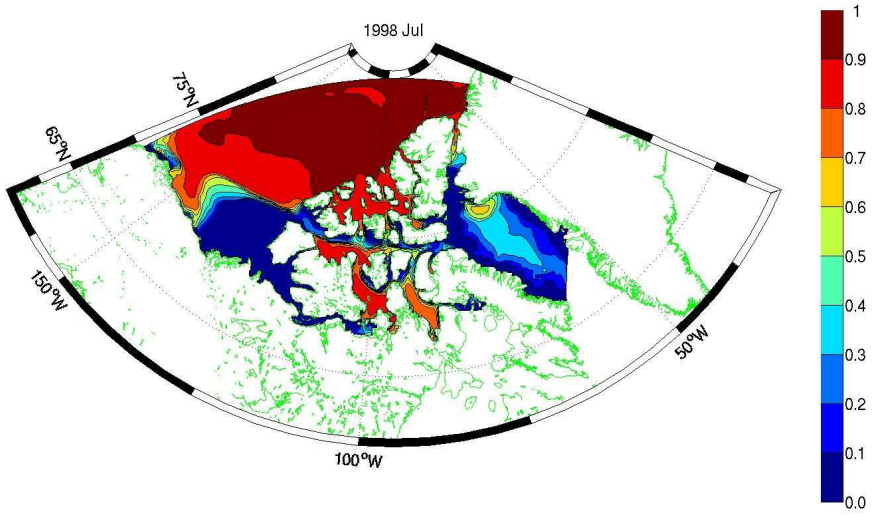

Figure 3.28: Modeled sea ice concentration in July 1998 when downwelling shortwave radiation from AGR data is used and the sea ice bridge in Nares Strait is parameterized in CAA interannual experiment.

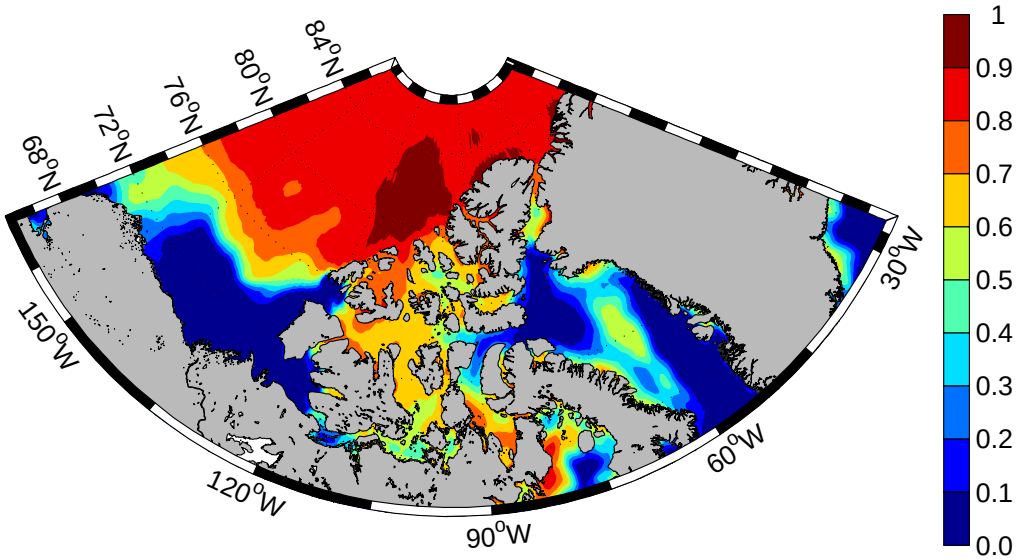

Figure 3.29: Observed sea ice concentration from SSM/I in July 1998.

Bibliography

Agnew, T., A. Lambe, and D. Long, 2008: Estimating sea ice area flux across the Canadian Arctic Archipelago using enhanced AMSR-E. *Journal of Geophysical Research*, **113**, doi:10.1029/2007JC004582.

Barber, D., J. Hanesiak, W. Chan, and J. Piwowar, 2001: Sea-ice and meteorological conditions in Northern Baffin Bay and the North Water polynya between 1979 and 1996. *Atmosphere-Ocean*, **39**, 343–359.

Barber, F., 1965: Current observations in Fury and Helca Strait. *J. Fish. Res. Board Can.*, **22**, 225–229.

Blanke, B., and P. Delecluse, 1993: Variability of the tropical Atlantic Ocean simulated by a general circulation model with two different mixed-layer physics. *Journal of Physical Oceanography*, **23**, 1363–1388.

Bouillon, S., M. A. M. Maqueda, V. Legat, and T. Fichefet, 2009: An elasticviscousplastic sea ice model formulated on Arakawa B and C grids. *Ocean Modelling*, **27**, doi:10.1016/j.ocemod.2009.01.004, 174–184.

Bourke, R. H., and R. P. Garrett, 1987: Sea ice thickness distribution in the Arctic Ocean. *Cold Regions Sciences and Technology*, **13**, 259–280.

Box, J., J. Key, J. Maslanik, and M. Serreze, 1998: Arctic Global Radiation (AGR) data set. National Snow and Ice Data Center, Boulder, digital Media.

Cavalieri, D., C. Parkinson, P. Gloersen, , and H. J. Zwally, 2008: Sea ice concentrations from Nimbus-7 SMMR and DMSP SSM/I passive microwave data. National Snow and Ice Data Center, Boulder, USA, digital Media.

Dumont, D., Y. Gratton, and T. E. Arbetter, 2009: Modeling the Dynamics of the North Water Polynya Ice Bridge. *Journal of Physical Oceanography*, **39**, 1448–1461.

Fichefet, T., and M. M. Maqueda, 1997: Sensitivity of a global sea ice model to the treatment of ice thermodynamics and dynamics. *Journal of Geophysical Research*, **102**, 12609–12646.

Haas, C., S. Hendricks, and M. Doble, 2006: Comparison of the sea-ice thickness distribution in the Lincoln Sea and adjacent Arctic Ocean in 2004 and 2005. *Annals of Glaciology*, **44**, 247–252.

Holloway, G., and Z. Wang, 2009: Representing eddy stress in an Arctic Ocean model. *Journal of Geophysical Research*, **114**, doi:10.1029/2008JC005169.

Hunke, E., and J. Dukowicz, 1997: An Elastic-Viscous-Plastic for sea ice dynamics. *Journal of Physical Oceanography*, **27**, 1849–1867.

Jakobsson, M., R. Macnab, L. Mayer, R. Anderson, M. Edwards, J. Hatzky, H. W. Schenke, and P. Johnson, 2008: An improved bathymetric portrayal of the Arctic Ocean: Implications for ocean modeling and geological, geophysical and oceanographic analyses. *Geophys. Res. Lett.*, **35**, doi:10.1029/2008GL033520.

Kwok, R., 2005: Variability of Nares Strait ice flux. *Geophysical Research Letters*, **32**, doi:10.1029/2005GL024768.

Kwok, R., L. T. Pedersen, P. Gudmandsen, and S. S. Pang, 2010: Large sea

ice outflow into the Nares Strait in 2007. *Geophysical Research Letters*, **37**, doi:10.1029/2009GL041872, 1363–1388.

Large, W., and S. Yeager, 2004: Diurnal to decadal global forcing for ocean and sea-ice models: the data sets and flux climatologies. NCAR, NCAR technical note: NCAR/TN-460+ STR.

Madec, G., 2008: NEMO Ocean Engine. Institut Pierre-Simon Palace (IPSL), France, volume 27 of *Notes de Pole de modelisation*.

Marshunova, M., and N. T. Chernigovskii, 1971: Radiatsionnyi rezhim zarubeznhoi arktiki (radiation regime of the foreign arctic). Gidrometeorologicheskoe Izdatel'stvo, 182.

Marshunova, M., and A. Mishin, 1994: Handbook of the radiation regime of the arctic basin (results from the drift stations). Applied Physics Laboratory, University of Washington, Seattle, WA, Tech. Rep. APL UW TR 9413.

Maykut, G. A., and N. Untersteiner, 1971: Some results from a time-dependent thermodynamic model of sea ice. *Journal of Geophysical Research*, **76**, 1550–1575.

McLaren, A., P. Wadhams, and R. Weintraub, 1984: The sea ice topography of M'Clure Strait in winter and summer of 1960 from submarine profiles. *Arctic*, **37**, 110–120.

Melling, H., 2000: Exchanges of freshwater through the shallow straits of the North American Arctic. *Freshwater Budget of the Arctic Ocean*, E. L. et al., ed., Kluwer Academic Publishers, The Netherlands, NATO Science Series, 479–502.

— 2002: Sea ice of the northern Canadian Arctic Archipelago. *Journal of Geophysical Research*, **107**, doi:10.1029/2001JC001102.

Melling, H., D. A. Riedel, and Z. Gedalof, 2005: Trends in the draft and extent of seasonal pack ice, Canadian Beaufort Sea. *Geophysical Research Letters*, **32**, doi:10.1029/2005GL024483.

Murray, R. J., 1996: Explicit generation of orthogonal grids for ocean models. *Journal of Computational Physics*, **126**, doi:10.1006/jcph.1996.0136, 251–273.

Prinsenberg, S. J., and E. Bennett, 1987: Mixing and transports in Barrow Strait, the central part of the Northwest passage. *Continental Shelf Research*, **7**, doi:10.1016/0278-4343(87)90006-9, 913–935.

— 1989: Transport between Peel Sound and Barrow Strait in the Canadian Arctic. *Continental Shelf Research*, **9**, doi:10.1016/0278-4343(89)90008-3, 427–444.

Prinsenberg, S. J., and J. Hamilton, 2005: Monitoring the Volume, Freshwater and Heat Fluxes Passing through Lancaster Sound in the Canadian Arctic Archipelago. *Atmosphere-Ocean*, **43**, doi:10.3137/ao.430101, 1–22.

Prinsenberg, S. J., J. Hamilton, I. Peterson, and R. Pettipas, 2009: Observing and interpreting the seasonal variability of the oceanographic fluxes passing through Lancaster Sound of the Canadian Arctic Archipelago. *Influence of Climate Change on the Changing Arctic and Sub-Arctic Conditions*, J. C. Nihoul and A. G. Kostianoy, eds., Springer, The Netherlands, NATO Science for Peace and Security Series, 125–143.

Rigor, I. G., R. Colony, and S. Martin, 2000: Variations in surface air temperature in the Arctic from 1979-1997. *Journal of Climate*, **13**, 896–914.

Roulet, R. R., 1969: Radiation regime of arctic drifting station arlis ii, jan-

uary 1964-may 1965. Department of Atmospheric Sciences, University of Washington, NR 307-252, 58.

Sadler, H., 1982: Water flow into Foxe Basin through Fury and Hecla Strait. *Naturaliste Can.*, **109**, 701–707.

Serreze, M. C., J. R. Key, J. E. Box, J. A. Maslanik, and K. Steffen, 1998: A new monthly climatology of global radiation for the Arctic and comparisons with NCEP-NCAR reanalysis and ISCCP-C2 fields. *Journal of Climate*, **11**, 121–136.

Shine, K. P., and A. Henderson-Sellers, 1985: Development of a turbulence closure model for geophysical fluid problems. *Journal of Geophysical Research*, **90**, 2243–2250.

Sou, T., and G. Flato, 2009: Sea ice in the Canadian Arctic Archipelago: Modeling the past (1950–2004) and the future (2041–60). *Journal of Climate*, **22**, doi:10.1175/2008JCLI2335.1, 2181–2198.

Steele, M., R. Morley, and W. Ermold, 2001: PHC: A global ocean hydrography with a high-quality Arctic Ocean. *Journal of Climate*, **14**, 2079–2087.

Tang, C. C., C. K. Ross, T. Yao, B. Petrie, B. M. DeTracey, and E. Dunlap, 2004: The circulation, water masses and sea-ice of Baffin Bay. *Progress in Oceanography*, **63**, doi:10.1016/j.pocean.2004.09.005, 183–228.

Treguier, A. M., B. Barnier, A. P. de Miranda, J. M. Molines, N. Grima, M. Imbard, G. Madec, C. Messager, T. Reynaud, and S. Michel, 2001: An eddy permitting model of the Atlantic circulation: Evaluating open boundary conditions. *Journal of Geophysical Research*, **106**, 22115–22129.

Weller, G., and B. Holmgren, 1974: Summer global radiation and albedo-data for three stations in the arctic basin, ice island t-3, barrow, prudhoe bay,

1971-1973. Geophysical Institute, University of Alaska, Fairbank, Tech. Rep. No. 2, December 1974, 31.

Zhang, J., and D. A. Rothrock, 2003: Modeling global sea ice with a thickness and enthalpy distribution model in generalized curvilinear coordinates. *Mon. Wea. Rev.*, **131**, 845–861.

Chapter 4

Flow constraints on pathways through the Canadian Arctic Archipelago

4.1 Introduction

The Canadian Arctic Archipelago (CAA) is a complex network of straits and basins connecting the Arctic Ocean and the Atlantic Ocean (Figure 4.1). Parry Channel, which runs from McClure Strait, Viscount Melville Sound, Barrow Strait to Lancaster Sound with a 131 m sill in Barrow Strait, is one of three major passages for the water flow from Arctic Ocean to Baffin Bay. The other two passages are through Nares Strait, and Jones Sound.

The CAA is one of the main pathways for freshwater outflow from the Arctic Ocean to the Atlantic Ocean (Dickson et al., 2007). This freshwater may impact the sub-polar gyre of the North Atlantic on issues from deep water formation (Aagaard and Carmack, 1989, 1994) to nutrient supply and productivity (Carmack, 2007). The importance of the freshwater outflow from the CAA might become more important in future climate scenarios (Dickson et al., 2007). The waters of the CAA are also very important locally, as a biological habitat (Stephenson and Hartwig, 2010), hunting grounds for the local Inuit peoples (Wenzel, 1978) as well as a possible transportation corridor

(Pharand, 1984).

Flow through the central archipelago is directed from the Beaufort Sea to Baffin Bay. The zero-th order driving mechanism is the sea level difference (Stigerbrandt, 1984; Kliem and Greenberg, 2003) with temporal anomalies strongly correlated with the wind stress over the Beaufort Sea (Prinsenberg et al., 2009). Extended current meter measurements have been made in Barrow Strait (Figure 1) over the past decade (Prinsenberg and Hamilton, 2005) and provide the single long term record of currents and transports in the region (Melling et al., 2008). Otherwise, only limited short term current records exist (Melling et al., 1984). General ideas related to the sea ice, such as the southward flowing ice stream in M'Clintock Channel (Figure 1), extend back to the 1850s and the search for Franklin's expedition. But detailed sea ice concentration maps extend only back to the 1960s (Canadian Ice Service, 2007) and detailed studies of ice motion are few (Agnew et al., 2008).

The surface layer (above 200 m) in the Beaufort Sea is fresher and lighter than that in Baffin Bay (Rudels, 1986) and the difference in steric height from the Beaufort Sea to Baffin Bay, with respect to the 250 decibar level, was calculated by Muench (1971) to be 0.3 m. This difference creates pressure gradients and drives the flow through the CAA (Rudels, 1986). In McClure Strait, the flow is southeastward (Melling et al., 1984).

There is southward flow towards Parry Channel via Byam Martin Channel and Penny Strait, with speeds of 5 to 13 cm s^{-1} based on current meter measurement (Fissel et al., 1988). In M'Clintock Channel, available current meter measurements shows the current is southward (Barry, 1993).

Based on hydrographic data and month-long sets of current meter data, part of the eastward transport through Barrow Strait flows southward into northern Peel Sound before continuing eastward through Barrow Strait at the north entrance of Peel Sound (Prinsenberg and Bennett, 1989). In April

1981, the northward transport (0.17 Sv) in eastern Peel Sound is higher than the southward transport (0.02 Sv) in western Peel Sound and is a significant contributor to Barrow Strait transport (Prinsenberg and Bennett, 1989).

There is a strong eastward current (10-20 cm s^{-1}) on the south side of western Lancaster Sound and the flow is similar at all depths and thus barotropic in nature while the current is weak on the north side of the sound and the flow is variable with depth and baroclinic in nature (Prinsenberg and Hamilton, 2005). Based on a section through western Lancaster Sound coincident with the moorings of Prinsenberg and Hamilton (2005), the yearly mean volume transport at the section, over 1998 to 2006, based on mooring data, is 0.7 $\pm$ 0.3 Sv (Prinsenberg et al., 2009). There is a strong annual cycle of volume transport through western Lancaster Sound, ranging between weak transport in December (0.2 Sv) and strong transport in summer (1.1 Sv) (Melling et al., 2008). The 6-year mean freshwater flux through western Lancaster Sound is 48 mSv (Melling et al., 2008). McClure Strait/Viscount Melville Sound, Byam Martin Channel, Penny Strait, and Peel Sound are all sources of the transport through western Lancaster Sound.

In the eastern Lancaster Sound, the Baffin Current penetrates westward along the north side of eastern Lancaster Sound, crosses to the south side and flows out to the east based on satellite-tracked drifter measurements, hydrographic data, and current meter data from the summer of 1978 and 1979 (Fissel et al., 1982). In the core of the intrusive current on the north side of eastern Lancaster Sound, the near-surface speed was 75 cm s^{-1}, decreasing to 50 cm s^{-1} at 40 m depth and 25 cm s^{-1} at 250m depth (Fissel et al., 1982). Since the flow is eastward throughout Barrow Strait between Cornwallis Island and Somerset Island (Prinsenberg and Bennett, 1987), the Baffin Current does not extend as far as Resolute Bay, which is located to the south of Cornwallis Island. Jones and Coote (1980) analyzed water masses and nutrient distri-

bution in Parry Channel and Baffin Bay and also suggested that the Baffin Water could not intrude into the region near Resolute Bay.

Inferred from CTD data, there is westward flow on the north side of Viscount Melville Sound, Barrow Strait, and Lancaster Sound (de Lange Boom et al., 1987). However, as far as we know, there is no data from direct current meters morred on the north side of Viscount Melville Sound. Holloway and Wang (2009) successfully simulated in a global ice-ocean coupled model a westward current on the north side of Parry Channel. They explained this by the neptune effect, which is a forcing of mean flows by eddy-topography interaction.

Numerical modeling of the CAA in the past has been very limited and the flow dynamics within the CAA are poorly understood. Kliem and Greenberg (2003) used a diagnostic model to study the summer mean circulation in the CAA. Their model results reveal that the currents in the CAA depend on the elevation difference between the Arctic Ocean and Baffin Bay and on the baroclinic pressure gradients. Sou and Flato (2009) used a high resolution ice-ocean regional model to examine how sea ice conditions in the archipelago region respond to climate projections. The neptune effect is also parameterized in their model. Aksenov et al. (2010) studied the sources of freshwater in the CAA and the routes of different water masses and their transport passing through the CAA.

There are still many open questions related to the circulation in the central CAA. Why is there southward ice motion in M'Clintock Channel? Especially since in August, the wind is directed to the north out of M'Clintock Channel. Why can the Baffin Current not intrude into the region near Resolute Bay? Since the Arctic is rapidly evolving (Serreze et al., 2007), understanding the dynamics that explain these observed features is important if we wish to know how these processes may change in the future.

We will use a pair of numerical configurations of the CAA and the Arctic to examine these questions, focusing on the ocean dynamics of the central archipelago. In section 2, we will discuss the configurations. After showing that the model results reproduce the main features of the observations in section 3, we will provide answers to the questions we posed above in section 4 and 5. Finally we will summarize and examine the significance of our results.

4.2 Model Configurations

Two configurations of the version 3.1 of the Nucleus for European Modeling of the Ocean (NEMO) Ocean/Sea-Ice general circulation model numerical code (Madec, 2008) are used including the Louvain-la-Neuve sea-ice model (LIM2) (Fichefet and Maqueda, 1997) in which ice dynamics are updated with an elastic-viscous-plastic (EVP) rheology (Hunke and Dukowicz, 1997) implemented on a C-grid (Bouillon et al., 2009). We mainly focus on an experiment using a limited domain configuration of the CAA. We also present results from one experiment using a Pan-Arctic configuration, to help explain aspects of the cyclonic flow in eastern Lancaster Sound that are not as well represented in the CAA configuration.

Both configurations have 46 levels in the vertical, with thicknesses from 6 m at the surface to 250 m at the bottom. A partial step representation of bathymetry is used. The two configurations use linear free surface formulation, laplacian horizontal viscosity, nonlinear bottom boundary friction, and a turbulence closure scheme (order 1.5) for vertical mixing (Blanke and Delecluse, 1993).

The two configurations were spun up from September 1, using initial climatological temperature and salinity based on the PHC 3.0 data set (Steele et al., 2001) and run under climatological forcing (normal year forcing). The coupled sea ice-ocean model is forced with 6-hourly surface air temperature,

specific humidity and 10 m winds, daily radiative fluxes, monthly precipitation and snow from Large and Yeager (2004) (hereafter LY04). Normal year forcing data is used in the two configurations. Turbulent fluxes at the sea surface are implemented according to the CORE (Coordinated Ocean Reference Experiments) strategy, utilizing the bulk forcing methodology for global ocean ice models developed by Large and Yeager (2004). Surface albedo is parameterized following Shine and Henderson-Sellers (1985). At the ocean boundaries we need data for temperature, salinity and the velocities. A detailed description of the numerics of the open boundaries is found in Treguier et al. (2001).

The CAA model domain is shown in Figure 4.2a. A tri-polar grid (Murray, 1996) is used in the horizontal, with one pole situated in the Pacific Ocean near Alaska and one pole situated in the northern Atlantic Ocean near Greenland. There are 446×268 points in the horizontal and the model resolution varies between 6.5 km and 9.5 km, with 7.5 km in Lancaster Sound. The bathymetry in CAA model is obtained from International Bathymetric Chart of the Arctic Ocean (IBCAO) (Jakobsson et al., 2008). The water depth in Bellot Strait, which is located between Somerset Island and Boothia Peninsula, is set to 17 m according to Melling (2000) (Figure 4.3a). The bathymetry is smoothed with a Shapiro filter. There is a relaxation to the PHC climatology for sea surface salinity. The coefficient (0.167 m day^{-1}) amounts to a decay time of 60 days for 10 m of water depth; under the ice cover restoring is 5 times stronger. No restoring to the sea surface temperature is applied. Some parameters of the coupled ice-ocean model are given in Table 1.

There are two boundaries. To the east, the boundary is located in Baffin Bay. To the north, the model is connected to the Arctic Ocean and Chukchi Sea. The monthly temperature, salinity, and the ocean velocities at the boundary are provided from a global model with a 1° horizontal resolution (Holloway and Wang, 2009) and were averaged over years 1958-2004. In northern Foxe

Basin, a closed boundary is used. According to observations, the volume transport through the Fury and Hecla Strait is between 0.04 Sv (Sadler, 1982) and 0.1 Sv (Barber, 1965).

The monthly sea ice boundary data (ice velocities, ice concentration and ice thickness) is derived from Pan-Arctic Ice-Ocean Modeling and Assimilation System (PIOMAS) data sets (Zhang and Rothrock, 2003). The monthly data is averaged over 1978-2004. The initial ice concentration is the mean ice concentration on September 1 from 1984 to 2004 derived from SMM/I data sets (Cavalieri et al., 2008). The initial ice thickness is 2 m. In Nares Strait, the ice velocity is set to zero from early February to mid July according to Kwok et al. (2010) in order to simulate the ice bridging in Nares Strait. Tides are not considered in the model. Since tides might have important impact on polynyas in the CAA (Hannah et al., 2009), tidal forcing will be considered in a future version of the CAA configuration. The CAA control experiment ran for 8 years. Unless specified otherwise, mean quantities for the CAA configuration in this paper will refer to averages over years 6-8.

Because the mountainous topography in the northern Archipelago is not resolved by the NCEP/NCAR (National Centers for Environmental Prediction/National Center for Atmospheric Research) model, surface air temperatures over Nares Strait and much of the Archipelago in the NCEP/NCAR reanalysis are too cold in summer and represent high-altitude glaciers of Greenland and Ellesmere Island (Sou and Flato, 2009). The LY04 surface air temperature is based on NCEP/NCAR reanalysis (Large and Yeager, 2004). Although the NCEP/NCAR surface air temperatures are corrected monthly by the mean monthly climatological difference between the IABP/POLES (International Arctic Buoy Program/Polar exchange at the Sea Surface) dataset (Rigor et al., 2000) and NCEP/NCAR reanalysis over the Arctic cap north of 70°N (Large and Yeager, 2004), the revision did not consider the spa-

tial variability of surface air temperature. Thus, for the CAA configuration, the LY04 surface air temperatures are adjusted again using IABP/POLES data, the same approach as used by Sou and Flato (2009). Our adjustment simply removes the monthly climatological difference between the LY04 and IABP/POLES dataset in the normal year forcing. There are still large difference around Nares Strait, with the difference larger than 2.5°C in August and September.

Downwelling shortwave radiation (DSR) is a major term in the surface heat budget and is an important factor that controls the sea ice melting and growth (Maykut and Untersteiner, 1971). The LY04 DSR is based on the ISCCP (International Satellite Cloud Climatology Project) dataset which was created using a GCM (General Circulation Model) radiative transfer model (Large and Yeager, 2004). DSR from LY04 with DSR from the Arctic Global Radiation (AGR) dataset (Box et al., 1998) are compared. In AGR, the DSR is obtained from land stations, ocean drifting stations and empirically derived long-term climatological estimates from earlier Russian studies (Serreze et al., 1998). The ocean drifting stations include Soviet North Pole drifting ice stations (Marshunova and Mishin, 1994) and U.S. drifting stations (ice island "T-3 ", "Arils II ") (Marshunova and Chernigovskii, 1971; Weller and Holmgren, 1974; Roulet, 1969).

Both the DSR from the AGR dataset (Figure 4.4a) and LY04 (Figure 4.4b) show that, in June, the DSR is high over the Greenland ice sheet and is relatively low over the central and southern archipelago, for example. The DSR is high over the Greenland ice sheet because of the elevation effect on atmospheric path length and the tendency for the high central portions of the ice sheet to be above the bulk of the cloud cover (Serreze et al., 1998). In summer, the DSR decreases away from the North Pole when the latitude is less than 70°N because of the combined effects of day length and solar zenith

angle (Serreze et al., 1998). The DSR difference between the AGR data and LY04 (Figure 4.4c), which is above 60 W m^{-2}, in June is highest in northern Baffin Bay. The DSR difference between AGR data and LY04 in northern Baffin Bay is also above 60 W m^{-2} in May, and still $\sim$ 30 W m^{-2} in July and August. An interpolation was used to map the irregularly spaced data to data on the regular grid of the AGR data (Serreze et al., 1998), which may lead to errors. However, since there are several observational sites around northern Baffin Bay (Serreze et al., 1998), it is likely that LY04's underestimation of the DSR around northern Baffin Bay is real. This leads to too small heat fluxes and too much sea ice in summer. Since the AGR dataset covers our the CAA configuration's domain, we use this data for our shortwave radiation. The monthly mean AGR data value is used as the forcing for every day in a given month.

In order to study the effect of bathymetry and sea surface salinity restoring on the circulation in the CAA, four sensitivity experiments (CAA-NS, CAA-MC, CAA-FB, CAA-BS) are conducted (Table 2). The experiment CAA-NS is same as the CAA control experiment except sea surface salinity restoring is removed. We then continue onwards with sea surface salinity restoring removed in all further sensitivity experiments. In CAA-MC, the water depth between 70-73.7°N and 105-100°W is set to 106 m which is the same water depth as the sill to the south of Prince of Wales Island (Figure 4.3b). In CAA-FB, the water depth between 70.5-72.3°N and 108-95.2°W, and the sill south of Prince of Wales Island is removed (Figure 4.3c). In CAA-BS, the sill in Barrow Strait is removed and the water depth is set to 300 m between 70-73.7°N and 105-100°W (Figure 4.3d).

The Pan-Arctic configuration domain, model grids, and the bathymetry are shown in Figure 4.2b. There are 568 $\times$ 400 points in the horizontal and the model resolution ranges from 9 km to 15 km, with 11 km in Lancaster

Sound. The bathymetry in the Pan-Arctic configuration is obtained from ETOPO1 (Amante and Eakins, 2009). There are two open boundaries, one located in the Atlantic Ocean, and the other located in the Pacific Ocean. The monthly boundary data is derived from a 1/4 ° global model based on the eddy permitting ORCA025 configuration (Barnier et al., 2006) and were averaged over years 1979-2004. There are three buffer zones, two located near the open boundaries, with another located in Foxe Basin. The width of the buffer zones is 40 grid points. The temperature and salinity is restored to the monthly climatology (PHC data), with relaxation time scale ranging from 1 day near the boundary to 40 days at the outer edge of the buffer zone. There is no sea surface salinity restoring in this configuration. The surface air temperature and downwelling shortwave radiation is still from the CORE dataset and is not adjusted. The Pan-Arctic experiment ran for 18 years. Unless specified otherwise, mean quantities for the Pan-Arctic configuration in this paper will refer to years 16-18.

4.3 Model Evaluation

Focusing on the regions important for our scientific questions (McClure Strait through to Lancaster Sound, in the central archipelago), we will first show that the model results agree rather well enough with the observations to allow us to use the model fields to explain the relevant dynamics.

4.3.1 Sea ice

Sea ice concentration is an important parameter to be examined because there are satellite measurements to validate the models' performance. Figure 4.5a and 4.5b compare the 1984-2004 mean sea ice concentration fields in July derived from SMMR (August 1984-1987) and SMM/I (September 1987-2004) data sets (Cavalieri et al., 2008) with the results in CAA control experiment.

Overall, the spatial pattern of the model simulated sea ice concentration is consistent with the satellite measurement. The North Water Polynya, located in northern Baffin Bay between Ellesmere Island and Greenland, is an important habitat for wildlife. The model simulated spatial patterns of the North Water Polynya is similar to observed patterns. In McClure Strait and Viscount Melville Sound, the sea ice is nearly stagnant from December to May while the sea ice moves eastward in eastern Lancaster Sound. The sea ice motion pattern in Parry Channel agrees well with observations (Agnew et al., 2008). Here the sea ice concentration in July is used because the sea ice concentration in Baffin Bay is better simulated after correcting the DSR from AGR dataset. In southeastern Baffin Bay, the sea ice concentration is low because of the warm West Greenland Current. The air temperature gradient seems play more important than the water temperature (Barber et al., 2001). In the southern Beaufort Sea, there is the Cape Bathurst polynya, which is located in the Amundsen Gulf, as the wind drives the sea ice westward in July. Both model results and observational data show that Baffin Bay is nearly ice free in August and September and the sea ice gradually expands to cover the whole model domain by January (not shown here).

Another important aspect of sea ice is its thickness. In April, the modeled ice thickness is highest near the coast of the northwest of the Queen Elizabeth Islands, which is consistent with observational results (Bourke and Garrett, 1987; Melling, 2002). The ice thickness reduces from the west coast of Prince Patrick Island to the Beaufort Sea north of Alaska (Figure 4.5c). The ice thickness also reduces with latitude from northwest of the Queen Elizabeth Islands to Parry Channel (Figure 4.5c). The difference of ice thickness from February to May in most of the model domain is less than 0.5 m. Table 4.3 shows some observations of ice thickness compared to modelled ice thickness. The modelled ice thickness compares well with those found in the observations

in most regions. Interannual variability in ice thickness may affect the comparison. For example, the ice thickness ranges from 0.9 m to 2 m at Clyde River in April.

4.3.2 Ocean currents

There is southeastward flow through McClure Strait. Part of the current through McClure Strait comes from the southern Beaufort Sea, while part of inflow comes from a southwestward flow north of CAA. The core of the current is on the north side in McClure Strait and diverts to the southern side in eastern Viscount Melville Sound (Figure 4.6). The current that originates north of the archipelago also flows southward into Parry Channel via Byam Martin Channel and Penny Strait, with the surface velocities in the range of 2-9 cm s^{-1}. Near the northern entrance of M'Clintock Channel, part of the current from McClure Strait bifurcates into M'Clintock Channel and then flows into Peel Sound via Franklin Strait. The southward surface current peaks at 7 cm s^{-1} in northwestern M'Clintock Channel.

The current through Barrow Strait intrudes into northern Peel Sound as a cyclonic current loop (Figure 4.7a). The mean volume transport through Peel Sound in April is 0.19 Sv in the CAA control experiment and 0.20 Sv in the Pan-Arctic experiment, which are similar to a previous estimate (0.15 Sv) (Prinsenberg and Bennett, 1989). As the sill in Dolphin and Union Strait is 26 m in the IBCAO dataset, the mean volume transport through Dolphin and Union Strait is 0.02 Sv in the CAA control experiment. The water flow through Peel Sound has mainly gone through M'Clintock Channel. In eastern Barrow Strait, the core of the eastward current is located on the south side (Figure 4.8). The model currents show a jet just off the shelf break at the south side in April, with velocities decreasing to the north (Figure 4.8), as seen by Prinsenberg and Bennett (1987). Velocities at 50 m are $\sim$ 13 cm s^{-1}, close

to the observed maximum (Prinsenberg and Bennett, 1987), albeit the model maximum of 18 cm s^{-1} is at the surface. Based on a section through western Lancaster Sound coincident with the moorings of Prinsenberg and Hamilton (2005), the long term mean volume transport is 0.77 Sv in the CAA control experiment and 0.85 Sv in the Pan-Arctic experiment, slightly larger than the 0.7 Sv (with interannual variations of $\pm$ 0.3 Sv), based on observations (Prinsenberg et al., 2009).

In eastern Lancaster Sound, there is cyclonic flow persistent throughout the year and the intrusive flow of the Baffin Current reaches 85°W on the north side of the sound in the Pan-Arctic experiment (Figure 4.9a). In the vicinity of Cape Warrender (Devon Island, Figure 4.9a), the current flows southward, which agrees with observation (Fissel et al., 1982). The westward current speed on the north side of the sound, which is very barotropic in the model, is about 10 cm s^{-1} (Figure 4.9b). The eastward current speed on the south side of the sound is above 20 cm s^{-1}, which is surface trapped at the shelf break (Figure 4.9b). Although the mean current fields in the CAA configuration is eastward in eastern Lancaster Sound, the penetration of the Baffin Current is more intermittent.

In the Pan-Arctic configuration, part of the flow bifurcates into Prince Regent Inlet and flows through the Gulf of Boothia and Fury and Hecla Strait into Foxe Basin, as discussed by (Collin, 1962; Barry, 1993). Since the CAA configuration only restores temperature and salinity in northern Foxe Basin, the currents in Prince Regent Inlet are weak. Thus, the CAA control experiment has a stronger eastward transport into Lancaster Sound, making it harder for the Baffin Current to penetrate into the sound.

4.4 M'Clintock Channel

The southward flow in M'Clintock Channel is persistent throughout the year. The mean volume transport through Viscount Melville Sound is 0.50 Sv in the CAA control experiment, while the mean volume transport through the M'Clintock Channel is 0.27 Sv in the CAA control experiment. In the Pan-Arctic experiment, the volume transport through Viscount Melville Sound and M'Clintock Channel are 0.37 Sv, and 0.21 Sv respectively. More than half of water from Viscount Melville Sound flows southward into M'Clintock Channel, before eventually looping round Prince of Wales Island and flowing northward into Peel Sound and then eastern Barrow Strait. Why is there southward flow in M'Clintock Channel? The importance of southward flow in M'Clintock Channel is discussed further in the discussion. In winter (December to May), because the sea ice in M'Clintock Channel could not move due to strong internal ice stress, the ice stress on the ocean retards the surface currents in M'Clintock Channel. Therefore, the surface stress on the ocean cannot drive the southward flow in M'Clintock Channel.

Now we study the momentum balance of the currents near the northern end of M'Clintock Channel. The horizontal momentum equation is given in the following:

$$\overbrace{\partial_t \mathbf{U}_h}^{1} + \overbrace{(\bigtriangledown \times \mathbf{U}_h)_z \mathbf{k} \times \mathbf{U}_h}^{2} + \overbrace{f\mathbf{k} \times \mathbf{U}_h}^{3} + \overbrace{1/\rho_0 \bigtriangledown p}^{4} + \overbrace{w\partial_z \mathbf{U}_h + 0.5 \bigtriangledown \mathbf{U}_h^2}^{5} + \overbrace{\partial_z(\nu_v \partial_z \mathbf{U}_h)}^{6} + \overbrace{\bigtriangledown(A_{lm} \bigtriangledown \cdot \mathbf{U}_h) - \bigtriangledown \times (A_{lm} \bigtriangledown \times \mathbf{U}_h)}^{7} = 0 \qquad (1)$$

where: $\mathbf{U}_h = (u, v)$ and w are the horizontal and vertical velocities, respectively; f the Coriolis parameter; p the hydrostatic pressure; ρ_0 a reference density; $\mathbf{k}$ the unit upward vertical vector; z the depth; ν_v the vertical eddy viscosity; A_{lm} horizontal eddy viscosity coefficients. Terms in Equation (1) are the acceleration term (term 1), metric term (term 2), Coriolis term (term 3), pressure gradient term (term 4), nonlinear advection term (term 5), ver-

tical diffusion term (term 6), horizontal viscosity term (term 7). Note there is southward flow in M'Clintock Channel in a global 1 degree model in which neptune effect is considered (Holloway and Wang, 2009).

Figure 4.10 shows the meridional momentum balance along line A over the top 50 m. We study the meridional momentum balance because we try to understand why the water flows southward into M'Clintock Channel. The ageostrophic acceleration is defined by the sum of the pressure gradient term and the Coriolis term. At line A, the meridional pressure gradient term is northward and is mainly balanced by Coriolis term and the ageostrophic acceleration is small. When the water flows to the northern end of M'Clintock Channel, the ageostrophic acceleration is negative since the pressure gradient reduces due to the direction change of the coastline. Therefore, the water turns southward into M'Clintock Channel because of the Coriolis term. The ageostrophic acceleration is mainly balanced by the vertical diffusion term and the nonlinear advection term, with the horizontal viscosity term less than 1×10^{-8} m s^{-2}.

Although one of major reasons that the water flows into M'Clintock Channel is because of the Coriolis effect, topography also plays an important role in the southward flow in M'Clintock Channel. The water depth is more than 300 m in central Viscount Melville Sound west of M'Clintock Channel decreasing to 131 m at a sill in Barrow Strait (Figure 4.3a). Near the northern entrance of M'Clintock Channel, the water depth decreases more slowly than to the east into Barrow Strait. There is also a sill with a depth of 106 m to the south of Prince of Wales Island.

Here we present some sensitivity experiments, focusing on the volume transport averaged over the second year of integration. The volume transport through M'Clintock Channel in CAA-MC is 0.26 Sv, which is nearly the same as the value in CAA-NS. In CAA-FB, the volume transport through

M'Clintock Channel increases to 0.37 Sv because of topographic steering. Therefore, the volume transport is strongly influenced by the sill depth in Franklin Strait instead of the deep trough in M'Clintock Channel. The volume transport through M'Clintock Channel dereases to 0.13 Sv in CAA-BS as the flow tries to follow the f/h contours, which are approximately parallel to the local isobaths, h. The sill depth in Barrow Strait can also have a strong influence on the flow through M'Clintock Channel.

4.5 Eastern Lancaster Sound

In the Pan-Arctic experiment, there is inflow into the northern part of Lancaster Sound from Baffin Bay, following the bathymetry, and flowing to the west before recirculating south of Devon Island to join the eastward flowing circulation from Barrow Strait (Figure 4.9a). Holloway and Wang (2009) show that the neptune effect can explain the penetration of the Baffin Current. Now we try to understand why the Baffin Current doesn't penetrate farther into the archipelago.

Vorticity dynamics can be used to study the circulation in eastern Lancaster Sound. We compute the Ertel's potential vorticity, averaged over the upper water column (top 300 m, or the bottom, whichever is shallower) from the Pan-Arctic experiment (Figure 4.7a). Note the choice of 300 m is arbitrary, but the results are not sensitive to the exact depth used. Ertel's potential vorticity (EPV) is $\frac{1}{\rho_0}(f+\zeta)\cdot\rho_z$, where f is the Coriolis parameter, ζ is the relative vorticity, ρ_z is the vertical density gradient, and ρ_0 takes the constant value of 1020 $kg\ m^{-3}$. The average water depth at the entrance of eastern Lancaster Sound is between 700 m to 800 m. Lancaster Sound gradually shoals westward to a sill of less than 200 m depth in Barrow Strait. Although the topography applies a strong constraint to the EPV field, there is also a significant impact of the stratification. In order to understand the effect of stratifica-

tion, the surface salinity in eastern Lancaster Sound is shown in Figure 4.9c. Because the flow is from relatively fresh water in the Beaufort Sea to saline water in Baffin Bay, the surface salinity decreases from Barrow Strait to Baffin Bay. The surface water on the south side of the sound is fresher than that on the north side, which agrees with observations (Fissel et al., 1982). Since the salinity difference is smaller at depth compared to the surface layer, the stratification pattern is similar to the surface salinity pattern. Thus there is an EPV gradient along and across Lancaster Sound matching the salinity contours (Figure 4.9c). ρ_z becomes larger when the water flows along the north side of eastern Lancaster Sound. Because of conservation of potential vorticity, the water must flow southward because f reduces when the current moves south. Figure 4.9d shows the EPV contours and vertical velocity at 81.4°W in eastern Lancaster Sound. In general, at the same depth, the EPV increases from the north side of the sound to the south side (Figure 4.9d). We thus find that there is downwelling in the central part of eastern Lancaster Sound (Figure 4.9d). Because the Baffin Bay waters are denser, they will sink under the lighter waters on the south side.

4.6 Summary and Discussion

A coupled ocean/sea-ice CAA model has been developed to simulate the circulation in the CAA. Both sea ice concentration and ice thickness are consistent with observed results after adjusting the surface air temperature and the DSR. The vertical structure and transports in Barrow Strait agrees with observed results. Furthermore, the southward flow in M'Clintock Channel and northward flow in Peel Sound is reproduced.

The classic view is that the flow through Parry Channel is controlled by the sea surface gradient between the Arctic and Baffin Bay (Stigerbrandt, 1984). However, model results shows that the flow is more complex than

previously thought. More than half of the water which flows through Vicsount Melville Sound loops around Prince of Wales Island and then flows through Peel Sound has mainly come from M'Clintock Channel. Our analysis shows that the flow in M'Clintock Channel is produced by a southward ageostrophic acceleration. The southward flow is also strongly influenced by sills at south of Prince of Wales Island and Barrow Strait. Our analysis also reveals that the stratification in combination with the topography prevents westward flow further into Barrow Strait and there is downwelling as the flow recirculates towards the south in eastern Lancaster Sound.

Figure 4.11a and 4.11b shows the sea ice concentration, mean ice motion and wind vectors in August and September, respectively. Because of southward current underneath, the ice moves upwind to the south in M'Clintock Channel in August. It is thus driven by the ocean currents whose path is governed by the topographic and vorticity constraints discussed above. In September, the sea ice concentration is lower in Peel Sound than that in M'Clintock Channel (Figure 4.11b), consistent with observed results from SSM/I. Because of southeastward winds and southward surface currents in M'Clintock Channel, the sea ice moves southward in M'Clintock Channel and the dynamical import of sea ice is large. This agrees with Agnew et al. (2008) who used AMSR-E (Enhanced Resolution Advanced Microwave Scanning Radiometer) imagery to estimate sea ice drift in the CAA from September to June. In Peel Sound, because the winds are southeastward and the surface currents are northward, the sea ice motion is slow and thus the amount of dynamical import of sea ice into Peel Sound is not large. Since the dynamical import of sea ice into M'Clintock Channel is larger than that of Peel Sound, the sea ice concentration in M'Clintock Channel is higher than that in Peel Sound in September. Similarly, the concentration of multiyear ice (MYI) is high in M'Clintock Channel in summer (Howell et al., 2008). Terwisscha van Scheltinga et al. (2010) stud-

ied sea ice concentration and fluxes in the CAA using a sea-ice model coupled to a slab ocean. In their experiments, the lack of ocean currents led to their model producing similar sea ice concentrations in both M'Clintock Channel and Peel Sound, again highlighting the importance of the underlying oceanic currents.

The migration of beluga whale, narwhals, and harp seals are linked to ice-edge productivity (Tynan and DeMaster, 1997). Bowhead whales are adapted to live in the loose ice edges and their migrations roughly track the advance and retreat of the ice edge (Dyke et al., 1996). Although Peel Sound is part of the summer home range of harp seal, bowhead whale, beluga whale, and narwhal, they are not found in M'Clintock Channel (Stephenson and Hartwig, 2010; Dietz et al., 2008). The persistent sea ice in M'Clintock Channel limits the movements of narwhal, bowhead whale, beluga whale, and various species of seal (Harington, 1966; Dyke et al., 1996). Therefore, the southward currents and sea ice in M'Clintock Channel have an impact on the marine mammals. Because the currents are mainly controlled by the Coriolis force and topography, one may not expect significant changes (such as enhanced sea ice import to Peel Sound) even in a changing climate.

One of the possible shipping routes of the northwest passage is through Peel Sound, Victoria Strait and Amundsen Gulf (Pharand, 1984). This route has always been sensitive to the import of MYI into McClure Strait and M'Clintock Channel. It was probably the fate of the Franklin Expedition in 1845 to be trapped in this oceanic advected MYI northwest of King William Island (M'Clintock, 1859). Again, Because the currents are mainly controlled by the Coriolis force and topography, as long as thick MYI enters McClure Strait, one may expect it to be advected into M'Clintock Channel. Thus even in a warmer climate, one may expect difficulties with using this route for navigation.

Although the modeled circulation agrees well with observed results, the

CAA configuration can be improved. This will include open boundaries and tidal forcing that should be considered. Additionally, the model has been run with interannual forcing, which will be used in future studies.

Table 4.1: Details on the model configurations and experiments used in the paper.

Configuration	CAA	Pan-Arctic
Ocean time step(s)	480	1800
Ice thermodynamic time step(s)	2400	1800
EVP subcycling time step(s)	5	1
Air-Ice drag coefficeint	0.00163	0.00163
Ice-Ocean drag coefficient	0.005	0.005
Ice strength parameter(N m^{-2})	27500	23000
Minimum ice thickness(m)	0.05	0.05

Table 4.2: List of six numerical experiments.

	Name of run	Domain	SSS restoring
1	CAA control	CAA real	yes
2	Pan-Arctic	Pan-Arctic	yes
3	CAA-NS	CAA real	no
4	CAA-MC	CAA+flat MC	no
5	CAA-FB	CAA+flat FB	no
6	CAA-BS	CAA+flat BS	no

Table 4.3: Observed ice thickness and modeled ice thickness (m).

Location	Observation	CAA control experiment
Mackenzie Shelf (April)	2 (Melling et al., 2005)	2.5
Queen Elizabeth Islands region (March-May)	3.4 (1.6-5.5) (Melling, 2002)	2.5-4.5
McClure Strait (Feburary)	4.2 (McLaren et al., 1984)	3
Northern Peel Sound (April)	1.9 (Prinsenberg and Bennett, 1989)	2
Clyde River (April)	1.5 $\pm$ 0.3 (Tang et al., 2004)	1.5
Lincoln Sea (May)	4.7 $\pm$ 2.2 (2004); 5.2 $\pm$ 2.4 (2005) (Haas et al., 2006)	4.5

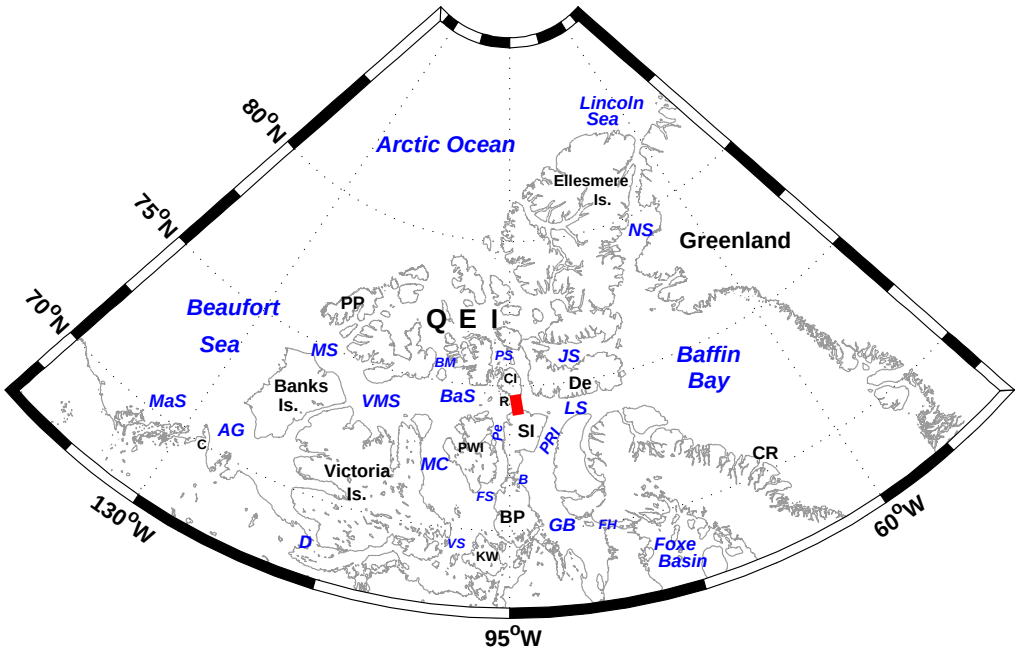

Figure 4.1: The name of the island, straits, and locations in the model domain, AG: Amundsen Gulf, B: Bellot Strait, D: Dolphin and Union Strait, BM: Byam Martin Channel, BaS: Barrow Strait, FH: Fury and Hecla Strait, FS: Franklin Strait, GB: Gulf of Boothia, LS: Lancaster Sound, JS: Jones Sound, MaS: Mackenzie Shelf, MC: M'Clintock Channel, MS: McClure Strait, NS: Nares Strait, Pe: Peel Sound, PS: Penny Strait, VMS: Viscount Melville Sound, VS: Victoria Strait, C: Cape Bathurst, CR: Clyde River, De: Devon Island, CI: Cornwallis Island, KW: King William Island, R: Resolute Bay, PP: Prince Patrick Island, PWI: Prince of Wales Island. PRI: Prince Regent Inlet, QEI: Queen Elizabeth Islands, SI: Somerset Island, The thick red bold line shows the location of a section in Figure 4.8. MS, VMS, BaS, and LS constitute Parry Channel.

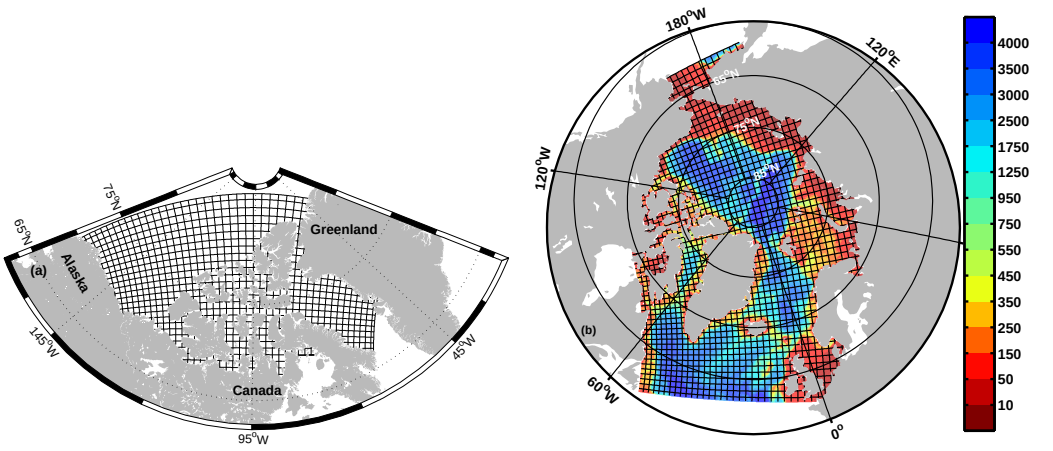

Figure 4.2: (a) The CAA configuration, (b) The Pan-Arctic configuration with the background bathymetry [m].

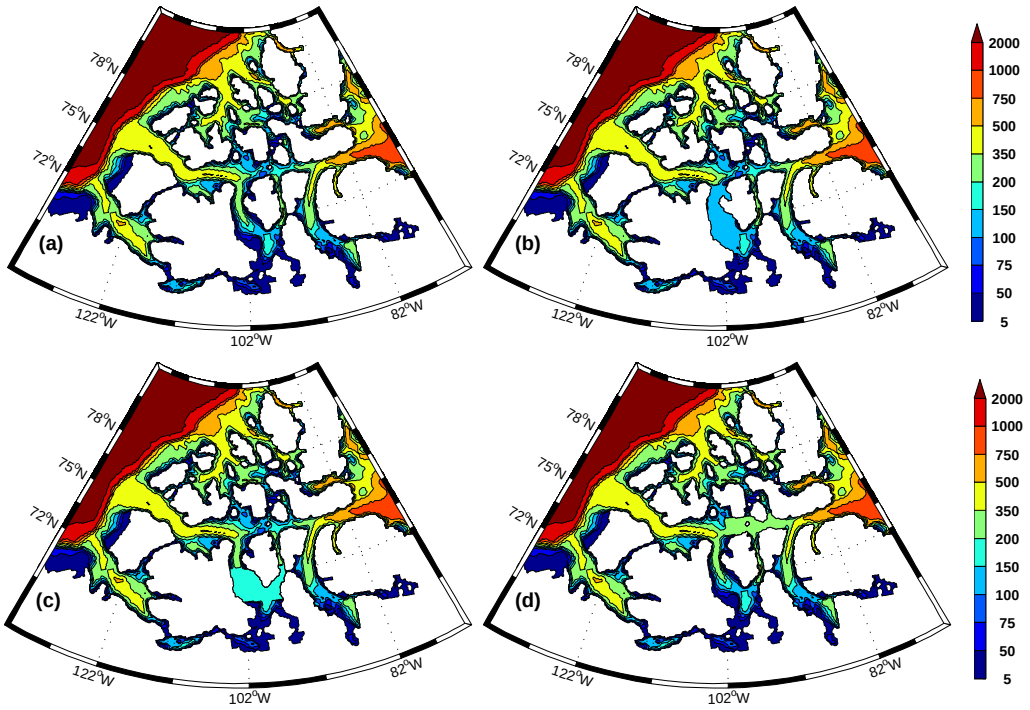

Figure 4.3: Bathymetry [m] in a) CAA control experiment (upper left), (b) experiment CAA-MC (upper right), (c) experiment CAA-FB (lower left), and (d) experiment CAA-BS (lower right).

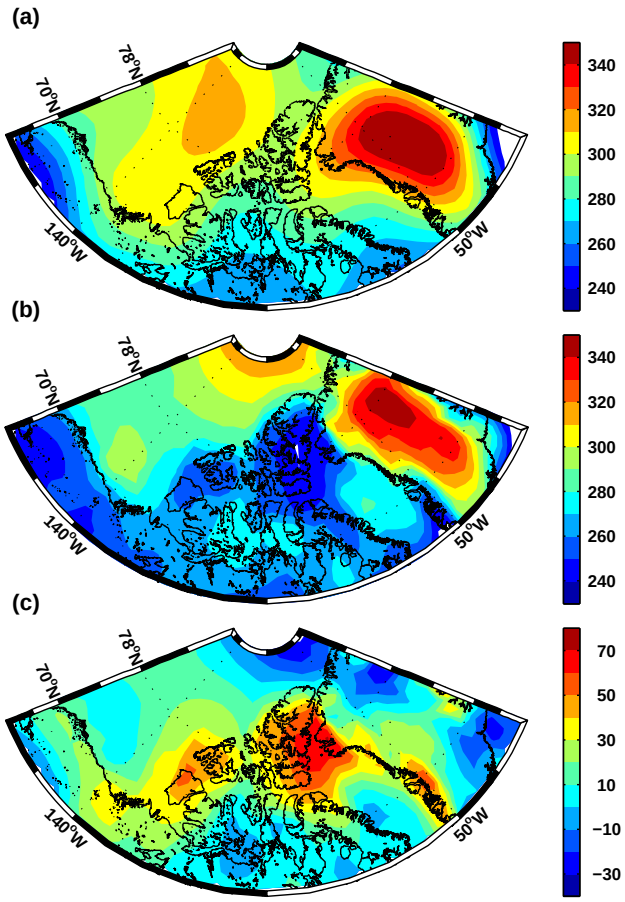

Figure 4.4: Downwelling shortwave radiation [W m^{-2}] in June (a) from the Arctic Global Radiation dataset, (b) from Large and Yeager (2004) dataset, and (c) the difference between the AGR dataset and Large and Yeager (2004) dataset for June.

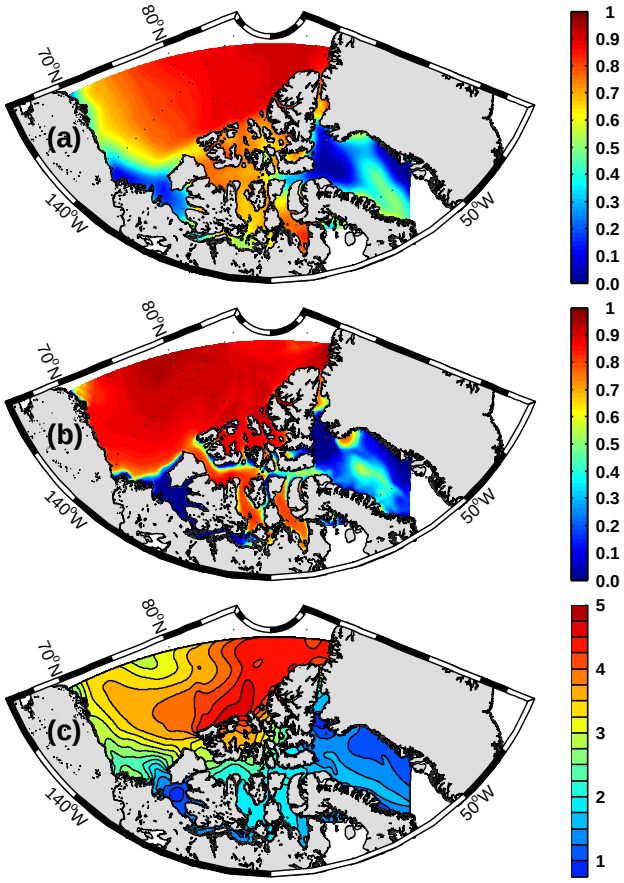

Figure 4.5: (a) Mean sea ice concentration in July for the period 1984-2004 from SSM/I. Simulated (b) mean sea ice concentration in July and (c) mean sea ice thickness [m] in April averaged over years 6-8 in the CAA control experiment.

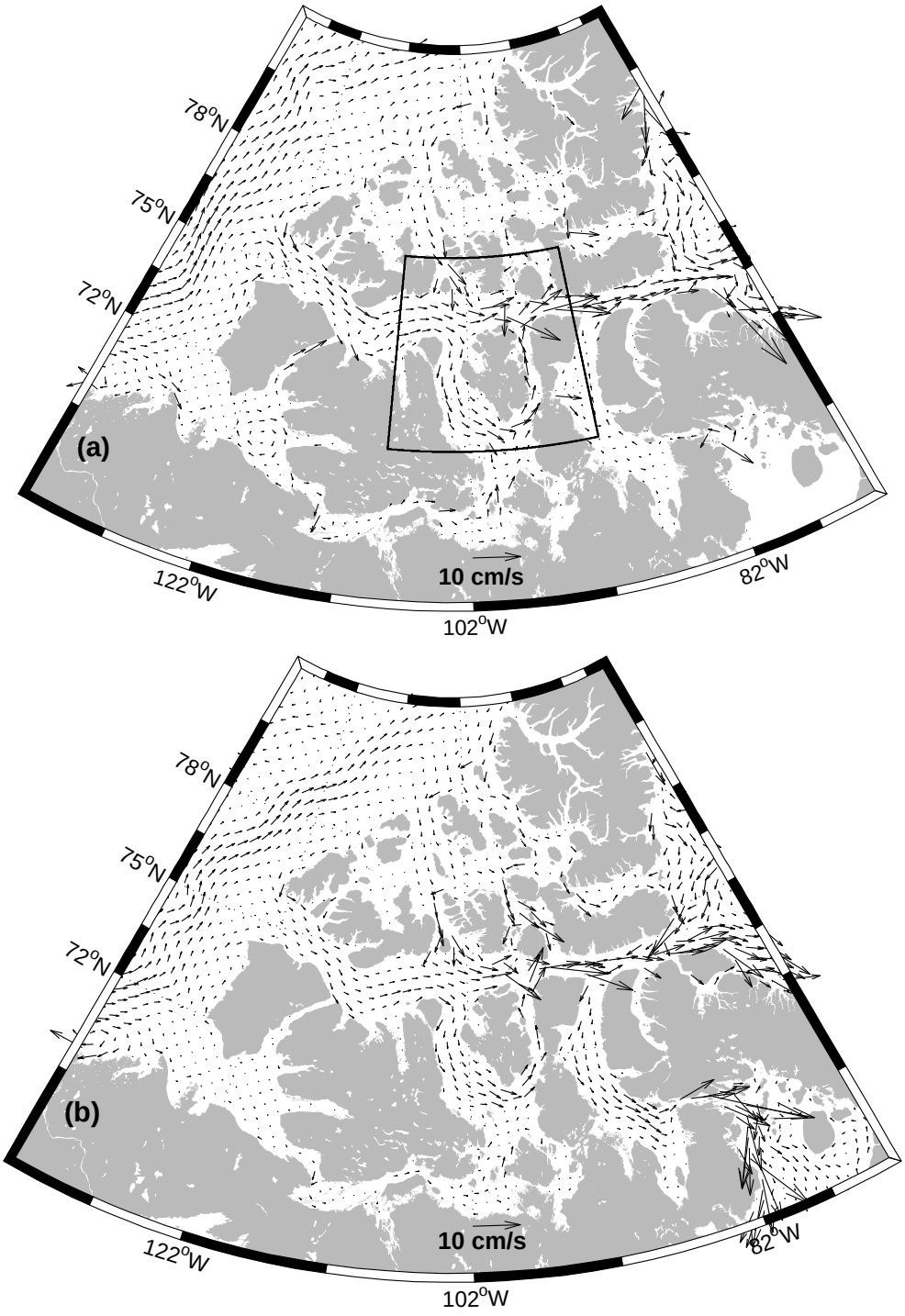

Figure 4.6: (a) The mean currents in the CAA averaged over the top 300 m and over years 6-8 in the CAA control experiment, with one fifth of the horizontal grid points shown. The box shows the zoomed region in Figure 5, (b) as in (a), but for the Pan-Arctic experiment averaged over years 16-18, with one third of the horizontal grid points shown.

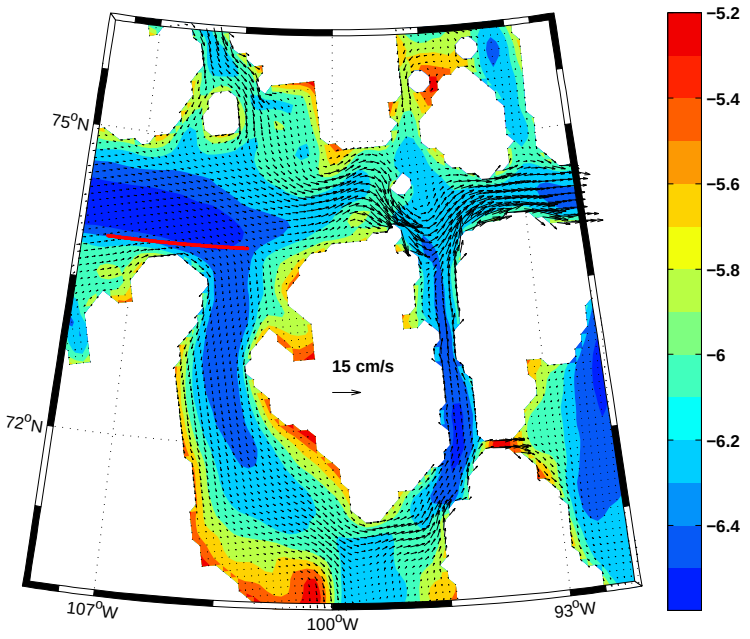

Figure 4.7: Zoom of the currents from Figure 4.6a. The background field is $\log_{10}(f/h)$. The red line shows the position of line A, where momentum balance is shown in Figure 4.10.

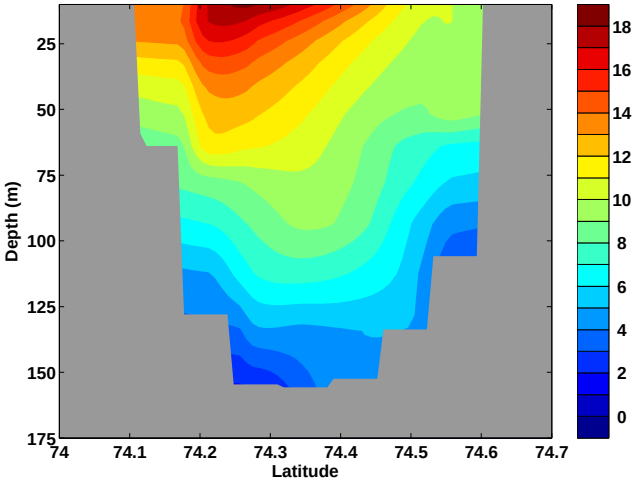

Figure 4.8: The mean cross section current speed [cm s^{-1}] in Barrow Strait (section shown in Figure 4.1) in April averaged over years 6-8 in the CAA control experiment.

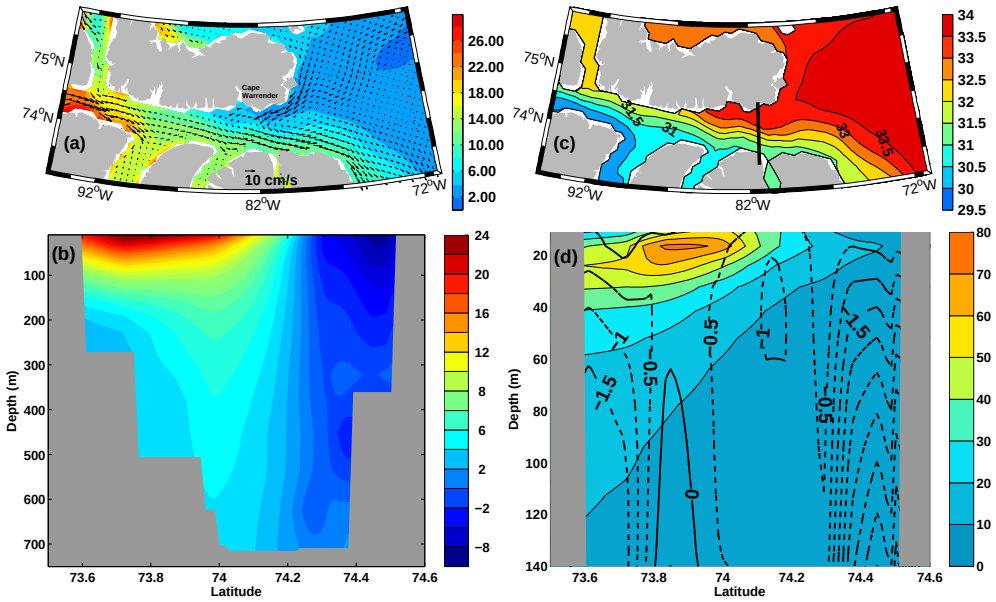

Figure 4.9: (a) The mean Ertel's potential vorticity and currents averaged over the top 300 m in eastern Lancaster Sound. (b) The cross section current speed [cm s^{-1}] at 81.4°W with the location of the section shown by the thick bold line in subfigure c. (c) Surface salinity in eastern Lancaster Sound. (d) The vertical velocity [10^{-5} m s^{-1}] (contours) over the top 140 m overlaying Ertel's potential vorticity at 81.4°W. Downward velocity is negative. The units for the Ertel's potential vorticity are 10^{-10} m^{-1} s^{-1}. All values are averaged over years 16-18 in the Pan-Arctic experiment.

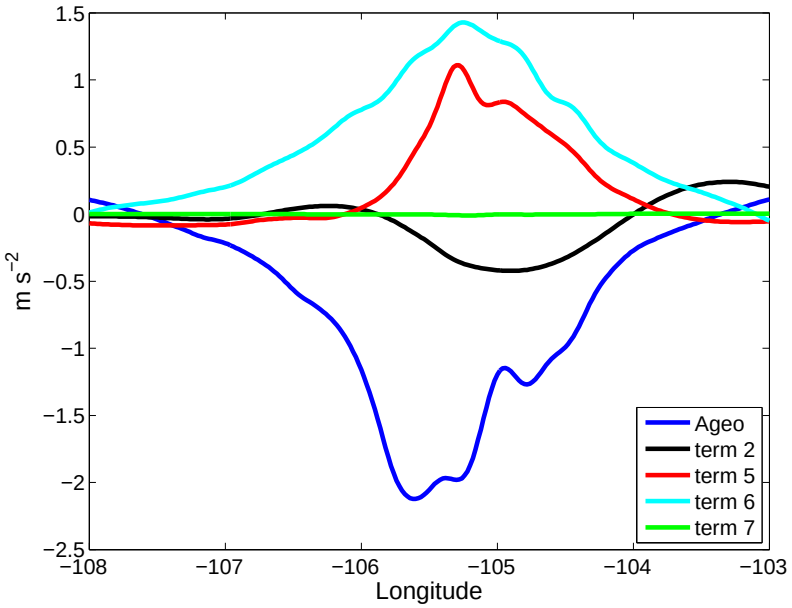

Figure 4.10: Meridional momentum balance averaged over top 50 m along line A, which is shown in Figure 4.7. Ageo represents ageostrophic acceleration. The values have been multiplied by 10^7.

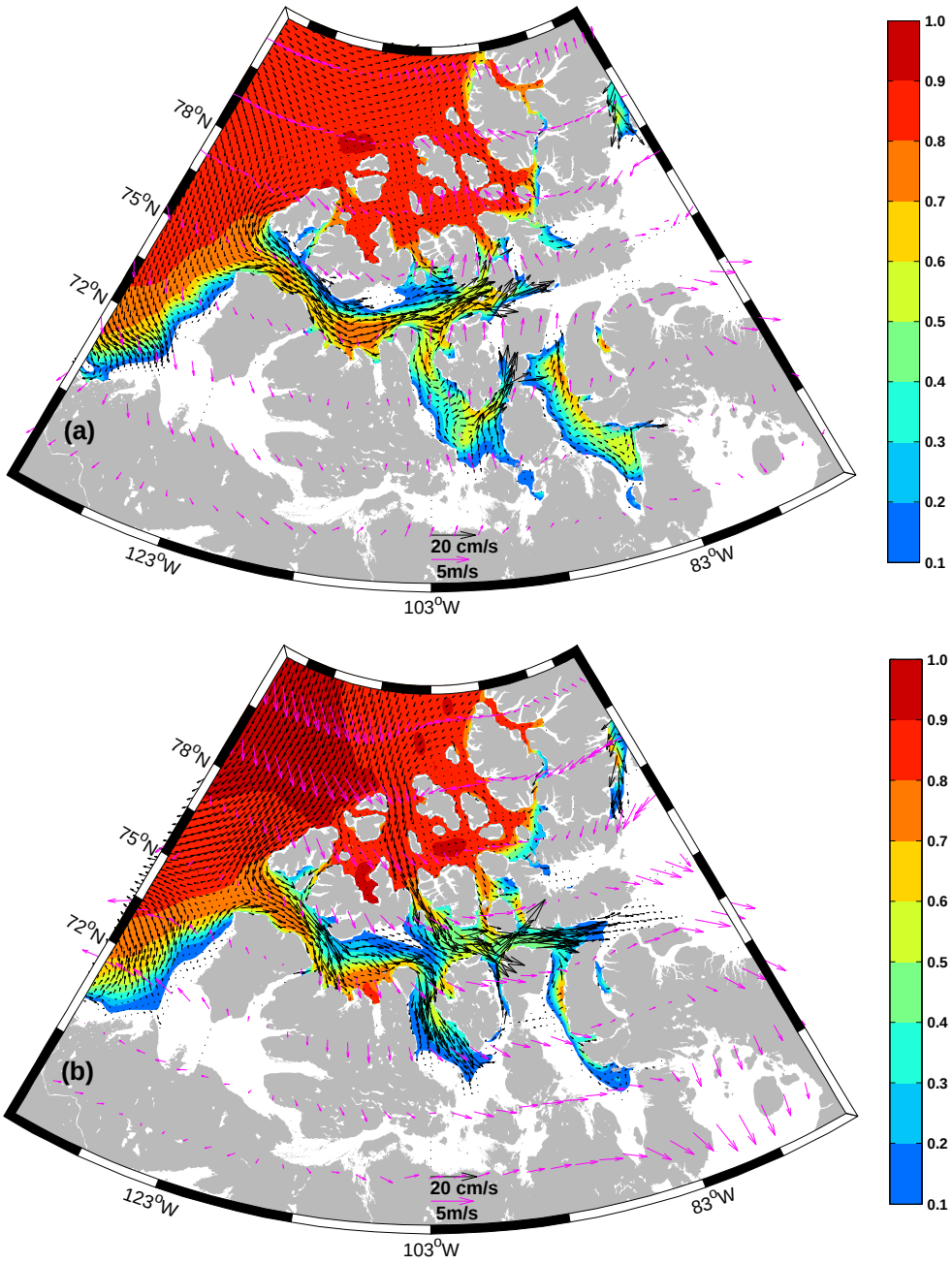

Figure 4.11: (a) the CAA control experiment ice concentration (color contours) and ice motion vectors (black arrows) and wind vectors (magenta arrows) in August and (b) in September.

Bibliography

Aagaard, K., and E. Carmack, 1989: The role of sea ice and other fresh water in the Arctic circulation. *Journal of Geophysical Research*, **94**, 14485–14498.

— 1994: The Arctic Ocean and climate: A perspective. *The Polar Oceans and Their Role in Shaping the Global Environment: The Nansen Centennial Volume*, O. M. Johannessen, R. D. Muench, and J. E. Overland, eds., Amer. Geophys. Union, USA, volume 85 of *Geophysical Monograph*, 4–20.

Agnew, T., A. Lambe, and D. Long, 2008: Estimating sea ice area flux across the Canadian Arctic Archipelago using enhanced AMSR-E. *Journal of Geophysical Research*, **113**, doi:10.1029/2007JC004582.

Aksenov, Y., S. Bacon, A. C. Coward, and P. N. Holliday, 2010: Polar outflow from the Arctic Ocean: A high resolution model study. *Journal of Marine System*, **83**, doi:10.1016/j.jmarsys.2010.06.007, 14–37.

Amante, C., and B. W. Eakins, 2009: ETOPO1 1 Arc-Minute global relief model:Procedures, data sources and analysis. NOAA Technical Memorandum NESDIS NGDC-24.

Barber, D., J. Hanesiak, W. Chan, and J. Piwowar, 2001: Sea-ice and meteorological conditions in Northern Baffin Bay and the North Water polynya between 1979 and 1996. *Atmosphere-Ocean*, **39**, 343–359.

Barber, F., 1965: Current observations in Fury and Helca Strait. *J. Fish. Res. Board Can.*, **22**, 225–229.

Barnier, B., G. Madec, T. Penduff, J.-M. Molines, A.-M. Treguier, J. L. Sommer, A. Beckmann, A. Biastoch, C. Bning, J. Dengg, C. Derval, E. Durand, S. Gulev, E. Remy, C. Talandier, S. Theetten, M. Maltrud, J. McClean, and B. D. Cuevas, 2006: Impact of partial steps and momentum advection schemes in a global ocean circulation model at eddy-permitting resolution. *Ocean Dynamics*, **56**, doi:10.1007/s10236-006-0082-1, 543–567.

Barry, R. G., 1993: Canada's cold seas. *Canada's cold environment*, H. M. French and O. Slaymaker, eds., McGill Queen's University Press, Canada, NATO Science for Peace and Security Series, 29–61.

Blanke, B., and P. Delecluse, 1993: Variability of the tropical Atlantic Ocean simulated by a general circulation model with two different mixed-layer physics. *Journal of Physical Oceanography*, **23**, 1363–1388.

Bouillon, S., M. A. M. Maqueda, V. Legat, and T. Fichefet, 2009: An elasticviscousplastic sea ice model formulated on Arakawa B and C grids. *Ocean Modelling*, **27**, doi:10.1016/j.ocemod.2009.01.004, 174–184.

Bourke, R. H., and R. P. Garrett, 1987: Sea ice thickness distribution in the Arctic Ocean. *Cold Regions Sciences and Technology*, **13**, 259–280.

Box, J., J. Key, J. Maslanik, and M. Serreze, 1998: Arctic Global Radiation (AGR) data set. National Snow and Ice Data Center, Boulder, digital Media.

Canadian Ice Service, 2007: Canadian ice service archive documentation seriesregional charts: History, accuracy, and caveats. Ottawa.

Carmack, E., 2007: The alpha/beta ocean distinction: A perspective on fresh-

water fluxes, convection, nutrients and productivity in high-latitude seas. *Deep Sea Research Part II*, **54**, doi:10.1016/j.dsr2.2007.08.018, 2578–2598.

Cavalieri, D., C. Parkinson, P. Gloersen, , and H. J. Zwally, 2008: Sea ice concentrations from Nimbus-7 SMMR and DMSP SSM/I passive microwave data. National Snow and Ice Data Center, Boulder, USA, digital Media.

Collin, A., 1962: Oceanography in the Canadian Arctic. *Canadian Geographer*, **6**, 120–128.

de Lange Boom, B., H. Melling, and R. A. Lake, 1987: Late winter hydrography of the northwest passage. *Canadian technical report of hydrography and ocean sciences*, Institute of Ocean Science, Washington, D.C, USA.

Dickson, R., B. Rudels, S. Dye, M. Karcher, J. Meincke, and I. Yashayaev, 2007: Current estimates of freshwater flux through Arctic and subarctic seas. *Progress in Oceanography*, **73**, doi:10.1016/j.pocean.2006.12.003, 210–230.

Dietz, R., M. P. Heide-Jrgensen, P. Richard, K. L. Jack Orr, and H. C. Schmidt, 2008: Movements of narwhals (Monodon monoceros) from Admiralty Inlet monitored by satellite telemetry. *Polar Biology*, **31**, doi:10.1007/s00300-008-0466-4, 1295–1306.

Dyke, A. S., J. Hooper, and J. M. Savelle, 1996: A history of sea ice in the Canadian Arctic Archipelago based on postglacial remains of the bowhead whale (Balaena mysticetus). *Arctic*, **49**, 235–255.

Fichefet, T., and M. M. Maqueda, 1997: Sensitivity of a global sea ice model to the treatment of ice thermodynamics and dynamics. *Journal of Geophysical Research*, **102**, 12609–12646.

Fissel, D., J. Birch, H. Melling, and R. A. Lake, 1988: Non-tidal flows in the

Northwest Passage. *Canadian Technical Report of Hydrography and Ocean Sciences*, Department of Fisheries and Oceans, Sidney, BC, Canada.

Fissel, D., D.D.Lemon, and J. Birch, 1982: Major features of the summer near-surface circulation of western Baffin Bay, 1978 and 1979. *Arctic*, **35**, 180–200.

Haas, C., S. Hendricks, and M. Doble, 2006: Comparison of the sea-ice thickness distribution in the Lincoln Sea and adjacent Arctic Ocean in 2004 and 2005. *Annals of Glaciology*, **44**, 247–252.

Hannah, C. G., F. Dupont, and M. Dunphy, 2009: Polynyas and Tidal Currents in the Canadian Arctic Archipelago. *Arctic*, **62**, 83–95.

Harington, C. R., 1966: Extralimital occurrences of walruses in the Canadian Arctic. *Journal of Mammalogy*, **47**, 506–513.

Holloway, G., and Z. Wang, 2009: Representing eddy stress in an Arctic Ocean model. *Journal of Geophysical Research*, **114**, doi:10.1029/2008JC005169.

Howell, S. E., A. Tivy, J. J. Yackel1, and S. McCourt, 2008: Multi-year sea-ice conditions in the western Canadian Arctic Archipelago region of the Northwest Passage: 1968-2006. *Atmosphere-Ocean*, **46**, doi:10.3137/ao.460203, 229–242.

Hunke, E., and J. Dukowicz, 1997: An Elastic-Viscous-Plastic for sea ice dynamics. *Journal of Physical Oceanography*, **27**, 1849–1867.

Jakobsson, M., R. Macnab, L. Mayer, R. Anderson, M. Edwards, J. Hatzky, H. W. Schenke, and P. Johnson, 2008: An improved bathymetric portrayal of the Arctic Ocean: Implications for ocean modeling and geological, geophysical and oceanographic analyses. *Geophys. Res. Lett.*, **35**, doi:10.1029/2008GL033520.

Jones, E. P., and A. R. Coote, 1980: Nutrient distributions in the Canadian Archipelago: Indicators of summer water mass and flow characteristics. *Can. J. Fish. Aquat. Sci*, **37**, 589–599.

Kliem, N., and D. A. Greenberg, 2003: Diagnostic simulations of the summer circulation in the Canadian Arctic Archipelago. *Atmosphere-Ocean*, **41**, 273–289.

Kwok, R., L. T. Pedersen, P. Gudmandsen, and S. S. Pang, 2010: Large sea ice outflow into the Nares Strait in 2007. *Geophysical Research Letters*, **37**, doi:10.1029/2009GL041872, 1363–1388.

Large, W., and S. Yeager, 2004: Diurnal to decadal global forcing for ocean and sea-ice models: the data sets and flux climatologies. NCAR, NCAR technical note: NCAR/TN-460+ STR.

Madec, G., 2008: NEMO Ocean Engine. Institut Pierre-Simon Palace (IPSL), France, volume 27 of *Notes de Pole de modelisation*.

Marshunova, M., and N. T. Chernigovskii, 1971: Radiatsionnyi rezhim zarubeznhoi arktiki (radiation regime of the foreign arctic). Gidrometeorologicheskoe Izdatel'stvo, 182.

Marshunova, M., and A. Mishin, 1994: Handbook of the radiation regime of the arctic basin (results from the drift stations). Applied Physics Laboratory, University of Washington, Seattle, WA, Tech. Rep. APL UW TR 9413.

Maykut, G. A., and N. Untersteiner, 1971: Some results from a time-dependent thermodynamic model of sea ice. *Journal of Geophysical Research*, **76**, 1550–1575.

McLaren, A., P. Wadhams, and R. Weintraub, 1984: The sea ice topography

of M'Clure Strait in winter and summer of 1960 from submarine profiles. *Arctic*, **37**, 110–120.

M'Clintock, F. L., 1859: *The voyage of the 'Fox' in the Arctic seas: A Narrative of the Discovery of the Fate of Sir John Franklin and His Companions*. London J. Murray.

Melling, H., 2000: Exchanges of freshwater through the shallow straits of the North American Arctic. *Freshwater Budget of the Arctic Ocean*, E. L. et al., ed., Kluwer Academic Publishers, The Netherlands, NATO Science Series, 479–502.

— 2002: Sea ice of the northern Canadian Arctic Archipelago. *Journal of Geophysical Research*, **107**, doi:10.1029/2001JC001102.

Melling, H., T. Agnew, K. K. Falkner, D. Greenberg, C. Lee, A. Mnchow, B. Petrie, S. Prisenberg, R. Samelson, and R. A. Woodgate, 2008: Freshwater fluxes via Pacific and Arctic outflows across the Canadian Polar Shelf. *Arctic-Subarctic Ocean fluxes, defining the role of the northern seas in climate*, R. R. Dickson, J. Meincke, and P. Rhines, eds., Springer, New York, 193–247.

Melling, H., R. Lake, D. Topham, and D. Fissel, 1984: Oceanic thermal structure in the western Canadian Arctic. *Continental Shelf Research*, **3**, doi:10.1016/0278-4343(84)90010-4, 233–258.

Melling, H., D. A. Riedel, and Z. Gedalof, 2005: Trends in the draft and extent of seasonal pack ice, Canadian Beaufort Sea. *Geophysical Research Letters*, **32**, doi:10.1029/2005GL024483.

Muench, R., 1971: The physical oceanography of the northern Baffin Bay

region. *The Baffin-North Water project, scientific report 1*, Arctic institute of north America, Washington, D.C, USA.

Murray, R. J., 1996: Explicit generation of orthogonal grids for ocean models. *Journal of Computational Physics*, **126**, doi:10.1006/jcph.1996.0136, 251–273.

Pharand, D., 1984: *The Northwest Passage: Arctic straits*. Dordrecht, The Netherland, 199 pp.

Prinsenberg, S. J., and E. Bennett, 1987: Mixing and transports in Barrow Strait, the central part of the Northwest passage. *Continental Shelf Research*, **7**, doi:10.1016/0278-4343(87)90006-9, 913–935.

— 1989: Transport between Peel Sound and Barrow Strait in the Canadian Arctic. *Continental Shelf Research*, **9**, doi:10.1016/0278-4343(89)90008-3, 427–444.

Prinsenberg, S. J., and J. Hamilton, 2005: Monitoring the Volume, Freshwater and Heat Fluxes Passing through Lancaster Sound in the Canadian Arctic Archipelago. *Atmosphere-Ocean*, **43**, doi:10.3137/ao.430101, 1–22.

Prinsenberg, S. J., J. Hamilton, I. Peterson, and R. Pettipas, 2009: Observing and interpreting the seasonal variability of the oceanographic fluxes passing through Lancaster Sound of the Canadian Arctic Archipelago. *Influence of Climate Change on the Changing Arctic and Sub-Arctic Conditions*, J. C. Nihoul and A. G. Kostianoy, eds., Springer, The Netherlands, NATO Science for Peace and Security Series, 125–143.

Rigor, I. G., R. Colony, and S. Martin, 2000: Variations in surface air temperature in the Arctic from 1979-1997. *Journal of Climate*, **13**, 896–914.

Roulet, R. R., 1969: Radiation regime of arctic drifting station arlis ii, january 1964-may 1965. Department of Atmospheric Sciences, University of Washington, NR 307-252, 58.

Rudels, B., 1986: The outflow of polar water through the Arctic Archipelago and the oceanographic conditions in Baffin Bay. *Polar Research*, **4**, 161–180.

Sadler, H., 1982: Water flow into Foxe Basin through Fury and Hecla Strait. *Naturaliste Can.*, **109**, 701–707.

Serreze, M. C., M. M. Holland, and J. Stroeve, 2007: Perspectives on the Arctic's shrinking sea ice cover. *Science*, **315**, doi:10.1126/science.1139426, 1533–1536.

Serreze, M. C., J. R. Key, J. E. Box, J. A. Maslanik, and K. Steffen, 1998: A new monthly climatology of global radiation for the Arctic and comparisons with NCEP-NCAR reanalysis and ISCCP-C2 fields. *Journal of Climate*, **11**, 121–136.

Shine, K. P., and A. Henderson-Sellers, 1985: Development of a turbulence closure model for geophysical fluid problems. *Journal of Geophysical Research*, **90**, 2243–2250.

Sou, T., and G. Flato, 2009: Sea ice in the Canadian Arctic Archipelago: Modeling the past (1950–2004) and the future (2041–60). *Journal of Climate*, **22**, doi:10.1175/2008JCLI2335.1, 2181–2198.

Steele, M., R. Morley, and W. Ermold, 2001: PHC: A global ocean hydrography with a high-quality Arctic Ocean. *Journal of Climate*, **14**, 2079–2087.

Stephenson, S., and L. Hartwig, 2010: The Arctic Marine Workshop. *Proceedings of the Arctic Basin Symposium*, Freshwater Institute, Winnipeg, Manitoba, Can. Manuscript Rep. Fish. Aquat. Sci. 2934.

Stigerbrandt, A., 1984: The North Pacific: a global-scale estuary. *Journal of Physical Oceanography*, **14**, 464–470.

Tang, C. C., C. K. Ross, T. Yao, B. Petrie, B. M. DeTracey, and E. Dunlap, 2004: The circulation, water masses and sea-ice of Baffin Bay. *Progress in Oceanography*, **63**, doi:10.1016/j.pocean.2004.09.005, 183–228.

Terwisscha van Scheltinga, A., P. G. Myers, and J. D. Pietrzak, 2010: A finite element sea ice model of the Canadian Arctic Archipelago. *Ocean Dynamics*, **60**, doi:10.1007/s10236-010-0356-5, 1539–1558.

Treguier, A. M., B. Barnier, A. P. de Miranda, J. M. Molines, N. Grima, M. Imbard, G. Madec, C. Messager, T. Reynaud, and S. Michel, 2001: An eddy permitting model of the Atlantic circulation: Evaluating open boundary conditions. *Journal of Geophysical Research*, **106**, 22115–22129.

Tynan, C. T., and D. P. DeMaster, 1997: Observations and predictions of Arctic climatic change: potential effects on marine mammals. *Arctic*, **50**, 308–322.

Weller, G., and B. Holmgren, 1974: Summer global radiation and albedo-data for three stations in the arctic basin, ice island t-3, barrow, prudhoe bay, 1971-1973. Geophysical Institute, University of Alaska, Fairbank, Tech. Rep. No. 2, December 1974, 31.

Wenzel, G., 1978: The harp-seal controversy and the Inuit economy. *Arctic*, **31**, 3–6.

Zhang, J., and D. A. Rothrock, 2003: Modeling global sea ice with a thickness and enthalpy distribution model in generalized curvilinear coordinates. *Mon. Wea. Rev.*, **131**, 845–861.

Chapter 5

Seasonal circulation in the CAA

5.1 Introduction

The Canadian Arctic Archipelago (CAA) is a complex network of straits and basins connecting the Arctic Ocean and the Atlantic Ocean. The CAA is one of the main pathways for freshwater outflow from the Arctic Ocean to the Atlantic Ocean (Dickson et al., 2007). This freshwater may impact the sub-polar gyre of the North Atlantic on issues from deep water formation (Aagaard and Carmack, 1989, 1994) to nutrient supply and productivity (Carmack, 2007). The importance of the freshwater outflow from the CAA may become more important in future climate scenarios (Dickson et al., 2007).

There is a strong seasonal cycle of volume transport through Barrow Strait (Prinsenberg and Bennett, 1987) and western Lancaster Sound (Melling et al., 2008). The volume transport through west Lancaster Sound is highest in August and lowest in winter (Melling et al., 2008). Prinsenberg and Bennett (1987) found that the monthly sea level difference between Cape Parry/Sachs Harbour and Resolute is also highest in August and lowest in winter. They pointed out that there is a strong relation between the sea level difference along the Northwest Passage and volume transport through Barrow Strait. McLaughlin et al. (2004) pointed out that if the water flow through Barrow Strait is hydraulicly controlled, the volume transport through Barrow Strait

should increase during summer when the water becomes fresher, and decrease during winter when the water becomes more saline. Friction is also likely to play an important role in controlling the flow through the CAA, especially in winter when the sea ice forms a static canopy over the channel (Melling, 2000; McLaughlin et al., 2004). It is still unclear which factors have a stronger impact on the seasonal variation of volume transport through western Lancaster Sound. Now we ask two questions. What is the role of local surface stress in central Canadian Arctic on the seasonal variation of volume transport through Lancaster Sound? Does the stratification in Barrow Strait have strong impact on the seasonal variation of volume transport through Lancaster Sound?

Münchow and Melling (2008) and Rabe et al. (2010) showed results from Nares Strait, including ocean currents between 30 m and 300 m depth and temperature, conductivity, and pressure between 30 m depth and a few meters above the seabed for the 2003-2006 period. Based on three-year observations, the 3-year mean geostrophic velocity has a surface intensified southward flow of 0.20 m s^{-1} against the western side of the strait and a secondary core flowing southward at 0.14 m s^{-1} in the middle of the strait (Rabe et al., 2010). When the sea ice was drifting between late summer and early winter, there was a strong surface intensified geostrophic flow in the middle of the strait (Rabe et al., 2010). Münchow and Melling (2008) showed that the vertically averaged current speed near Ellesmere Island is southward and stronger in winter and spring when the sea ice is immobile. When the sea ice was immobile between late winter, and early summer, there was a subsurface core of strong geostrophic flow adjacent to the western side of the strait (Rabe et al., 2010). Rabe et al. (2012) found that the geostrophic volume flux through the Nares Strait was little influenced by the state of the ice. The 3-year mean geostrophic volume transport under mobile ice and fast ice was 0.47 ± 0.12 Sv, and 0.47 ± 0.09 Sv, respectively (Rabe et al., 2012). Why is the volume transport through

Nares Strait less effected by the state of sea ice?

5.2 Model configuration

We use a CAA configuration of version 3.1 of the Nucleus for European Modeling of the Ocean (NEMO) Ocean/Sea-Ice general circulation model numerical code (Madec, 2008) including the Louvain-la-Neuve sea-ice model (LIM2) (Fichefet and Maqueda, 1997) in which ice dynamics are updated with an elastic-viscous-plastic (EVP) rheology (Hunke and Dukowicz, 1997) implemented on a C-grid (Bouillon et al., 2009). The ice thermal dynamics are based on Fichefet and Maqueda (1997). The atmospheric forcing for these experiments was set up in the framework of the Coordinated Ocean-ice Reference Experiments (CORE) (Griffies et al., 2009), using the forcing fields developed by Large and Yeager (2004). The adjustment of downwelling shortwave radiation and surface air temperature for normal year forcing can be seen in Wang et al. (2012).

The CAA model domain covers the CAA, most of Baffin Bay and part of the Arctic Ocean. The tri-polar grid technique (Murray, 1996) is employed to generate the horizontal model mesh in CAA model and the model resolution is about 7.5 km. The bathymetry is obtained from IBCAO data (Jakobsson et al., 2008). The model was spun up from Septemper 1 and the initial climatological temperature and salinity data are from (Steele et al., 2001).

In the interannual year experiment, after a 5 year model run under normal year forcing, the model is run under the interannual year forcing. For the interannual year run, the CORE surface air temperatures are adjusted using IABP/POLES (International Arctic Buoy Program/Polar exchange at the Sea Surface) data, the same approach as Sou and Flato (2009). Our adjustment simply removes the monthly difference between the CORE and IABP/POLES dataset.

Since the CORE data underestimate the downwelling shortwave radiation (Wang et al., 2012), the downwelling shortwave radiation data is corrected using Arctic Global Radiation dataset by the following methods: Interannual year daily DSR = daily CORE data + monthly climatology AGR data - monthly normal year CORE data. There are two open boundaries for the interannual year run. The boundary in Foxe Basin is closed. The sea ice bridge in Nares Strait is parameterized in the CAA interannual experiment. Details of model configuration may be found in Chapter 3.

In the control experiment, there are three open boundaries. The control experiment is forced by normal year forcing for 5 years. To the east, the boundary is located in Baffin Bay. To the north, the model is connected to the Arctic Ocean and Chukchi Sea. To the south, the model is connected to Foxe Basin. The monthly temperature, salinity, and the ocean velocities at the boundary are provided from a global model with a 1° horizontal resolution (Holloway and Wang, 2009). For normal year forcing, the boundary data were averaged over years 1958-2004. The monthly sea ice boundary data (ice velocities, ice concentration and ice thickness) is derived from Pan-Arctic Ice-Ocean Modeling and Assimilation System (PIOMAS) data sets (Zhang and Rothrock, 2003). For normal year forcing, the monthly data is averaged over 1978-2004. There is no ice bridge in Nares Strait in the control experiment.

5.3 Seasonal pattern in the CAA

The background model results have been discussed previously by Wang et al. (2012) and agree well with observations. There is strong seasonal variation of sea ice motion and surface stress on the ocean in Parry Channel. In March, the modeled ice speed is less than 1 cm s^{-1} in western Parry Channel because of strong internal ice stress due to thick ice and high sea ice concentration (Figure 5.1a). The modeled ice speed in Lancaster Sound is less than 5 cm s^{-1} (Figure

5.1a). Observational results also showed that there is little net ice motion in the CAA in March except that there is eastward ice motion in Lancaster Sound (Agnew et al., 2008). Although the ice moves slowly in Parry Channel, the eastward current speed is higher than the ice speed (Figure 5.2). Since the ice stress on the ocean is determined by the difference of ice velocity and surface current velocity, the zonal ice stress on the ocean in Parry Channel is westward and about 0.02 Pa in March (Figure 5.3).

From March and May, both modeled results and observations show that there is no net ice motion in western Parry Channel because of strong internal ice stress. In June, the modeled results show that the ice moves slowly (less than 3 cm s^{-1}) in western Parry Channel although the observations show that there is no net sea ice motion in western Parry Channel in June (Agnew et al., 2008) and the ice stress on the ocean is reduced (eastward is positive) in June compared to that in March (Figure 5.3). In July, the sea ice begins to drift in western Parry Channel (Verrall et al., 1974). From July to August, model results show that the ice moves faster in western Parry Channel since the interal ice stress reduces because of reduction of ice thickness and concentration. Thus the ice stress on the ocean in Parry Channel reduces in July compared to that in June (Figure 5.3). In August, the modeled results show that the ice stress on the ocean in western Parry Channel is eastward (Figure 5.3) since the wind blows the sea ice eastward and the sea ice moves faster than ocean currents underneath.

In September, the modeled eastward ice motion is about 5 cm s^{-1} in western Parry Channel because both sea ice concentration and ice thickness decrease (Figure 5.1b). The modeled results are similar to the observed eastward ice speed (4 cm s^{-1}) in western Parry Channel in September (Agnew et al., 2008). Although the current speed in Parry Channel in September is higher than that in March (Figure 5.2), the current in Parry Channel has much less seasonal

variation than that of the sea ice motion (Figure 5.2). In September, the zonal stress on the ocean in western Parry Channel is eastward due to wind (Figure 5.3). The zonal stress on the ocean is small in eastern Parry Channel (Figure 5.3).

In October, there is mean ice motion of about 5 cm s^{-1} through western Parry Channel, which agrees well with observations (Agnew et al., 2008). Since both the ice concentration and ice thickness increase in Parry Channel, the internal ice stress increases and the mean ice stress on the ocean is westward in October (Figure 5.3). In November, the modeled results show that the sea ice moves slowly (less than 2 cm s^{-1}) in western Parry Channel. Observations show that the mean ice motion in western Parry Channel in November is near zero in most years, but in November 2006, there was a net ice motion toward Barrow Strait of about 3 cm/s in western Parry Channel (Agnew et al., 2008). The westward stress on the ocean increases from September to November since the eastward ice motion reduces due to the increase of ice thickness and ice concentration (Figure 5.3). From December to March, the modeled results show that there is nearly no sea ice motion in Parry Channel, which agrees well with observations by Agnew et al. (2008). The surface stress on the ocean reduces in Parry Channel from November to March (Figure 5.3).

In March, in most regions of Nares Strait, the ice speed is less than 3 cm s^{-1} (Figure 5.4a) although the southward current speed over the top 50 m (Figure 5.5a) is greater than 10 cm s^{-1} in western Nares Strait. The strong southward flow in western Nares Strait in March is in agreement with observations (Münchow and Melling, 2008; Rabe et al., 2010). In March, the meridional stress on the ocean is northward and about 0.02 Pa in Nares Strait since the ice is immobile and southward current is strong (Figure 5.6). The meridional stress on the ocean (northward is positive) reduces from May to July due to the reduction of internal ice stress (Figure 5.6).

In September, the ice motion is northward due to wind in northern Nares Strait (Figure 5.4). The southward current speed in western Nares Strait in September is smaller than that in March (Figure 5.5). The stress on the ocean in northern Nares Strait is northward since the ice moves northward (Figure 5.6). In September, the water flows northward on the eastern side of southern Nares Strait, which agree well with the observations of Münchow and Melling (2008). Southern Nares Strait is ice free in September and the meridional stress on the ocean in southern Nares Strait is southward in September (Figure 5.6). From October to Feburary, the meridional ice stress on the ocean in Nares Strait increases since the ice motion is retarded due to the increase of both ice thickness and concentration. Note there are only 3 to 5 grid points in Nares Strait. Therefore, we could not simulate the secondary core flowing southward in the middle of the Nares Strait.

In March, the modeled strong ice motion towards the Labrador Sea in western Baffin Bay is in agreement with the observations of Agnew et al. (2008). In March, both the ice speed and current speed are less than 3 cm s^{-1} in northeastern Baffin Bay (Figure 5.7 and Figure 5.8). Thus the zonal stress and meridional stress in northeastern Baffin Bay are small in March. In September, there is strong northwestward stress on the ocean in northeastern Baffin Bay (Figure 5.9) and the cyclonic circulation in northern Baffin Bay is stronger in September than that in March (Figure 5.8). The modeled results are similar to the observations of Tang et al. (2004) who found weaker currents in winter/spring and stronger currents in summer/fall in northeastern Baffin Bay. The stronger cyclonic circulation in northeastern Baffin Bay in summer might reduce the volume transport through Nares Strait by increasing the sea level in northeastern Baffin Bay.

The relatively high westward stress on the ocean in Parry Channel in winter might reduce the volume transport through Lancaster Sound in winter. The

relatively high northward meridional ice stress on the ocean in Nares Strait in March might have an influence on the volume transport through Nares Strait. In the following, we try to understand which factors have a strong influence in the volume transport in Parry Channel and Nares Strait.

5.4 Parry Channel

Figure 5.10 shows the time series of monthly observed and modeled volume transport through Lancaster Sound from January 1998 to November 2004. The modeled mean volume transport from January 1999 to November 2004 is 0.6 Sv and agrees well with the corresponding observed value (0.55 Sv). The variation of modeled volume transport through Lancaster Sound from January 1999 to November 2004 is similar to the observed volume transport. The correlation between the modeled volume transport from January 1999 to November 2004 and observed results is 0.71 (Figure 5.10).

Although the correlation is high, the amplitude of modeled volume transport variation through Lancaster Sound is smaller than that of observed fields. The modeled volume transport in November and December is smaller than the observations (Figure 5.10). Possible reasons for the smaller seasonal amplitude in the model simulations may include issues with the coarse resolution CORE forcing, missing localized and/or high frequency forcing, sea ice issues in the Arctic, and lack of tides in the model.

Figure 5.11 shows the mean annual cycle of observed volume transport from August 1998 to July 2010 and modeled annual cycle from August 1998 to August 2004 through Lancaster Sound. In August, the modeled volume transport is about 0.8 Sv, slightly smaller than that of observations, but the winter volume transport is higher than the observations.

In the control experiment, the monthly maximum volume transport occurs in September, while the monthly maximum volume transport in the interan-

nual run from 1998 to 2004 occurs in August. This is because in the interannual year run, Foxe Basin is closed, while an open boundary is used at Foxe Basin in the control experiment. Therefore, the boundary flows at Foxe Basin impacts the seasonal variation of volume transport through Lancaster Sound. The volume transport in the control experiment is higher than the observations. This is because the normal year forcing and the interannual year forcing are different. Although there is discrepancy between model results and observations, we still can understand the impact of surface stress and stratification on the variations of volume transport through Lancaster Sound, using five sensitivity experiments which are discussed below.

For experiments 1 to 4, the ice model is not used, river runoff is not included, and the ocean is only driven by the surface stress and boundary data. The surface stress is from daily output in the fifth year of the control experiment. The difference between each experiment can be seen in Table 5.1. The mean boundary data means the mean values of twelve months of temperature, salinity, normal velocity are set as the boundary data. That is, there is no seasonal variation at the boundary.

These five experiments are model simulations driven respectively by (a) the surface stress forcing over the whole model domain, and seasonal boundary data (experiment 1), (b) stress forcing over the whole model domain, with mean boundary data (experiment 2), (c) there is no stress at the surface and mean boundary data (experiment 3), (d) the stress is only applied in area 1 (shown in Figure 5.12), with mean boundary data (experiment 4), (e) no surface stress, mean boundary data, the ice model and river runoff are included, therefore, there are salt and heat fluxes at the surface and there is seasonal variation of river runoff (experiment 5). In the following, unless specified otherwise, the quantities will refer to those from the 3rd year of each run.

In both the control experiment and experiment 1, the volume transport

increases from April to August and decreases from September to December. The minimum volume transport is in April in both experiments. Since the seasonal variation of volume transport in experiment 1 is similar to that in control experiment, the surface stress and seasonality of boundary flows are the major reasons in controlling the seasonal variation of the volume transport (Figure 5.13). The volume transport in experiment 1 is lower than that in the control experiment and the mean difference of volume transport between the two experiments is 0.17 Sv in the third year of model run. This shows that the steric height has an impact on the mean volume transport because the difference between experiment 1 and control experiment is that there is boundary fluxes at the surface and river runoff in the control experiment while experiment 1 does not consider those factors.

The volume transport in experiment 2 has a strong seasonal cycle and increases from June to September and decreases from November to February. The volume transport changes only 0.04 Sv from September to November in experiment 2 while the volume transport in experiment 1 decreases by 0.21 Sv over the same period. Therefore, the boundary flows have strong impact on the volume transport. Kliem and Greenberg (2003) used a diagnostic model to study summer mean circulation in the CAA. Their model results reveal that the currents in the CAA depend on the elevation difference between the Arctic Ocean and Baffin Bay. The variation of boundary flows can cause the variation of the sea level in Arctic Ocean and Baffin Bay, and thus changing the volume transport through Lancaster Sound. McGeehan and Maslowski (2012) have pointed out that the reduced northward flow of the West Greenland Current in winter can increase the volume transport through Lancaster Sound in winter compared to that in fall since reduced northward flow of the West Greenland Current can reduce the sea level in Baffin Bay. Another possible reason that the volume transport in the control experiment is not same as observation

because the boundary value might not be very good.

Experiment 3 shows that if there is no surface stress over the model domain with mean boundary flows, there are no seasonal variations of volume transport. The mean volume transports in the third year of model in experiment 2, 3 are 0.65 Sv, 0.68 Sv, respectivley. There is only a little change of volume transport after the surface stress over the whole model domain is removed. When there is no surface stress, the mean volume transport through Lancaster Sound is nearly same as that in experiment 1. Comparing to experiment 3, the surface stress over the model domain causes the strong seasonal cycle of volume transport through Lancaster Sound in experiment 1.

In experiment 4, the volume transport increases from June to September and decreases from September to February when only surface stress exists in central Canadian Arctic. The volume transport increases from June to September because the zonal surface stress on the ocean increases from June to August (eastward is positive). The volume transport decreasees from September to November because the zonal surface stress on the ocean decreases from September to November. The amplitude of volume transport variation is 0.18 Sv, while the amplitude of volume transport variation in the control experiment is 0.29 Sv. Therefore, the seasonal variation of local surface stress in the central Canadian Arctic is one of major reasons that cause the seasonal variation of volume transport. The annual mean volume transport through Lancaster Sound declines over the model run. Therefore, the stress in the central Canadian Arctic has an impact on the annual mean volume transport through Lancaster Sound. In experiment 2, the volume transport decreases 0.04 Sv from September to November, while the volume transport decreases 0.08 Sv during the same period in experiment 4. The volume transport increases 0.01 Sv from April to June in experiment 2, while the volume transport increases 0.04 Sv during the same period in experiment 4. Therefore, not only

the local stress, but also the remote stress can change the volume transport through Lancaster Sound.

Experiment 5 shows that there is no strong seasonal variation of volume transport when sea ice model and river runoff are included and there is no surface stress. In Barrow Strait, the stratification is strong in summer and weak in winter because sea ice melts in summer and sea ice forms in winter becasue the sea ice model is used in this experiment. Thus the volume transport through Lancaster Sound is not hydraulically controlled and the stratification in Barrow Strait does not have strong impact on the volume transport through Lancaster Sound. Comparing experiments 3 and 5, the volume transport is large in experiments 5 and the difference of volume transport between experiments 3 and 5 in the third year of model run is 0.08 Sv, suggesting steric height has a strong influence on the mean volume transport through Lancaster Sound. In the future, we will do more experiments to see which factor (salt flux, heat flux or river runoff) is most important.

5.5 Nares Strait

In the control experiment, the volume transport through Nares Strait decreases from June (0.71 Sv) to August (0.47 Sv) and the volume transport increases from September (0.38 Sv) to January (0.70 Sv) although the observed results show that the volume transport through Nares Strait does not have a strong seasonal cycle. Although the model results does not agree well with current observed results (which are however based on a very short period), we still can understand why the volume transport is high in winter, although the ice stress on the ocean in Nares Strait tends to decrease volume transport in winter.

In order to study the effect of surface stress on the volume transport in Nares Strait, two additional sensitivity experiments are conducted besides the previous discussed experiments: (e) the stress exists only in area 2 (shown in

Figure 5.12), with mean boundary data (experiment 6), (f) the stress exists only in area 3 (shown in Figure 5.12), with mean boundary data (experiment 7). The ocean is only driven by the surface stress and boundary data. The stress is from the daily output of the fifth year of the control experiment.

Although the suface heat and salt fluxes and river runoff are not considered in experiment 1, the seasonal variation of volume transport through Nares Strait in experiment 1 is similar to that in the control experiment (Figure 5.14). This shows that surface stress and boundary flows are major factors that control the volume transport through Nares Strait. However, the volume transport in experiment 1 is greater than that in the control experiment and thus the steric height can influence the mean volume transport through Nares Strait. The mean difference between the control experiment and experiment 1 over the third year of model run is 0.14 Sv.

In experiment 2, the volume transport through Nares Strait is low in winter and high in summer, similar to that in experiment 1. However, the seasonal variation of volume transport through Nares Strait in experiment 2 is 0.16 Sv while the seasonal variation of volume transport is 0.36 Sv in experiment 1. Since the boundary flows in experiment 1 have seasonal variation while the boundary flows in experiment 2 has no seasonal variation, the boundary flows have strong impact on the volume transport in Nares Strait. McGeehan and Maslowski (2012) have pointed out that the reduced northward flow of the West Greenland Current in winter can increase the volume transport through Nares Strait in winter compared to that in summer since reduced northward flow of the West Greenland Current can reduce the sea level in Baffin Bay.

Experiment 3 shows that if there is no surface stress over the model domain with mean boundary flows, there are no seasonal variations of volume transport through Nares Strait. The mean volume transport through Nares Strait in experiments 1 and 3 are 0.77 Sv and 0.78 Sv, respectively. Comparing

experiment 1 to experiment 3, the stress over the whole model domain in experiment 1 only changes the seasonal variability of volume transport through Nares Strait, but does not change the mean volume transport through Nares Strait.

In experiment 4, the volume transport through Nares Strait is lowest in September and highest in April and the difference is 0.14 Sv. In this experiment, the volume transport through Lancaster Sound is highest in September and lowest in April. Therefore, the volume transport through Nares Strait is relatively small in summer because of enhanced transport through Lancaster Sound in summer. In general, the annual mean volume transport through Nares Strait increases over the model run because the volume transport through Lancaster Sound declines over the model run (Figure 5.13). Therefore, the surface stess in central Canadian Arctic has a strong impact on the volume transport through Nares Strait.

The meridional stress on the ocean (northward is positive) increases in winter since the internal ice stress increases due to the increase of both ice thickness and concentration increase (Figure 5.6). In experiment 6, the stress only exists in Nares Strait, the volume transport decreases from September to April and the variation of volume transport is 0.08 Sv. Therefore, the surface stress on the ocean in Nares Strait reduces the volume transport through Nares Strait in winter. The local surface stress in Nares Strait does not have strong impact as that in experiment 3 since the variation of volume transport (0.14 Sv) in experiment 3 is higher than that in experiment 6 (0.08 Sv). We think that because the length of Nares Strait is shorter than that of Parry Channel, the local surface stress in Nares Strait does not have as strong impact as in Parry Channel.

In summer, the cyclonic surface stress in northern Baffin Bay increases, and the cyclonic circulation in northern Baffin Bay increases (Figure 5.9). In

experiment 7, the volume transport in summer is lower than that in winter and the variation is 0.08 Sv. Therefore, the stress on the ocean in Baffin Bay reduces the volume transport in summer but the impact is not strong.

5.6 Conclusions

A regional Canadian Arctic Archipelago model is set up to study the seasonal variation of volume transport through the Parry Channel and Nares Strait. In winter, the sea ice could not move through western Parry Channel and moves slowly in eastern Parry Channel. Since the current moves underneath, the ice stress on the ocean is westward. In summer, the sea ice is mobile and the ice stress on the ocean is small. The model sensitivity experiments show that the ice stress on the ocean in Parry Channel has a strong impact on the seasonal variation of volume transport through western Lancaster Sound. The volume transport increases from June to September because the zonal surface stress on the ocean increases from June to August (eastward is positive). The volume transport decreases from September to November because the zonal surface stress on the ocean decreases over the same period. In winter, the ice stress on the ocean reduces the volume transport through western Lancaster Sound. The boundary flows also have strong impact on the volume transport through western Lanaster Sound and Nares Strait. The stratification does not have strong impact on the seasonal variation of volume transport through Lancaster Sound and the volume transport through Lancaster Sound is not hydaulic controlled.

We also tried to understand why the volume transport through Nares Strait is less affected by the state of sea ice. We found that the ice stress on the ocean in Parry Channel, stress on the ocean in Nares Strait, stress on the ocean in Baffin Bay have impact on the seasonal variation of volume transport through Nares Strait. The impact of local stress on the ocean in Nares Strait is not as

strong as that in Parry Channel. The boundary flows have strong impact on the volume transport through Nares Strait.

Table 5.1: List of sensitivity experiments.

Experiment	stress region	BC	ice model
1	whole model domain	seasonal	no
2	whole model domain	mean	no
3	no stress	mean	no
4	only in area 1	mean	no
5	no stress	mean	yes
6	only in area 2	mean	no
7	only in area 3	mean	no

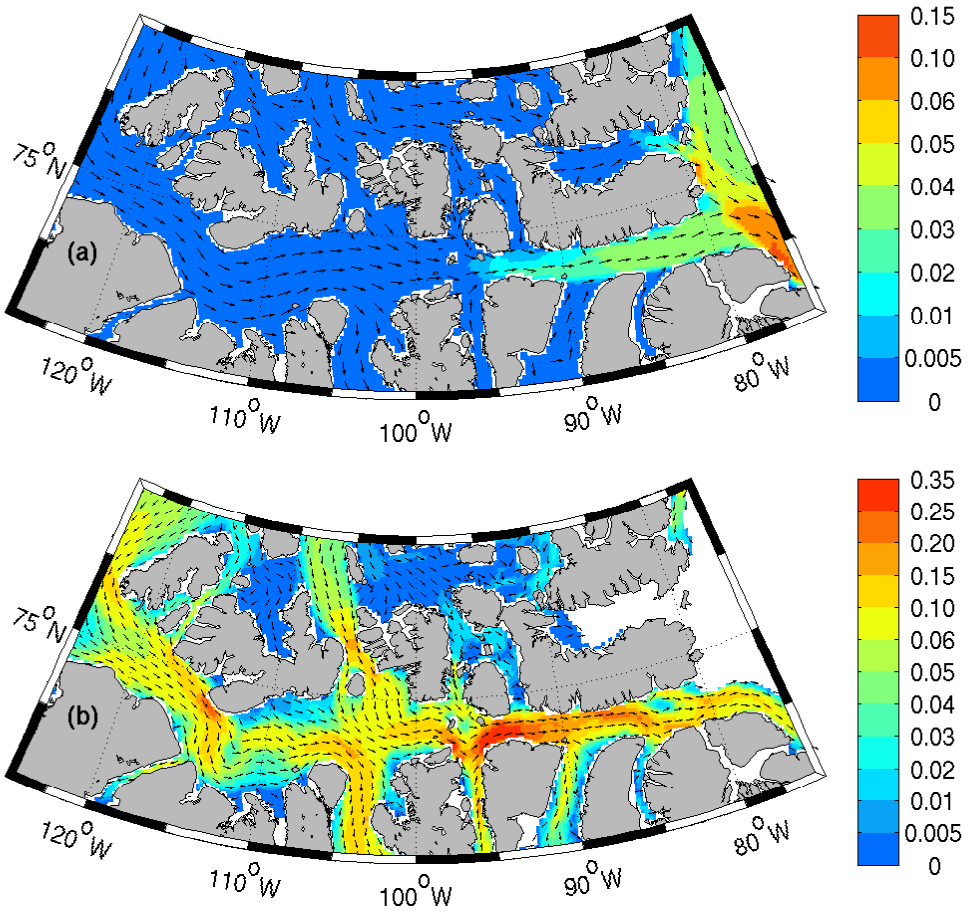

Figure 5.1: Magnitude (cm s^{-1}) of monthly sea ice motion (color contoured) in March (a) and September (b) with velocity vectors superimposed in Parry Channel in the fifth year of model run under normal year forcing, with one third of the horizontal grid points shown.

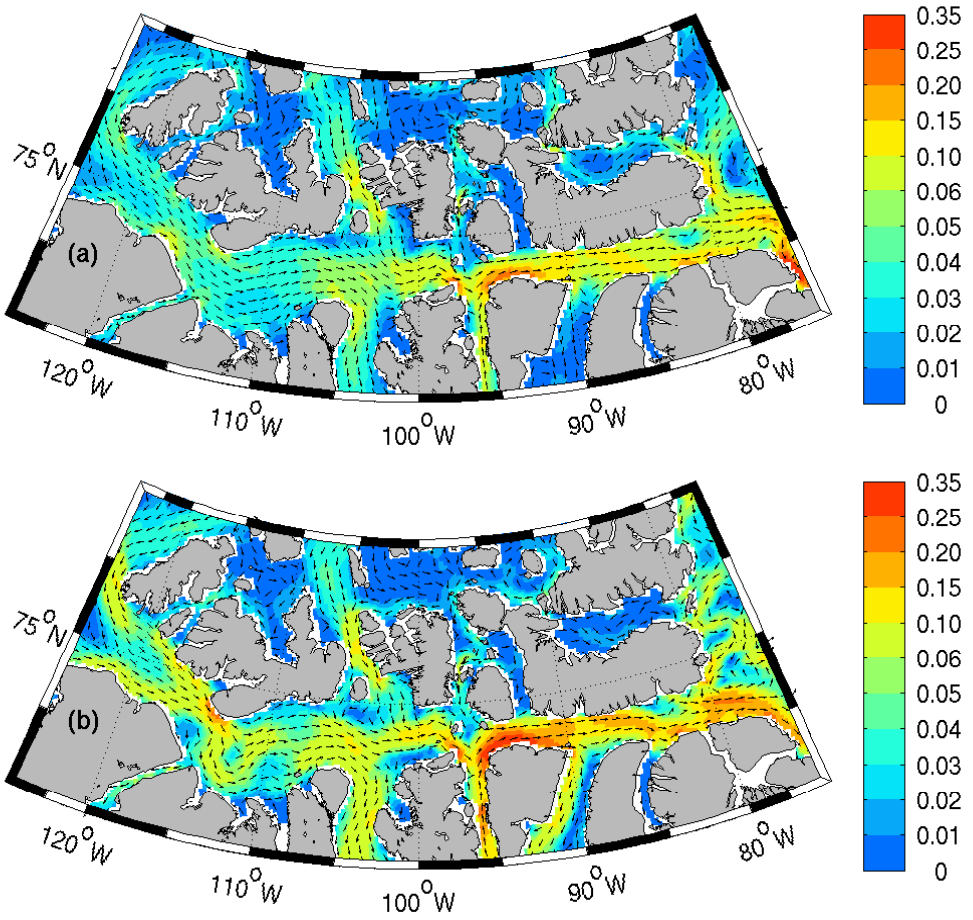

Figure 5.2: Magnitude (cm s^{-1}) of monthly currents over top 50 m (color contoured) in (a) March (b) and September with velocity vectors superimposed in Parry Channel in the fifth year of the model run under normal year forcing, with one third of the horizontal grid points shown.

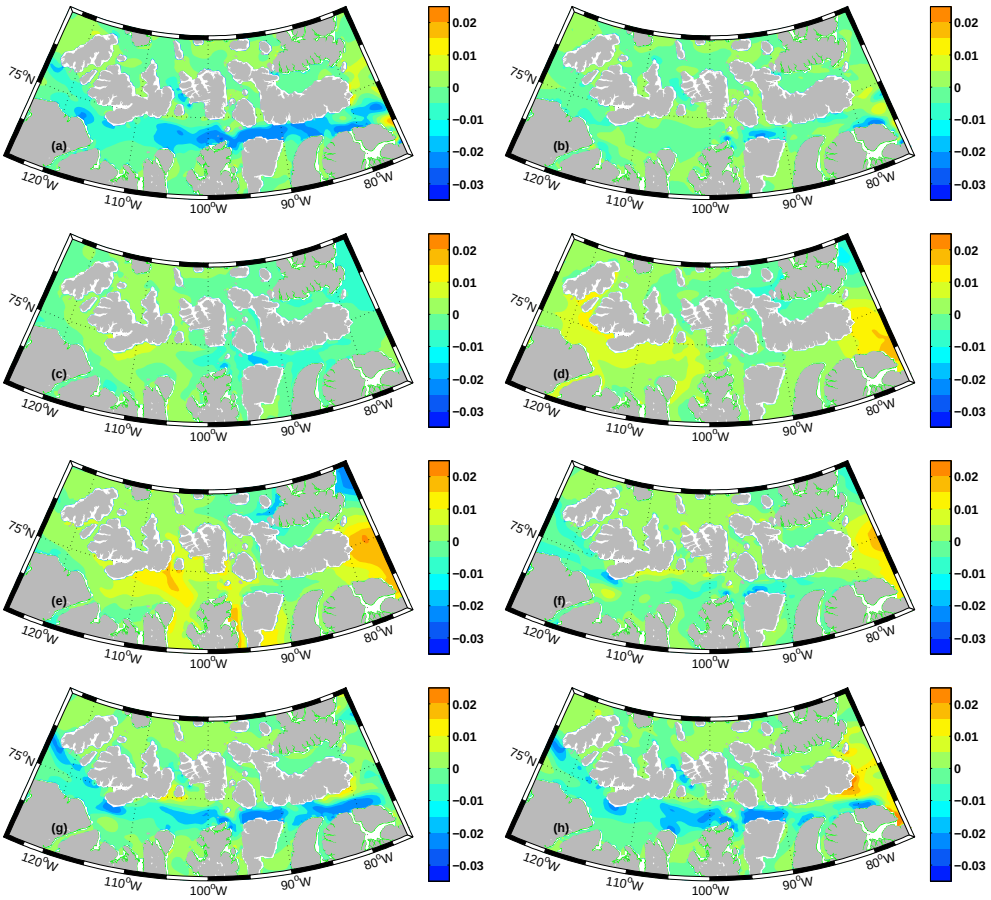

Figure 5.3: The zonal stress [Pa] on the ocean in Parry Channel in (a) March, and (b) June, (c) July, (d) August, (e) September, (f) October, (g) November, (h) December in the fifth year of the model run under normal year forcing. Eastward is positive.

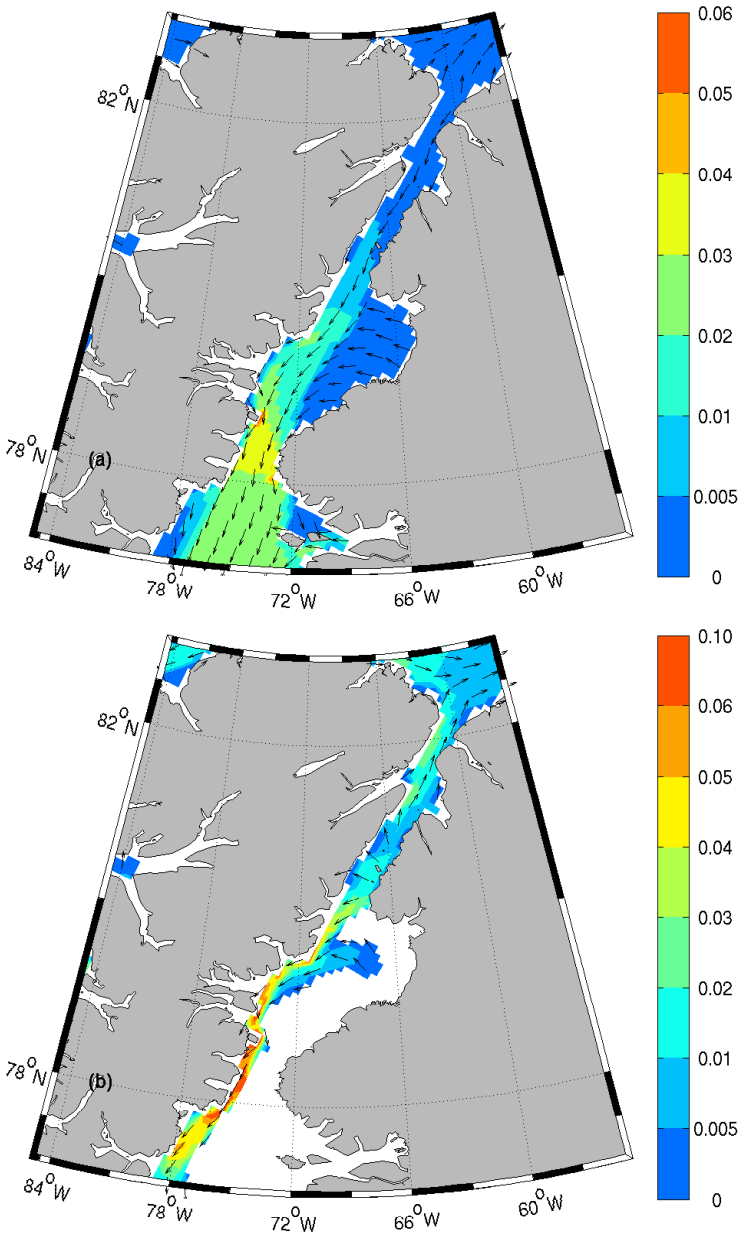

Figure 5.4: Magnitude (cm s^{-1}) of monthly sea ice motion (color contoured) in March (a) and September (b) with velocity vectors superimposed in Nares Strait in the fifth year of the model run under normal year forcing, with one third of the horizontal grid points shown.

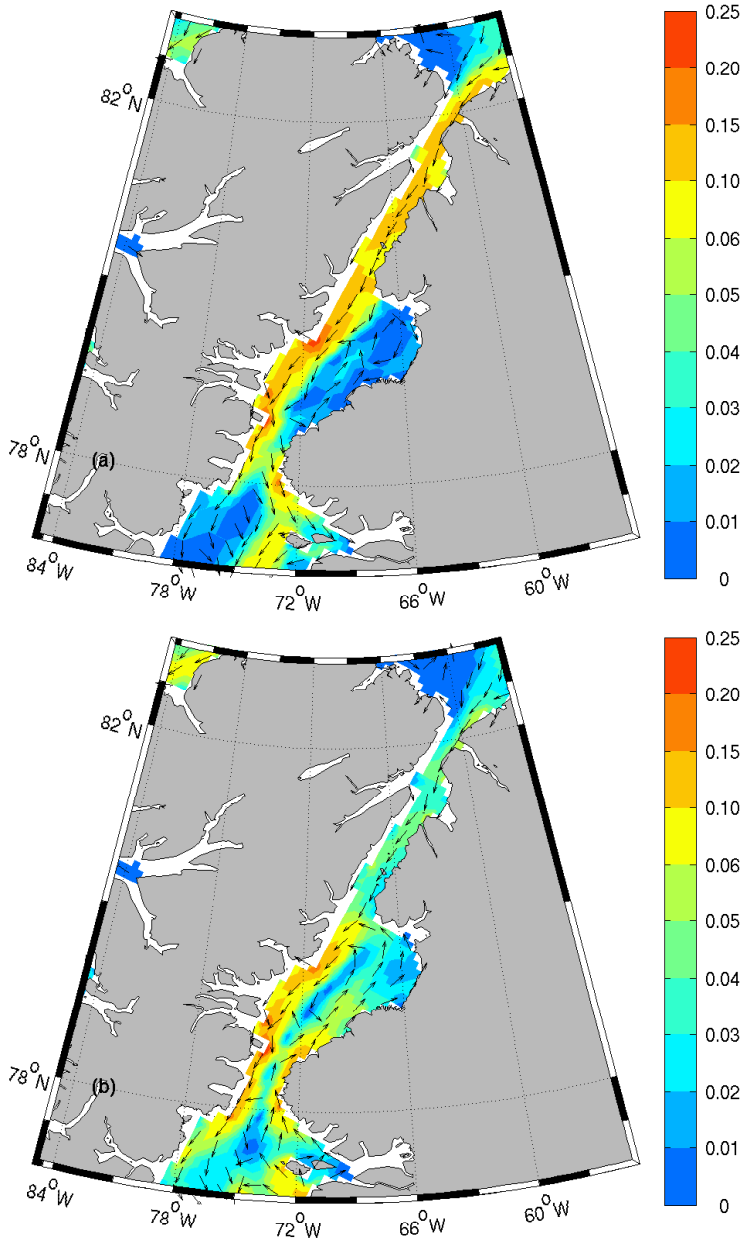

Figure 5.5: Magnitude (cm s^{-1}) of monthly currents over top 50 m (color contoured) in March (a) and September (b) with velocity vectors superimposed in Nares Strait in the fifth year of model run under normal year forcing, with one third of the horizontal grid points shown.

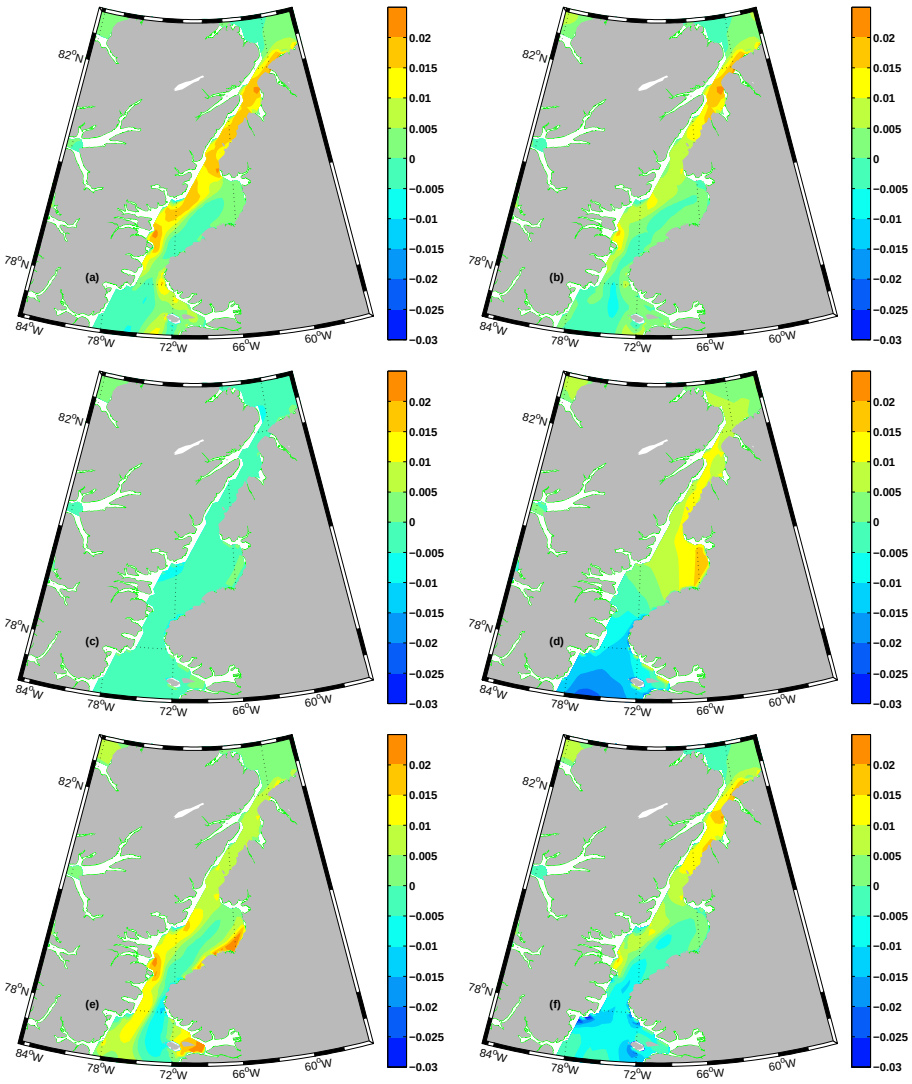

Figure 5.6: The meridional stress on the ocean in Nares Strait in (a) March, (b) May, (c) July, (d) September, (e) November, (f) January in the fifth year of model run under normal year forcing. Northward is positive.

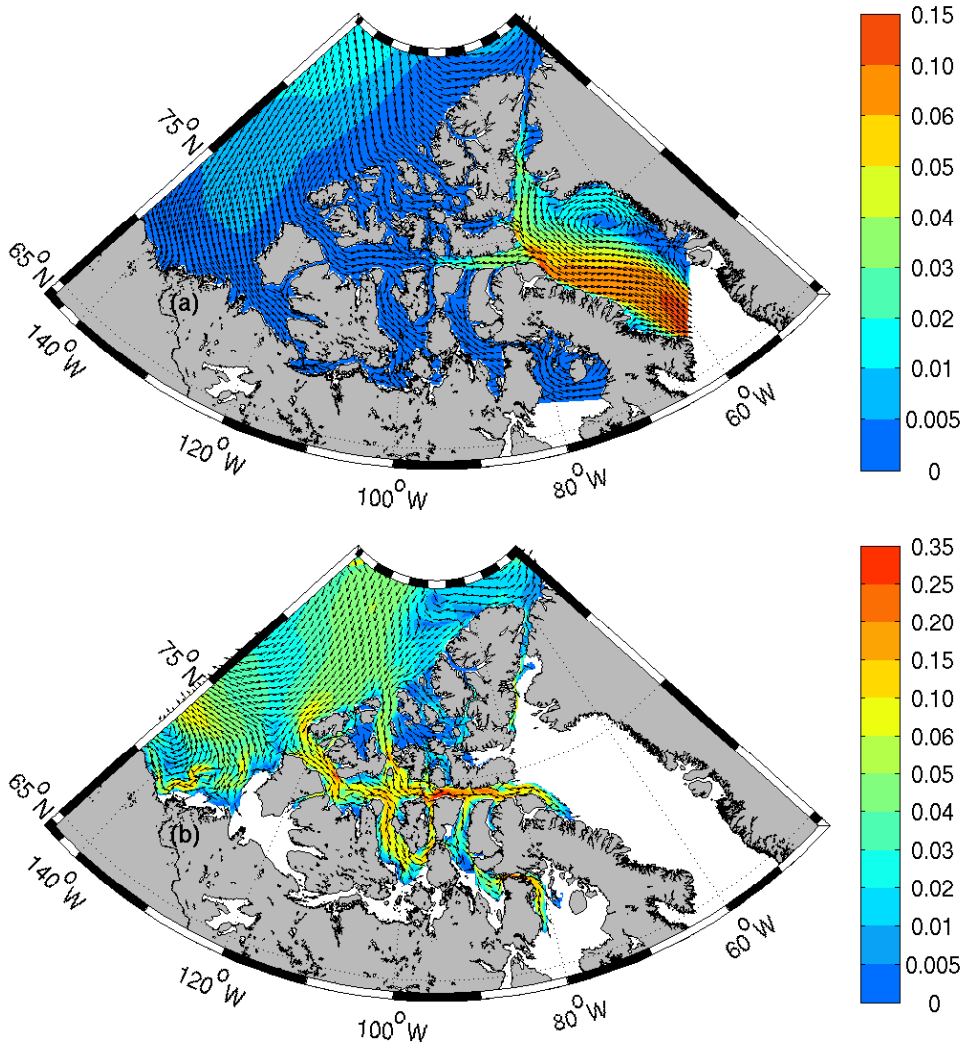

Figure 5.7: Magnitude (cm s^{-1}) of monthly sea ice motion (color contoured) in March (a) and September (b) with velocity vectors superimposed in the fifth of model year run under normal year forcing, with one fifth of the horizontal grid points shown.

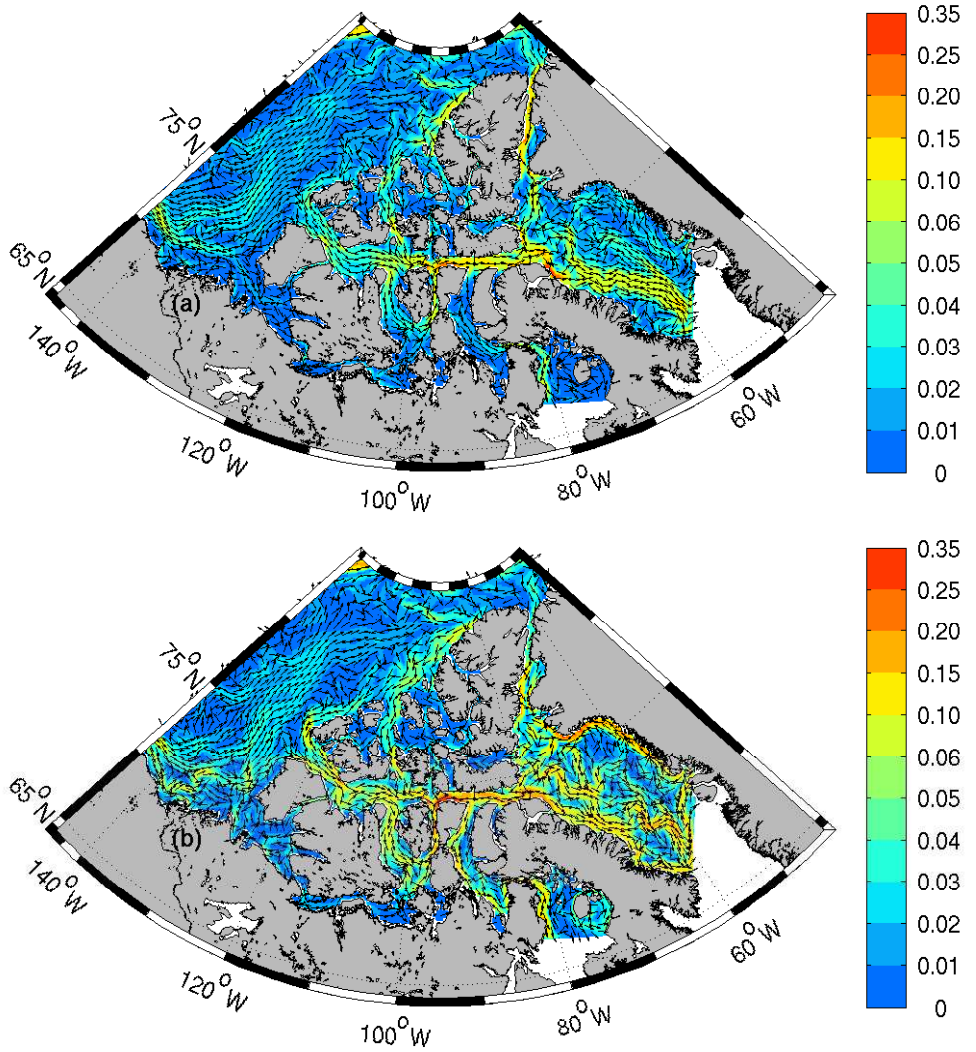

Figure 5.8: Magnitude (cm s^{-1}) of monthly currents over top 50 m (color contoured) in March (a) and September (b) with velocity vectors superimposed in the fifth year of model run under normal year forcing, with one fifth of the horizontal grid points shown.

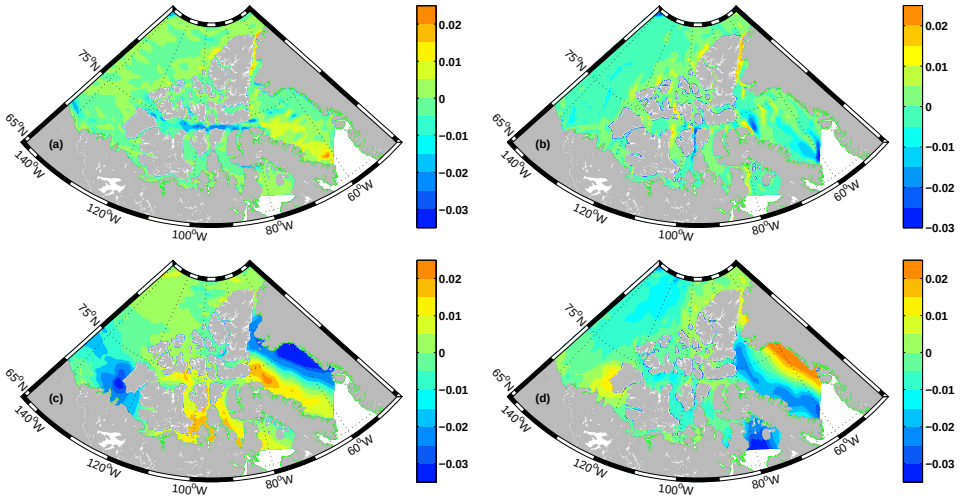

Figure 5.9: Model results of monthly mean zonal stress [Pa] (a) and meridional stress (b) in March, zonal stress (c) and meridional stress (d) in September in the fifth year of model run under normal year forcing.

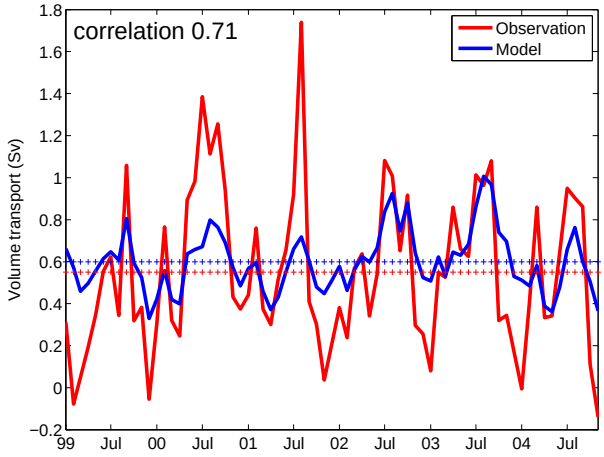

Figure 5.10: Time series of monthly observed (red line) and modeled (blue line) volume transport [Sv] through Lancaster Sound from January 1998 to November 2004.

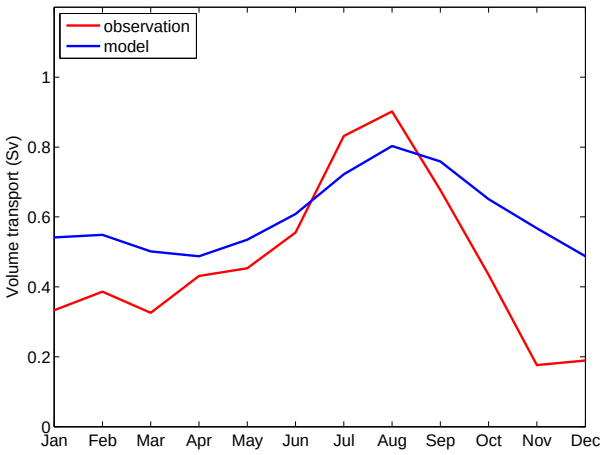

Figure 5.11: Mean annual cycle of observed volume transport [Sv] from August 1998 to July 2010 (blue line) and modeled volume transport from August 1998 to August 2004 (red line) through western Lancaster Sound.

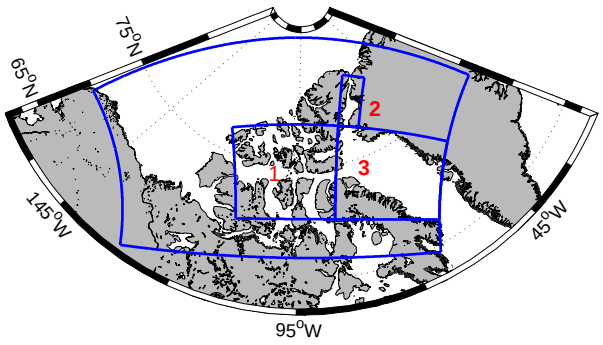

Figure 5.12: Position of areas 1, 2, and 3.

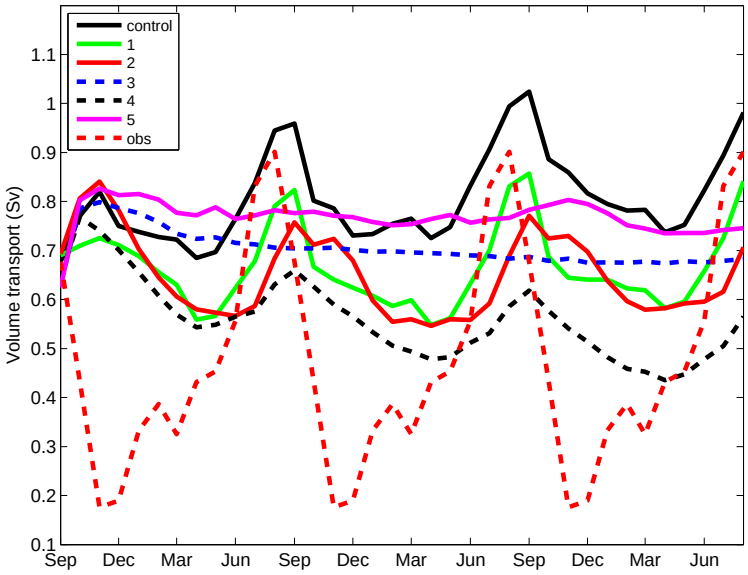

Figure 5.13: Time series of volume transport [Sv] through western Lancaster Sound in different sensitivity experiments.

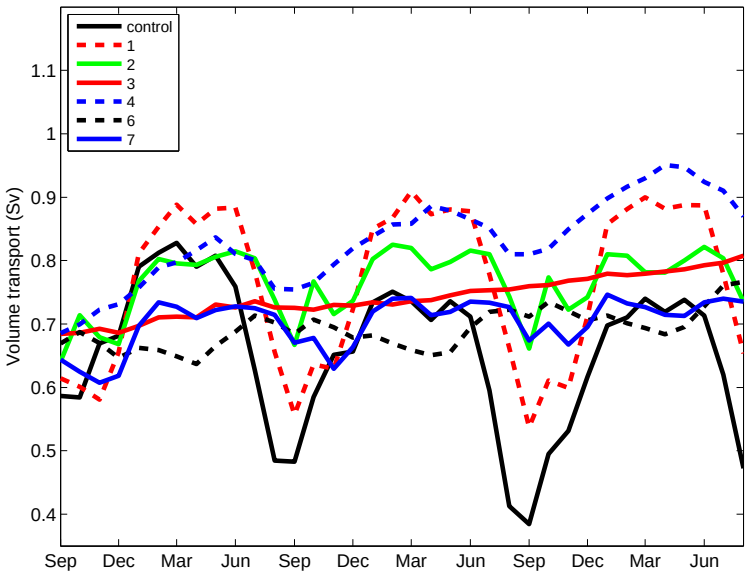

Figure 5.14: Time series of volume transport [Sv] through Nares Strait in different sensitivity experiments.

Bibliography

Aagaard, K., and E. Carmack, 1989: The role of sea ice and other fresh water in the Arctic circulation. *Journal of Geophysical Research*, **94**, 14485–14498.

— 1994: The Arctic Ocean and climate: A perspective. *The Polar Oceans and Their Role in Shaping the Global Environment: The Nansen Centennial Volume*, O. M. Johannessen, R. D. Muench, and J. E. Overland, eds., Amer. Geophys. Union, USA, volume 85 of *Geophysical Monograph*, 4–20.

Agnew, T., A. Lambe, and D. Long, 2008: Estimating sea ice area flux across the Canadian Arctic Archipelago using enhanced AMSR-E. *Journal of Geophysical Research*, **113**, doi:10.1029/2007JC004582.

Bouillon, S., M. A. M. Maqueda, V. Legat, and T. Fichefet, 2009: An elasticviscousplastic sea ice model formulated on Arakawa B and C grids. *Ocean Modelling*, **27**, doi:10.1016/j.ocemod.2009.01.004, 174–184.

Carmack, E., 2007: The alpha/beta ocean distinction: A perspective on freshwater fluxes, convection, nutrients and productivity in high-latitude seas. *Deep Sea Research Part II*, **54**, doi:10.1016/j.dsr2.2007.08.018, 2578–2598.

Dickson, R., B. Rudels, S. Dye, M. Karcher, J. Meincke, and I. Yashayaev, 2007: Current estimates of freshwater flux through Arctic and subarctic seas. *Progress in Oceanography*, **73**, doi:10.1016/j.pocean.2006.12.003, 210–230.

Fichefet, T., and M. M. Maqueda, 1997: Sensitivity of a global sea ice model to

the treatment of ice thermodynamics and dynamics. *Journal of Geophysical Research*, **102**, 12609–12646.

Griffies, S., A. Biastoch, C. Bning, F. Bryan, G. Danabasoglu, E. Chassignet, M. England, R. Gerdes, H.Haak, R. Hallberg, W. Hazeleger, J. Jungclaus, W. Large, A. P. G. Madec, B. Samuels, M. Scheinert, A. S. Gupta, C. Severijns, H. Simmons, A. Treguier, M. Winton, S. Yeager, and J. Yin, 2009: Coordinated Ocean-ice Reference Experiments (COREs). *Ocean Modelling*, **26**, doi:10.1016/j.ocemod.2008.08.007, 1–46.

Holloway, G., and Z. Wang, 2009: Representing eddy stress in an Arctic Ocean model. *Journal of Geophysical Research*, **114**, doi:10.1029/2008JC005169.

Hunke, E., and J. Dukowicz, 1997: An Elastic-Viscous-Plastic for sea ice dynamics. *Journal of Physical Oceanography*, **27**, 1849–1867.

Jakobsson, M., R. Macnab, L. Mayer, R. Anderson, M. Edwards, J. Hatzky, H. W. Schenke, and P. Johnson, 2008: An improved bathymetric portrayal of the Arctic Ocean: Implications for ocean modeling and geological, geophysical and oceanographic analyses. *Geophys. Res. Lett.*, **35**, doi:10.1029/2008GL033520.

Kliem, N., and D. A. Greenberg, 2003: Diagnostic simulations of the summer circulation in the Canadian Arctic Archipelago. *Atmosphere-Ocean*, **41**, 273–289.

Large, W., and S. Yeager, 2004: Diurnal to decadal global forcing for ocean and sea-ice models: the data sets and flux climatologies. NCAR, NCAR technical note: NCAR/TN-460+ STR.

Madec, G., 2008: NEMO Ocean Engine. Institut Pierre-Simon Palace (IPSL), France, volume 27 of *Notes de Pole de modelisation*.

McGeehan, T., and W. Maslowski, 2012: Evaluation and control mechanisms of volume and freshwater export through the Canadian Arctic Archipelago in a high-resolution pan-Arctic ice-ocean model. *Journal of Geophysical Research*, **117**, doi:10.1029/2011JC007261.

McLaughlin, F., E. Carmack, R. Ingram, W. Williams, and C. Michel, 2004: Oceanography of the northwest passage. *The Sea*, A. Robinson and K. Brink, eds., Harvard University Press, New York, Vol 14, part B, 1211–1242.

Melling, H., 2000: Exchanges of freshwater through the shallow straits of the North American Arctic. *Freshwater Budget of the Arctic Ocean*, E. L. et al., ed., Kluwer Academic Publishers, The Netherlands, NATO Science Series, 479–502.

Melling, H., T. Agnew, K. K. Falkner, D. Greenberg, C. Lee, A. Mnchow, B. Petrie, S. Prisenberg, R. Samelson, and R. A. Woodgate, 2008: Freshwater fluxes via Pacific and Arctic outflows across the Canadian Polar Shelf. *Arctic-Subarctic Ocean fluxes, defining the role of the northern seas in climate*, R. R. Dickson, J. Meincke, and P. Rhines, eds., Springer, New York, 193–247.

Münchow, A., and H. Melling, 2008: Ocean current observations from Nares Strait to the west of Greenland: Interannual to tidal variability and forcing. *Journal of Geophysical Research*, **66**, 801–833.

Murray, R. J., 1996: Explicit generation of orthogonal grids for ocean models. *Journal of Computational Physics*, **126**, doi:10.1006/jcph.1996.0136, 251–273.

Prinsenberg, S. J., and E. Bennett, 1987: Mixing and transports in Barrow Strait, the central part of the Northwest passage. *Continental Shelf Research*, **7**, doi:10.1016/0278-4343(87)90006-9, 913–935.

Rabe, B., H. L. Johnson, A. Münchow, and H. Melling, 2012: Geostrophic ocean currents and freshwater fluxes across the Canadian polar shelf via Nares Strait. *Journal of Marine Research*, submitted.

Rabe, B., A. Münchow, H. L. Johnson, and H. Melling, 2010: Nares Strait hydrography and salinity field from a 3-year moored array. *Journal of Geophysical Research*, **115**, doi:10.1029/2009JC005966.

Sou, T., and G. Flato, 2009: Sea ice in the Canadian Arctic Archipelago: Modeling the past (1950–2004) and the future (2041–60). *Journal of Climate*, **22**, doi:10.1175/2008JCLI2335.1, 2181–2198.

Steele, M., R. Morley, and W. Ermold, 2001: PHC: A global ocean hydrography with a high-quality Arctic Ocean. *Journal of Climate*, **14**, 2079–2087.

Tang, C. C., C. K. Ross, T. Yao, B. Petrie, B. M. DeTracey, and E. Dunlap, 2004: The circulation, water masses and sea-ice of Baffin Bay. *Progress in Oceanography*, **63**, doi:10.1016/j.pocean.2004.09.005, 183–228.

Verrall, R., J. Ganton, and A. Milne, 1974: An ice drift measurement in western Parry Channel. *Arctic*, **27**, 47–52.

Wang, Q., P. G. Myers, X. Hu, and A. B. Bush, 2012: Flow constrains on pathways through the Canadian Arctic Archipelago. *Atmosphere-Ocean*.

Zhang, J., and D. A. Rothrock, 2003: Modeling global sea ice with a thickness and enthalpy distribution model in generalized curvilinear coordinates. *Mon. Wea. Rev.*, **131**, 845–861.

Chapter 6

Summary

A coupled ocean/sea-ice CAA configuration has been developed to simulate the circulation in the CAA. The surface air temperature in Nares Strait from CORE data is underestimated in August and September. We use IABP/POLES data to correct the CORE data. The downwelling shortwave radiation from CORE is underestimated in Nares Strait. We use the Arctic Global Radiation dataset to correct the CORE data. After adjusting the surface air temperature and the downwelling shortwave radiation, both simulated sea ice concentration and ice thickness are consistent with observed results. We did some sensitivity experiments to show that the ice bridge in Nares Strait does not have a strong impact on the sea ice concentration in northern Baffin Bay but help to simulate the sea ice better in Nares Strait. The use of AGR downwelling shortwave radiation data improves the model performance on simulating the sea ice concentration. The current speed and direction at Byam Martin Channel, Penny Strait are in good agreement with observations. The vertical structure and transports in Barrow Strait agree with observed results. The volume transport through Peel Sound also agree well with observations. Furthermore, the southward flow in M'Clintock Channel and northward flow in Peel Sound is reproduced.

The flow dynamics in the CAA are diagnosed by using a numerical model.

The classic view is that the flow through Parry Channel is controlled by the sea surface gradient between the Arctic Ocean and Baffin Bay (Stigerbrandt, 1984). However, model results shows that the flow is more complex than previously thought. This is the first time that we show that the flows through Peel Sound has mainly come from M'Clintock Channel. We also point out why the water flows southward in M'Clintock Channel. Our analysis shows that the flow in M'Clintock Channel is produced by a southward ageostrophic acceleration. The ageostrophic acceleration is mainly balanced by the vertical diffusion term and the nonlinear advection term. The southward flow is also strongly influenced by sills at south of Prince of Wales Island and another one located at Barrow Strait.

In the eastern Lancaster Sound, the Baffin Current penetrates westward along the north side of eastern Lancaster Sound, crosses to the south side and then flows out to the east. Vorticity dynamics explains why the Baffin Current cannot not intrude further than into Resolute. The analysis reveals that the stratification in combination with the topography prevents westward flow further into Barrow Strait and there is downwelling as the flow recirculates towards the south in eastern Lancaster Sound.

There is a national marine conservation area in Lancaster Sound. Lancaster Sound is an area of critical ecological importance to marine mammals, including seals, narwhal, beluga and bowhead whales, as well as walrus and polar bears. Our understanding of the circulation pattern in Lancaster Sound can help us to understand the nutrients distribution in Lancaster Sound.

Although Peel Sound is part of the summer home range of harp seal, bowhead whale, beluga whale, and narwhal, they are not found in MClintock Channel (Stephenson and Hartwig, 2010; Dietz et al., 2008). The persistent sea ice in M'Clintock Channel limits the movements of narwhal, bowhead whale, beluga whale, and various species of seal (Harington, 1966; Dyke et al., 1996).

Therefore, we found that the southward currents and sea ice in M'Clintock Channel have an impact on the marine mammals since southward sea ice motion is related to southward ocean currents.

In summer the volume transport is higher than that in winter in western Lancaster Sound and Barrow Strait. We have expalined the role of surface stress and stratification on the seasonal variation of volume transport through Parry Channel. In winter, the sea ice could not move in western Parry Channel and moves slowly in eastern Parry Channel. Since the current moves underneath, the ice stress on the ocean is westward. In summer, the sea ice is mobile and the ice stress on the ocean is small. Sensitivity experiments and the model results show that the surface stress on the ocean in Parry Channel has a strong impact on the seasonal variation of volume transport through western Lancaster Sound. In winter, the ice stress on the ocean reduces the volume transport in western Lancaster Sound. The boundary flows also have strong impact on the volume transport through western Lancaster Sound and Nares Striat. We also found that the volume transport through Lancaster Sound is not hydraulically controlled and the stratification in Barrow Strait does not have a strong impact on the volume transport through Lancaster Sound.

Sensitivity experiments found that the ice stress on the ocean in Parry Channel, and stress on the ocean in Nares Strait impact the seasonal variation of volume transport through Nares Strait. The impact of local stress on the ocean in Nares Strait is not as strong as that in Parry Channel. The boundary flows have a strong impact on the seasonal variation of volume transport through Nares Strait. This is the first time that we show that the seasonal variability of the sea ice motion in the central CAA has strong impact of the circulation in the CAA.

The variability of primary production may be the result of changes in

water masses in the surface layer. To better understand the variability of the circulation in the CAA can help us to better understand the variability of primary production. Our results of the circulation pathways through the CAA can help us to understand the transport of nutrients and the cycling of mercury in the CAA.

In the future, we will do more experiments to see which factor (salt flux, heat flux or river runoff) is most important on the volume transport through Lancaster Sound. We also will do more sensitivity experiments to understand how the changes at the boundary impact on the seasonal variation of volume transport through Lancaster Sound. Tides will be considered in the configuration in the future work.

Bibliography

Dietz, R., M. P. Heide-Jrgensen, P. Richard, K. L. Jack Orr, and H. C. Schmidt, 2008: Movements of narwhals (Monodon monoceros) from Admiralty Inlet monitored by satellite telemetry. *Polar Biology*, **31**, doi:10.1007/s00300-008-0466-4, 1295–1306.

Dyke, A. S., J. Hooper, and J. M. Savelle, 1996: A history of sea ice in the Canadian Arctic Archipelago based on postglacial remains of the bowhead whale (Balaena mysticetus). *Arctic*, **49**, 235–255.

Harington, C. R., 1966: Extralimital occurrences of walruses in the Canadian Arctic. *Journal of Mammalogy*, **47**, 506–513.

Stephenson, S., and L. Hartwig, 2010: The Arctic Marine Workshop. *Proceedings of the Arctic Basin Symposium*, Freshwater Institute, Winnipeg, Manitoba, Can. Manuscript Rep. Fish. Aquat. Sci. 2934.

Stigerbrandt, A., 1984: The North Pacific: a global-scale estuary. *Journal of Physical Oceanography*, **14**, 464–470.